New μ-CHP network technologies
for energy efficient and sustainable districts
Project co-funded by EC. Grant no 260105.

D3.3

Report on results from case studies for biogas fuel utilization at the FC-District unit

Issue Date	28-02-2013 (M30)
Deliverable Number	D3.3
WP Number	WP3: Building and district tailoring of SOFC
Status	Approved
Author(s)	J. Navalho, J. M. C. Pereira, J. C.F. Pereira (IST) G. Vourliotakis, Ch. Keramiotis, G. Skevis, M. Founti (NTUA.HMCS) Ciprian Chisega-Negrilã (OVM-ICCPET)

Dissemination level		
PU	Public	**X**
PP	Restricted to other programme participants (including the Commission Services)	
RE	Restricted to a group specified by the consortium (including the Commission Services)	
CO	Confidential, only for members of the consortium (including the Commission Services)	

Document history

Version	Date	Author	Description
0.1	2013-01-06	Jorge Navalho (IST)	Draft version
0.2	2013-01-08	Ciprian Chisega-Negrilã (OVM-ICCPET)	Integration of OVM-ICCPET contribution
0.3	2013-01-20	George Vourliotakis (NTUA.HMCS)	Integration of NTUA.HMCS contribution
1.0	2013-02-12	Jorge Navalho (IST)	First version
2.0	2013-02-18	Maria Founti (NTUA.HMCS)	Peer review
3.0	2013-02-21	Jorge Navalho (IST)	Final version

Table of contents

Summary

This document presents a review on conventional non-catalytic and catalytic reforming strategies applicable for biogas.
The document gives an overview of the μ-CHP system needs and formulates different strategies that can be used in the FC-District μ-CHP unit working with biogas.
The document provides typical biogas compositions highlighting harmful contaminants for the fuel processing components of the system and the required cleaning technologies to pre-treat the biogas.
The potential applicability of the biogas reforming strategies to FC-District μ-CHP system was assessed. The catalytic partial oxidation of biogas was found the most prominent technology to be applied in the FC-District μ-CHP unit.
The catalytic partial oxidation to reform biogas mixtures under the FC-District μ-CHP system was investigated experimentally and also numerically. Very good agreement between the numerical results and the experimental data was observed under operating conditions relevant to downstream project requirements.
Future activities to address the problem of replacing the utilization of conventional fuels, namely natural gas, by biogas mixtures in the μ-CHP system can be strongly supported on the present document.

1. Introduction

1.1 Biogas

Biogas consists in a mixture composed mainly by methane and carbon dioxide derived from the anaerobic decomposition of any organic biodegradable material (biomass) by the action of a population of microorganisms[1]. A large variety of feedstock has been considered suitable for the production of raw biogas such as animal manure, sewage sludge, municipal solid wastes, agro-industrial wastes, by-products from the production of biofuels and energy crops [171,173].
The composition of the raw biogas depends on several factors such as on the feedstock (substrate) composition, batch load, operating conditions and the technical specifications of the digester. Table 1 presents a typical range for the major components in the biogas composition. Traces of other compounds can also be found such as aromatics, sulphur compounds, higher hydrocarbons or siloxanes. A large collection for biogas (landfill gas) compositions can be found in Appendix II.

Table 1. Typical composition of biogas [171].

Component	Support
Methane (CH4)	55-65
Carbon dioxide (CO2)	35-45
Nitrogen (N2)	0-3
Oxygen (O2)	0-2
Hydrogen Sulphide (H2S)	0-1
Hydrogen (H2)	0-1
Ammonia (NH3)	0-1

The presence of hydrogen sulphide in the biogas composition is an issue that concerns the biogas applications. Hydrogen sulphide is a toxic, corrosive and malodourous component. Furthermore, regarding biogas applications involving the presence of catalysts, hydrogen sulphide in the feed stream can lead to the catalyst deactivation by poisoning. An extensive list of other contaminants and their potential for damaging reforming catalysts and anodic materials of the SOFC are presented in Appendix III.
Biogas is a promising fuel for a large number of applications. Biogas can be utilized for the production of heat and stream and/or for electricity generation/cogeneration in combined heat and power (CHP) applications. Several EU countries have recently initiated programs to increase biogas penetration in the transport sector [174-175]. Also, conventional gas burners can easily be adjusted for biogas operation by changing the air-to-gas ratio. Burning biogas is an established and trustworthy technology, with low demands on biogas quality. However this is not the case for biogas use in fuel cell systems. As stated above, fuel cells are considered to become the small-scale power plant of the future, having the potential to reach very high efficiencies and low emissions. Special interest for biogas is focused on hot fuel cells (>800 ºC), where CO_2 does not inhibit the electrochemical process but rather serves as a heat carrier. Generally, biogas has a low heating value, caused by the relatively high levels of carbon oxides and nitrogen. However, this

[1] A detailed description of the production process can be found in Appendix I.

drawback is not an issue for fuel cells, particularly the molten carbonate (electrolyte) fuel cell (MCFC) and solid oxide fuel cell (SOFC), which are able to handle very high concentrations of carbon oxides [176].
The contaminants presented in the raw biogas composition should be removed to a certain degree before biogas utilization. Depending on its initial composition[2] and its purpose there are several technologies that can be employed for biogas cleaning [173]. For the use of biogas/landfill gas in SOFC systems the required clean-up flux was proposed by OVM-ICCPET and it can be found in Appendix V.

1.2 SOFCs and fuel flexibility

Enhancing energy efficiency and promoting sustainability requires a thorough assessment of novel energy conversion concepts and technologies. Fuel cells are energy conversion devices converting the chemical energy of a hydrocarbon fuel into electricity and heat through a series of thermo-chemical and electrochemical reactions. There are several types of fuel cells, mainly differentiated by the type of electrolyte and the range of operating parameters, such as primary fuel feed and stack temperature (e.g. [176]). Solid-oxide-fuel-cells (SOFC), in particular, have two unique characteristics that make them ideal candidates for a number of applications in the energy sector. They are solid devices without any moving parts and operate at relatively high temperatures (650-1000 ^{o}C) over varying load conditions, yielding exploitable heat and electricity (e.g. [175]). As such, their operation is not limited by second law considerations and they can achieve very high efficiencies, particularly at low to intermediate powers. Furthermore, small scale SOFC systems of the order of a few kW are potentially ideal candidates for decentralized microcogeneration (μ-CHP) systems, also at domestic or district scales, producing both heat and electricity in a certain ratio to each other, providing potential reductions in carbon emissions and costs by generating both heat and electricity locally with efficient fuel use and by offsetting the use of centrally generated electricity from the grid (e.g. [177]).
Over the last decade, SOFC technology has reached a certain degree of maturity both at component and system level. Note that fuel flexibility in SOFC systems, is essential, particularly in their operation at district level, where specific fuel availability may be limited or constrained. In principle, SOFCs can operate over a wide range of fuels. Recently, there is a growing interest in developing fuel flexible systems capable of operating with highly variable and potentially low quality fuels, while also producing minimal air pollutants [178]. SOFCs can operate either on hydrocarbon or reformed-hydrocarbon fuels. Due to their high operating temperatures, SOFC operation directly on hydrocarbon fuels is possible, e.g. [179], but practical systems rely entirely on fuel reforming processes in order to convert the fuel into hydrogen and/or syngas, e.g. [180]. Syngas mixtures, in particular, are ideally suited for use in SOFC systems, with pure CO also being a viable option [181]. Currently, methane is the fuel of choice in fuel cell applications mainly in view of its high hydrogen to carbon ratio (e.g. [182]). Reforming of higher pure hydrocarbons (e.g. butane) and practical fuels (e.g. gasoline and diesel) is also an option but has been shown to result in a reduced overall fuel conversion into hydrogen [182].
On the other hand, the use of alternative, non-fossil fuels as syngas sources to feed SOFC systems is steadily increasing due to energy security and supply issues as well as concerns about climate change. Renewable methane sources, such as biomass or biogas from anaerobic digestion gas from municipal waste incinerators [176], can also be utilized as syngas sources to

[2] Appendix IV presents standars for sampling and measurement of biogas contaminants.

feed SOFC systems [183]. Synthetic natural gas (SNG) and biogas produced from biomass are promising, environmentally-friendly, alternative fuels for use in SOFC applications, particularly for small scale domestic applications. For example, bio-alcohols constitute an additional possibility. Ethanol in particular, is a renewable fuel, provided it is derived from feedstock, biomass (e.g. [184]) and waste products (e.g. [185]), and has a high enough hydrogen content in order to be a candidate for hydrogen production in fuel cell systems through a reforming process (e.g. [186]). Essentially, any mixture rich enough in H_2 and CO that does not lead to carbon deposition in the anode can in principle be utilized in SOFCs, e.g. [187].

Although internal reforming directly at the stack of large-scale systems is possible, and has been demonstrated (e.g. [188]) for a variety of fuels, from natural gas to alcohols and practical transportation fuels [180,189], external reforming is generally preferable, at least in cases where fuel flexibility is a prerequisite, owing to the relatively high operating temperatures and the increased risk of carbon deposits and anode deactivation [181], associated with the former. Generally, available reforming technologies include steam reforming (SR), partial oxidation (POx) and autothermal reforming (ATR) (e.g. [175-176]). The exothermic POx process appears advantageous in terms of system complexity and integration, also having good dynamic response to load variation. In order to enhance POx reforming efficiency, catalysts are widely used, but suffer from poisoning and age degeneration. Moreover, catalysts are specific to the particular primary fuel and reforming application. On the contrary, an alternative thermal POx (TPOx) reformer appears to be a proper solution towards an SOFC fuel flexible system.

1.3 Objectives

The present document intends to provide the state-of-the-art of external reforming technologies with potential for SOFC systems. Reforming technologies for common and alternative hydrocarbon fuels with and without the requirement of catalysts are revisited. Among the non-catalytic reforming technologies the benefits of thermal partial oxidation and pyrolysis are extensively discussed while for catalyst aided reforming strategies CO_2 reforming, steam reforming, catalytic partial oxidation and autothermal reforming are examined. In particular, a numerical assessment for the potential of catalytic partial oxidation with biogas in the FC-District μ-CHP unit is also presented.

1.4 Document organization

This deliverable is organized in 5 sections. Besides the introductory section, section 2 and 3 are concerned with the non-catalytic and catalytic reforming technologies, respectively, section 4 discusses the applicability of biogas catalytic partial oxidation for the FC-District μ-CHP system. Summary conclusions are drawn in section 5.

2. Non-catalytic reforming strategies of biogas

As also stated in the introduction of this deliverable, the exothermic POx process appears advantageous in terms of system complexity and integration, also having good dynamic response to load variation. In order to enhance POx reforming efficiency, catalysts are widely used, but suffer from poisoning and age degeneration. Moreover, catalysts are specific to the particular primary fuel and reforming application. In order to take full advantage of the SOFC fuel flexibility capability, an alternative thermal POx (TPOx) reformer appears to be a proper solution. The operation of such a reformer, either as a standalone unit [190-191] or as an integral part of a prototype SOFC system [192-193] has been extensively studied. A TPOx reactor is in ideal agreement with the desired SOFC fuel interchange-ability, as it is very fuel flexible since the fuel conversion and product yield depend on operating parameters and are not constrained by potential fuel-catalyst incompatibilities. In order to achieve efficient operation in the absence of a catalyst, high temperatures in excess of 1000 K (ca. 1300 $^{\circ}$C) are required. This is not an issue in SOFC systems since they already operate at elevated temperatures. However, high temperatures combined with fuel rich reformate mixtures provide ideal conditions for carbon deposits. Efficient operation of the fuel cell system requires not only optimization of the hydrogen/syngas yield, under a wide range of operating conditions, but also minimization of the potentially harmful carbonaceous species formation. The total amount of carbon at the reformer exit is of major importance since the mixture is subsequently fed into to the porous anode (e.g. [180]) where electrochemical oxidation takes place.

Previous numerical studies on the thermo-chemical behaviour of integrated SOFC systems have revealed that significant chemical activity takes place, not only in the reformer and the off-gas burner, but also in several auxiliary components, such as the connecting pipes between the reformer and the stack (e.g. [192]). The extent of such chemical activity largely controls efficiency and can also result in highly undesirable kinetically controlled processes, such as ignition and soot formation, anywhere in the system. In order to study and predict such thermo-chemical behaviour, a solely thermodynamic approach is not sufficient, and can, at best, provide limited information for syngas yield, and only under a narrow range of operating conditions. Instead, a detailed kinetic methodology is essential for accurate predictions and a complete representation of both fuel conversion and carbon formation processes. This is even more the case when evaluating advanced fuel cell operation concepts, including mass integration (e.g. [194-195]). Mass integrated SOFC systems, incorporate anode flue gas recirculation in order to improve system efficiency and avoid carbon deposition within the reformer and the stack [195]. Such systems operate very close to the carbon deposition limit, thus requiring efficient control strategies (flue gas composition and enthalpy state determination, dilution rate and so on) that can only be properly defined by resorting to detailed chemical considerations.

In the following section (section 2.1) a comparative study of the non-catalytic POx reforming operation with conventional (methane) and alternative (biogas, methanol and ethanol) fuels is presented. The reforming performance for each fuel is characterized on the basis of syngas yield, reforming efficiency and pollutants formation. Section 2.2 focuses on the experimental and numerical investigation of non-catalytic pyrolysis of methane mixtures at atmospheric pressure in an isothermal plug flow reactor (PFR).

2.1 Assessment of the reforming potential of common fuels for practical applications

While biogas has been considered for use in SOFC with almost all catalyst-based reforming technologies, relevant studies focusing on the non-catalytic biogas TPOx reforming are lacking. In order to explore the potential of biogas TPOx reforming for SOFC applications, a comparative computational assessment of biogas as compared to methane, methanol and ethanol has been conducted. Comparisons with other commonly used fuels in SOFCs, provides an excellent starting point for further studies of biogas utilization in real practical reformers, since it can provide solid methodological guidelines that can be applied for an optimal system design.

The present study on the assessment of the reforming potential of common fuels for practical applications is organized as follows: the numerical methodology is described first (section 2.1.1), followed by numerical computations regarding the onset of ignition (section 2.1.2) and finally by a detailed kinetic evaluation of the reforming process (section 2.1.3).

2.1.1 Numerical methodology

In order to assess the TPOx reforming potential of common fuels, two kinds of computations have been performed in this work. The first relates to the quantification of the ignition propensity of the fuel mixtures considered, for typical TPOx conditions. This would provide rough guidelines for the operation of real reforming devices. The onset of ignition has been investigated through transient calculations in a closed, constant pressure, adiabatic, perfectly stirred reactor (PSR). Computations have also been performed in an isothermal, atmospheric pressure plug flow reactor (PFR) in order to provide a detailed representation of fuel fate and product formation within the TPOx reactor. The results of these computations will lead to an accurate prediction of product yield, conversion efficiency and carbonaceous species formation tendency. For both numerical investigations, a wide range of operating conditions have been considered; initial temperatures from 650 K to 1500 K, fuel – air mixture stoichiometries in the range ϕ = 2 - 6. In the context of the present work stoichiometry is expressed in terms of the equivalence ratio, defined as the actual (mass) fuel-to-air ratio over the stoichiometric fuel-to-air ratio.
The chemistry model used has been mainly developed in order to describe the combustion chemistry of hydrocarbon fuels and has been demonstrated to accurately describe chemistry relevant to SOFC components and systems processes, in the operational range of the latter. The mechanism has been extensively validated against experimental speciation data from laminar counterflow, premixed flames and shock tubes, including laminar flame speeds and ignition time delays, as well as from perfectly stirred and plug flow reactors, all under a wide range of temperatures, pressures and stoichiometries. During the last years the mechanism has been exploited in order to describe the combustion chemistry of conventional, i.e. methane [190], ethane [196], allene and propyne [197-198], benzene [199], and alternative, i.e. biogas [196], methanol [197-198], ethanol [200], fuels. The mechanism has also been supplemented with sub-models for polycyclic aromatic hydrocarbons (PAH) [201], NO_x chemistry [169] and for poly-chlorinated dioxins and furans (PCDD/F) [202]. The mechanism currently consists of 1150 reactions among 191 species and is available from the authors upon request. All computations have been performed with CHEMKIN [203]

2.1.2 Onset of ignition

The present section presents fundamental computations relating to the onset of ignition in the reformer. The onset of ignition is defined as the time corresponding to the maximization of the temporal temperature derivative in the closed adiabatic PSR against residence time. The latter parameter has been limited to 1 s, which is also the order of magnitude of typical SOFC reforming applications, e.g. ([175,193]). Computations are presented for initial temperatures ranging from 650 K to the highest temperature, for each fuel, for which ignition occurs after a predefined time interval. For the present work, this time has been set to 5 ms. For higher temperatures, the model predicts an instantaneous ignition. Results are presented in Figure 1 for all four fuels and for a stoichiometry of $\phi = 2$.

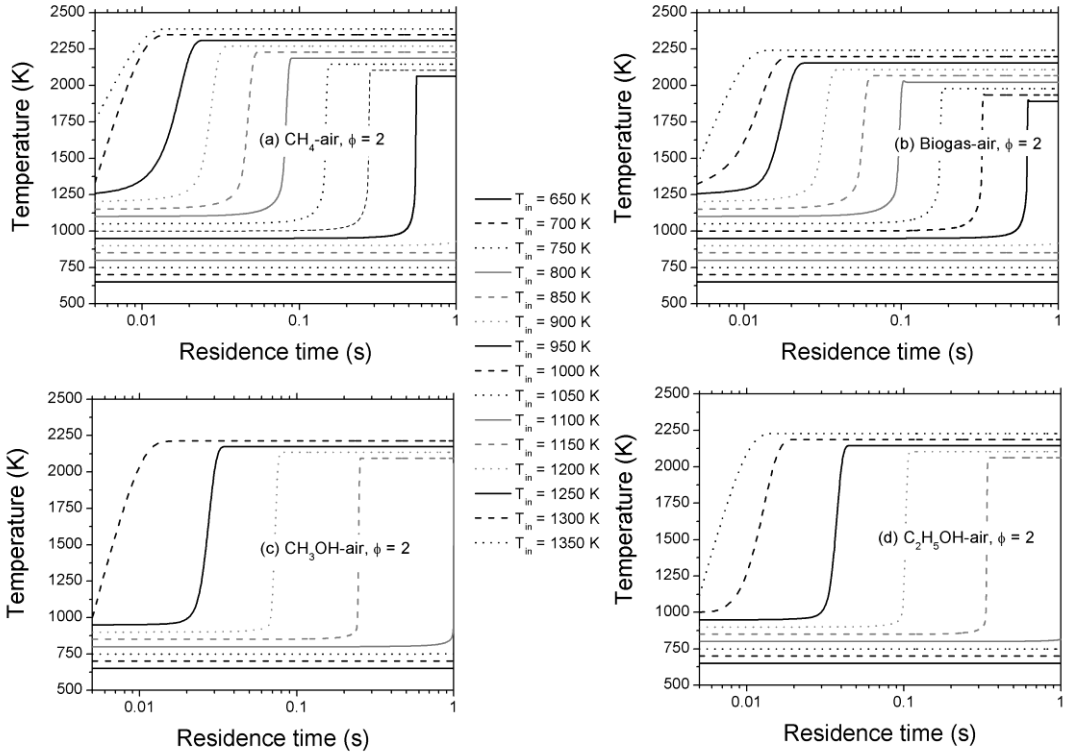

Figure 1. Temperature evolution as a function of time in a closed PSR for initial temperatures from T_{in} = 650 K to the highest T_{in} where ignition occurs after 5 ms (see text). (a) methane (b) biogas (c) methanol (d) ethanol.

As generally expected, induction time becomes shorter as the initial temperature increases. Methane and biogas feature similar, relatively long, induction times, while both alcohols ignite much faster. For example, at a temperature of 1000 K, methane and biogas ignite at approximately 300 ms, while ethanol ignites at less than 20 ms and methanol at less than 10 ms. These qualitative trends are directly related to differences in fuel reactivity. The above values are also in qualitative agreement with fundamental studies of ignition delay times in shock tubes (e.g [204-205]). Also note that these values constitute a lower limit for the induction time since in practical applications finite heat losses control system reactivity. However, it could be anticipated that the above trends would also be applicable for real systems. Finally, it can be argued that, reforming systems specifically designed for operation on relatively unreactive fuels may suffer the risk of undesired ignition, when operated with other fuels.

2.1.3 Detailed kinetic assessment of the reforming process

2.1.3.1 Fuel conversion and syngas formation processes

A numerical assessment of the reforming process in a single PFR for the four fuels considered here have been performed by using the developed C_1-C_6 detail kinetic mechanism. Computations were carried out under isothermal conditions for all fuel–air mixtures for temperatures of 650 to 1500 K, mixture stoichiometries of ϕ = 2–6 and for residence times up to 10 s. Typical computed H_2 and CO exhaust levels at a stoichiometry value of ϕ = 2, are presented in Figures 2 and 3 respectively, for all fuels.

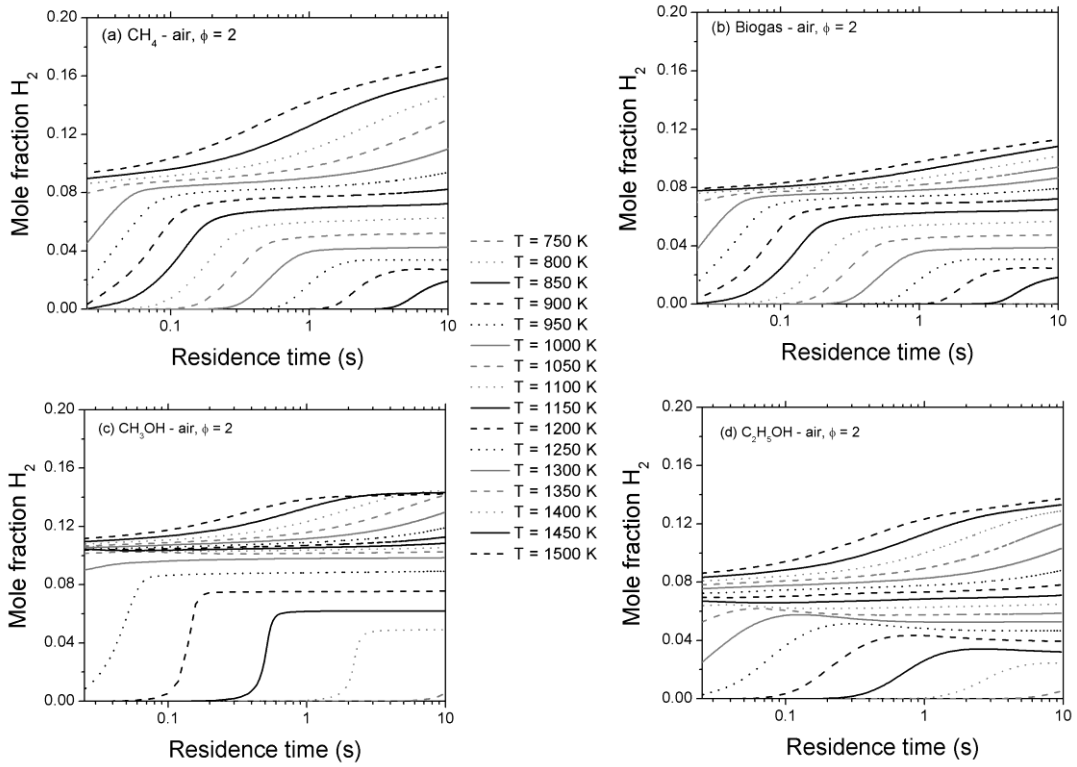

Figure 2. Computed H_2 mole fraction profiles as a function of time in a PFR for temperatures in the range 750 – 1500 K and for a stoichiometry of ϕ = 2. (a) methane (b) biogas (c) methanol (d) ethanol.

Hydrogen levels increase almost monotonically as temperature and residence time increase for all fuel mixtures. This is clearly the case for methane and biogas. For the two alcohols considered here, hydrogen levels sharply increase for low and high temperatures, while remain essentially constant over the intermediate temperature regime, irrespective of residence time value. Methane reforming results in approximately 10% more H_2, on a molar basis, for lower temperatures, to almost 40%, at higher temperatures, as compared to biogas. Methanol and ethanol produce similar amounts of hydrogen at high temperatures, with methanol producing twice as much hydrogen as compared to ethanol at lower temperatures, due to its higher reactivity. Note that, for low to intermediate temperatures (up to 1200 K), methanol produces generally more H_2 than methane, while, methane is clearly superior at very high temperature. It is also noteworthy, that with increasing temperature, there is not a significant increase in the H_2 levels for alcoholic fuels

reforming, as it is the case for methane. This is due to the fact that high temperature conditions accelerate the high activation energy molecular elimination reactions R93, R153 and R182, which feed the system with reactive H radicals, that in turn attack both the remaining methane and stable C_2 molecules that have been also produced by high activation energy recombination reactions. The major H_2 production sequence is outlined below.

$$CH_3 + H\ (+M) = CH_4\ (+M) \quad \text{(R93)}^3$$
$$C_2H_3\ (+M) = C_2H_2 + H\ (+M) \quad \text{(R153)}$$
$$C_2H_4 + H\ (+M) = C_2H_5\ (+M) \quad \text{(R182)}$$
$$CH_3 + CH_3\ (+M) = C_2H_6\ (+M) \quad \text{(R80)}$$
$$CH_4 + H = CH_3 + H_2 \quad \text{(R94)}$$
$$C_2H_4 + H = C_2H_3 + H_2 \quad \text{(R163)}$$
$$C_2H_6 + H = C_2H_5 + H_2 \quad \text{(R184)}$$

In the case of alcohols, the fuel bound oxygen prevents the attainment of pyrolytic conditions, and does not allow the above described sequence to be activated at high temperatures. Hydrogen production path ways are similar for both low and high temperatures.

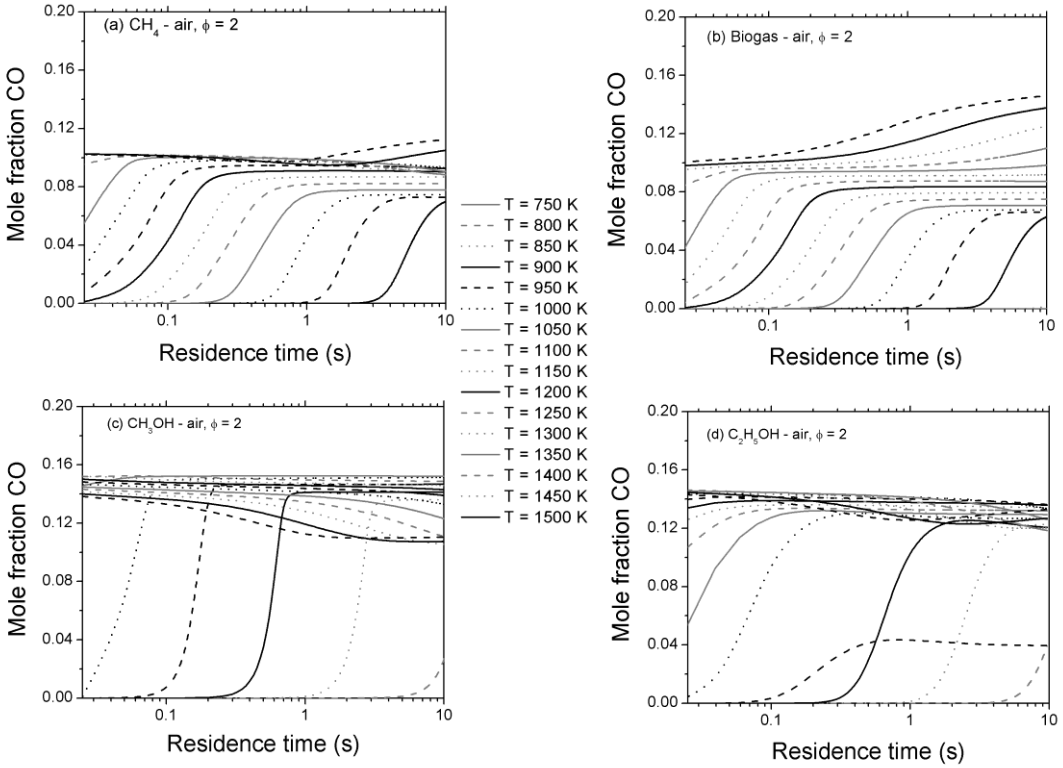

Figure 3. Computed CO mole fraction profiles as a function of time in a PFR for temperatures in the range 750 – 1500 K and for a stoichiometry of $\phi = 2$. (a) methane (b) biogas (c) methanol (d) ethanol.

On the other hand, CO yield (Figure 3) does not follow the same trends as compared to H_2. For all fuels examined, with the exception of biogas, CO levels appear to be independent of reforming temperature at longer residence times. In fact, CO formation in alcohols is practically instantaneous under high temperatures, and decreases as residence time becomes longer.

[3] Reaction numbering in the present document follows the original listing published in [199].

Overall, it is clear that the reforming of alcohols results in significantly higher CO levels than methane. For example, and at a temperature of 1200 K and a residence time of 1 s, exhaust CO values for methanol and ethanol reforming are around 15%, while for the case of methane is less than 10%. Biogas is considered to be a distinct case due to the presence of CO_2 in the initial fuel composition. For this reason, CO is constantly increasing as reforming temperature and reactor residence time increase.

Kinetic arguments can be used to scrutinize the above convoluted picture. Thus, in the case of methane, a molecular growth path, initiated by CH_3 formation accounts for almost the entire CO formation, over the whole residence time domain. In particular, initial methane fuel is consumed to the methyl radical through mainly the H abstraction reaction R94. Subsequently, methyl radical recombination to C_2H_6 (reaction R80) initiates the C_2 chain down to the formation of acetylene. The latter is qualitatively consumed to HCCO which eventually decomposes to CO as it is summarized in the sequence below.

$$C_2H_2 + O_2 = HCCO + OH \quad \text{(R150)}$$
$$CH_2CO + H = HCCO + H_2 \quad \text{(R204)}$$
$$HCCO + O_2 = CO + CO + OH \quad \text{(R196)}$$
$$CH_2CO + H = CH_3 + CO \quad \text{(R203)}$$
$$HCO + M = CO + H + M \quad \text{(R104)}$$

At higher temperatures, the recombination sequence is accelerated, feeding the above chain with extra carbonaceous species, e.g.

$$C_2H_5CO = CH_2CO + CH_3 \quad \text{(R427)}$$
$$C_2H_5CO = C_2H_5 + CO \quad \text{(R428)}$$

As it is shown in Figure 3, methanol reforming leads to higher CO levels than in the case of methane. This can be attributed to the initiation of a secondary reaction route, linked with the oxygenated nature of alcoholic fuels. In particular, apart from the molecular growth sequence initiated by CH_3 radical recombination, described above, an additional chemical path, through hydroxy-methyl (CH_3O) formation and subsequent consumption of the latter to formaldehyde and formyl radical and eventually to CO, is being activated.

$$CH_3OH + H = CH_2OH + H_2 \quad \text{(R125)}$$
$$CH_2OH + M = CH_2O + H + M \quad \text{(R116)}$$
$$CH_2O + H = HCO + H_2 \quad \text{(R105)}$$
$$HCO + H = CO + H_2 \quad \text{(R99)}$$
$$HCO + M = CO + H + M \quad \text{(R104)}$$

However, at the higher investigated temperatures, two observations can be made: there is a lack of a molecular growth path, as in the case of methane, and at the same time, the radical pool formation initiates CO conversion to CO_2. The combination of the above two effects lead to a drop in CO levels at longer residence times. Note that there is a striking similarity between methanol and ethanol in terms of CO levels. However, the absence of the pronounced CO drop at longer residence times in the case of ethanol is due to the fact that CO formation in ethanol is less dependent on the CH_2O formation path, as described above, than in methanol. Furthermore, the molecular growth route to CO, as described for the case of methane, contributes appreciatively due to the larger amounts of carbon contained in the ethanol molecule.

In biogas, the same qualitative observations made for methane are still valid, the only difference being that due to the significant CO_2 levels (initially present in the fuel mixture), CO is being continuously formed, at the expense of H_2. It is interesting to investigate the fate of CO at longer residence times. Reaction path analysis reveals that CO is being formed through the reaction CO+OH = CO_2+H (reaction R23). This reaction, under the conditions encountered in the present work, is under partial equilibrium, and since CO_2 reaches significant levels, and H radical features two orders of magnitude higher concentration than OH radical, CO formation is favoured.

The above detailed analysis offers valuable information regarding the design and optimization of a fuel reforming process. Alcohols are more reactive than methane, resulting in an overall higher syngas yield under most conditions of relevance. The relative unreactiveness of methane can be explained by the fact that, the formation of a series of stable C_2 and C_3 intermediate species delays the overall fuel conversion process, resulting to a later CO growth. Thus, in terms of syngas yield, the only operating conditions that methane is superior, is the high temperature and long residence time regime. On the other hand, if shorter residence times and/or lower to intermediate temperatures are required, then alcohols are the fuel of choice. Note that biogas can also be a viable option since it can compensate for the low CO yield of pure methane.

Apart from H_2 and CO, the reforming process results in a range of other species. This is of particular importance when integration of the components to a system level is concerned. The species distribution across the PFR at a particular residence time would correspond to the composition of the exhaust mixture for a reformer featuring the same residence time. Figure 4 presents species distribution, for all four fuel mixtures, at a residence time of 500 ms, for a typical TPOx reformer operation temperature of T = 1200 K and an initial mixture stoichiometry of ϕ = 2. Only species with molar concentration higher than $1.0 \cdot 10^{-3}$ are shown. Alcohol reforming results indeed in a higher syngas yield (H_2+CO) than methane and biogas. It is also interesting to note that, methane exists in considerable quantities, either as a non-reacted fuel (methane and biogas cases), or as an intermediate product of the fuel conversion process (alcohols cases), whereas methanol and ethanol are depleted in much shorter residence time. Further, methanol is characterized by a complete absence of C_2 species.

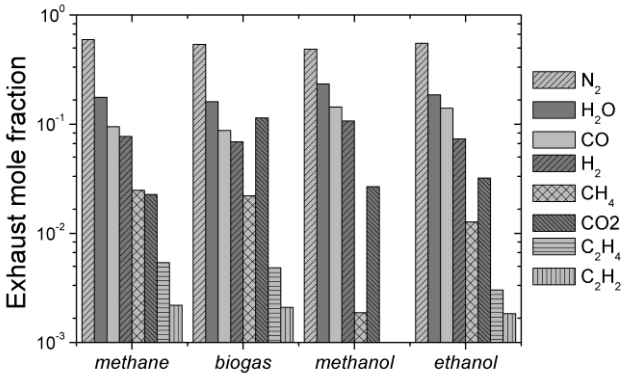

Figure 4. Computed exhaust species mole fraction profiles for a typical TPOx reformer having a characteristic residence time of 500 ms.

2.1.3.2 Molecular growth processes

Molecular growth processes are an inherent part of the fuel conversion process as shown above for the case of CO formation. Such processes can be either beneficial or detrimental for the overall reforming efficiency depending on the particular operating conditions. However, they invariably lead to the formation of a sequence of high molecular weight species, eventually leading to PAH (polycyclic aromatic hydrocarbon) and soot formation. Soot formation is a complicated process. Nonetheless the soot tendency of a particular fuel can be correlated to the evolution of several indicative species. These are benzene, a safe indicator of soot nucleation, acetylene, a marker for soot mass growth, and higher PAH species such as pyrene ([206]).

Figure 5 presents the temporal evolution of benzene for all four fuels, at an initial mixture stoichiometry of $\phi = 4$, and in the temperature range of T = 1100 – 1500 K. The above stoichiometry has been chosen in order to better highlight the underlying principles, since molecular growth effects are more pronounced for richer mixtures. The most striking observation is that methane, biogas and ethanol generally exhibit similar peak benzene levels, of the order of $1.0 \cdot 10^{-3}$, whereas benzene levels in methanol reforming are three orders of magnitude lower. This is linked to benzene formation paths which, for most hydrocarbons, are initiated by recombination reactions involving acetylene and ethylene, leading to the formation of the resonance-stabilized propargyl (C_3H_3), cyclopentadienyl (C_5H_5) and benzyl (C_7H_7) radicals, and through them to benzene. The virtual absence of benzene in methanol reforming is thus associated with the corresponding very low levels of C_2 hydrocarbons, as shown in Figure 4.

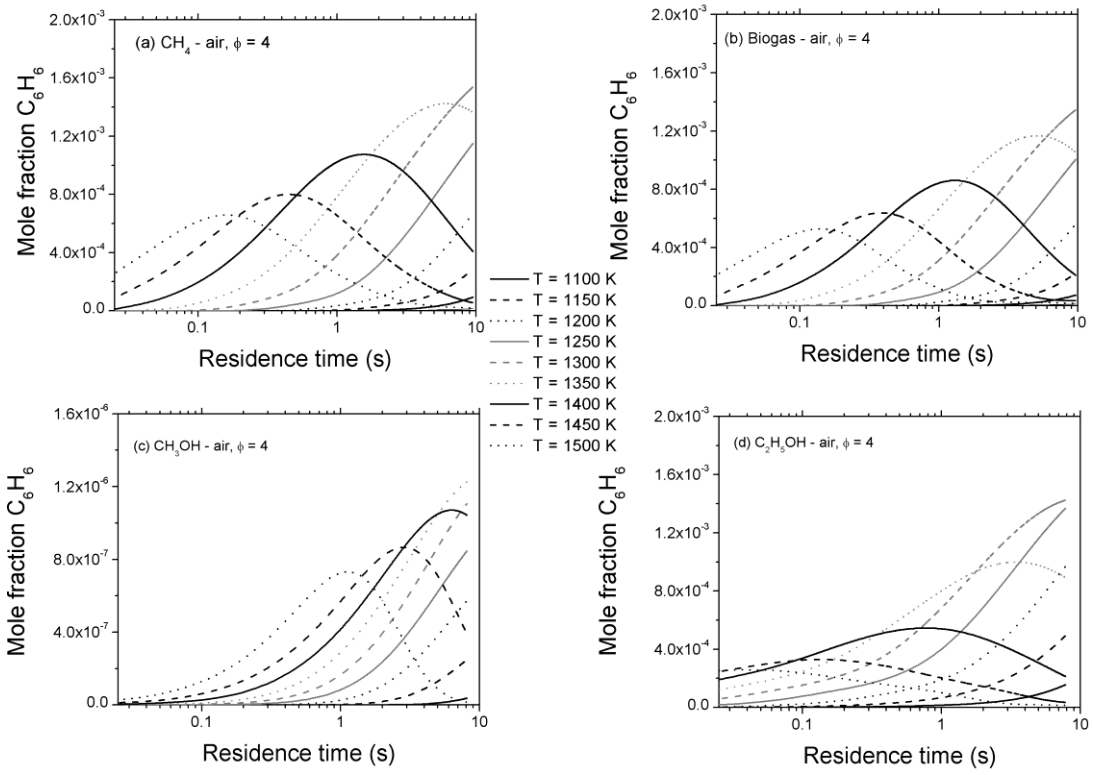

Figure 5. Computed C_6H_6 mole fraction profiles as a function of time in a PFR for temperatures in the range 750 – 1500 K and for a stoichiometry of $\phi = 4$. (a) methane (b) biogas (c) methanol (d) ethanol.

In contrast to syngas formation processes, peak benzene levels are not observed at the highest operation temperature. Instead, for most cases, benzene levels increase as a function of residence time, reach a maximum and then decrease. The benzene peak location is shifted towards shorter residence times, as temperature increases. For example, in the case of methane and for a temperature of T = 1350 K, benzene reaches its peak levels after approximately 6 s, while for a temperature of T = 1500 K peak location occurs at around 0.15 s.

For the other three remaining fuels, different characteristics in the temporal evolution of benzene do exist. Benzene formation in biogas–air mixtures features the same qualitative behaviour as in methane mixtures, with peak levels only marginally reduced (approximately 10%). For ethanol mixtures, benzene is formed generally earlier than methane. For example, for a temperature of T = 1200 K and a residence time of 1 s, benzene levels in the case of ethanol are four times higher than in the case of methane. There is also some difference in the relative formation paths. Benzene in methane mixtures mainly comes from recombination reactions involving C_3 species, namely propargyl radical recombination ($C_3H_3+C_3H_3$) and propargyl radical addition to allene ($C_3H_3+a\text{-}C_3H_4$) leading to a series of isomerisation reactions of C_6H_6 species, and eventually to benzene. Of almost equal importance is the additional path outlined below, also initiated by the C_3 chain, and passing through C_5 and C_7 intermediates.

$$a\text{-}C_3H_5 + C_2H_2 = c\text{-}C_5H_6 + H \quad \text{(R599)}$$
$$c\text{-}C_5H_6 + H = C_5H_5 + H_2 \quad \text{(R602)}$$
$$C_5H_5 + C_2H_2 = C_7H_7 \quad \text{(-R748)}$$
$$C_7H_7 + H = C_7H_8 \quad \text{(R751)}$$
$$C_7H_8 + H = C_6H_6 + CH_3 \quad \text{(R736)}$$

The above sequence accounts also for more than 60% of the benzene formation rate in the case of ethanol, while the remaining coming via recombination of C_2 species through the sequence:

$$C_2H_3 + C_2H_2 = C_4H_4 + H \quad \text{(R467)}$$
$$C_4H_4 + C_2H_3 = C_6H_6 + H \quad \text{(R655)}$$

The above discussion can be linked to the quantitative differences related to syngas and benzene formation in methane and ethanol reforming. In the case of methane, benzene formation precedes syngas formation. This is due to the pyrolytic nature of rich methane reforming and is even more pronounced at higher temperatures, where the prominent role of the recombination reactions promote the formation of higher order species, not only enhancing benzene, but also late CO (e.g. R427 and R428) and H_2 (via abstraction channels, e.g. R163 and R184) formation, as described in some detail in the previous section. Ethanol reforming is more oxidative in nature, characterized by an early shedding of CO (and H_2) molecules and a delay of recombination reactions.

The effect of mixture stoichiometry on reformate composition has also been numerically investigated. Figures 6 and 7 illustrate the variation in hydrogen and carbon monoxide levels respectively, for rich (ϕ = 2–6) methane–air, biogas-air, methanol-air and ethanol–air and mixtures, under high temperature (T = 1200 K) conditions. In general, syngas yield is roughly proportional to mixture stoichiometry for all fuels, and especially for the case of methanol. Hydrogen yield appears to be insensitive to stoichiometry values under very rich conditions (ϕ = 4 and ϕ = 6) for methane based fuels. However, for the methane and biogas cases, what is earned for richer mixtures in terms of syngas from the H_2 increase, is compensated by the slight drop in CO levels. Note that for residence times longer than 1 s, all H_2 and CO profiles reach a plateau. This is more pronounced

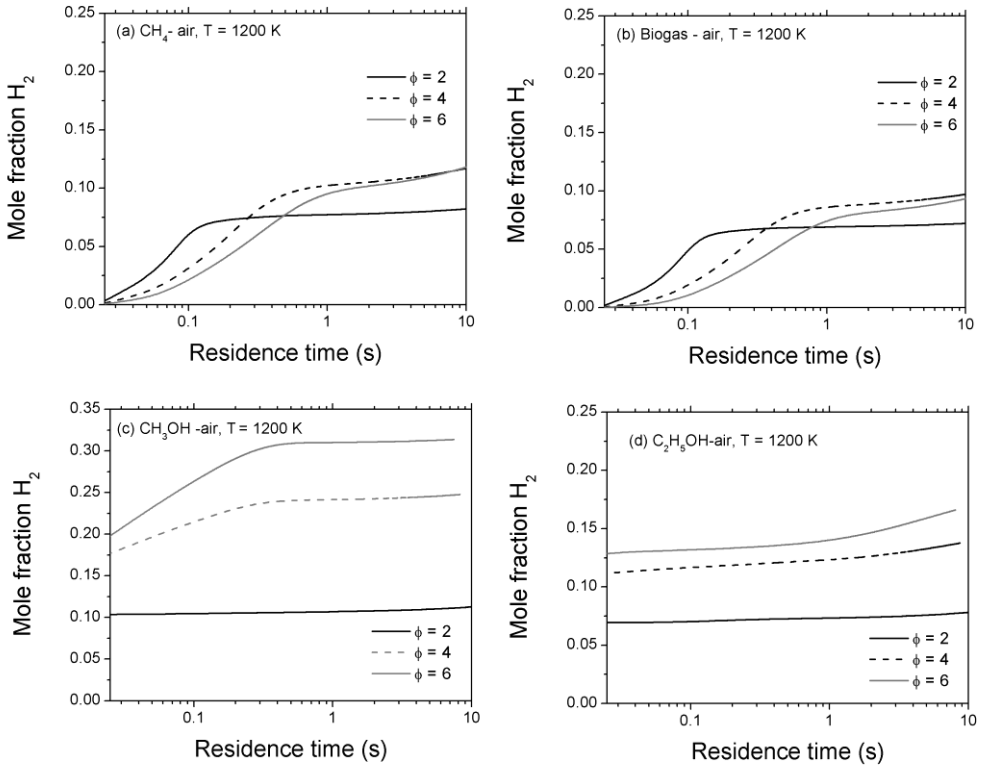

Figure 6. Computed H_2 mole fraction profiles as a function of time in a PFR for temperatures of 900 K and 1200 K and for a stoichiometry range of ϕ = 2 – 6. (a) methane (b) biogas (c) methanol (d) ethanol.

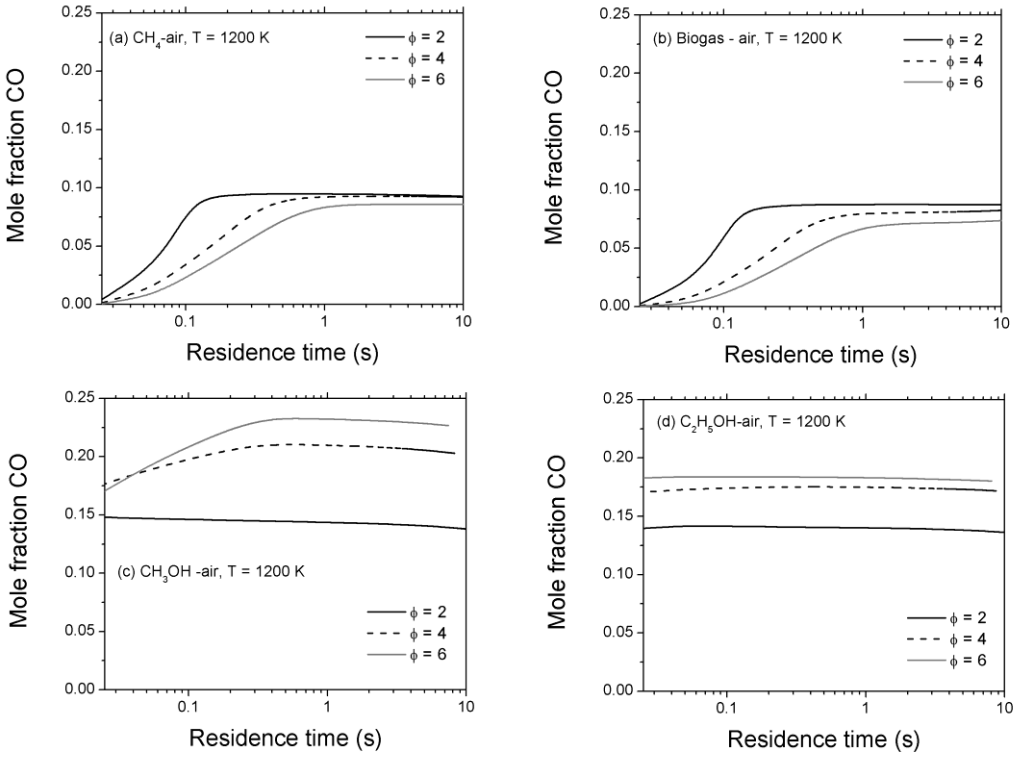

Figure 7. Computed CO mole fraction profiles as a function of time in a PFR for temperatures of 900 K and 1200 K and for a stoichiometry range of ϕ = 2 – 6. (a) methane (b) biogas (c) methanol (d) ethanol.

for the case of ethanol, where, under the conditions encountered presently (T = 1200 K), both species are very sharply formed early in the process and reach nearly constant values.
Stoichiometry also has an effect on benzene concentration as shown in Figure 8. There is a qualitative difference between methane and biogas on one hand and ethanol on the other. For the ethanol case, there is constant increase in benzene levels as stoichiometry increases whereas, for methane and biogas, no further increase is observed for stoichiometry higher than $\phi = 4$. The latter variation is reminiscent of a similar variation in syngas yield.

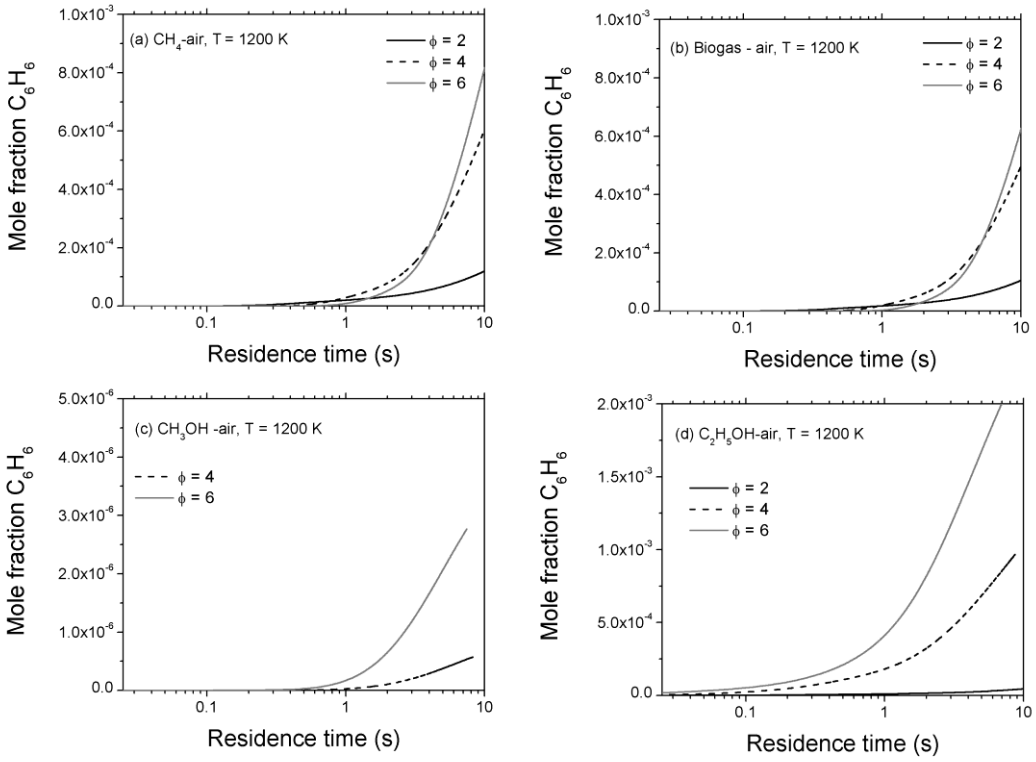

Figure 8. Computed C_6H_6 mole fraction profiles as a function of time in a PFR for temperatures of 900 K and 1200 K and for a stoichiometry range of $\phi = 2 – 6$. (a) methane (b) biogas (c) methanol (d) ethanol.

2.1.3.3 Efficiency

The above discussion has provided a detailed picture of the fuel conversion, syngas formation and molecular growth processes for the reforming of four commonly used fuels. However, absolute yield values can only provide information about the chemical activity of a particular fuel, and cannot be used to compare fuels having different energy content. An appropriate expression for reformer efficiency, taking into account the energy content of each fuel, has been defined as:

$$\eta_{ref} = \frac{LHV_{H_2}.\dot{m}_{H_2} + LHV_{CO}.\dot{m}_{CO}}{LHV_{fuel}.\dot{m}_{fuel}} \quad (1)$$

where LHV_i and m_i are the lower heating value (expressed in MJ/kg) and the mass flow rate (kg/s) of species *i* respectively. Typical results for all fuel mixtures, under rich $\phi = 2$ and $\phi = 4$ conditions and for temperatures of 900 K and 1200 K are shown in Figure 9.

Generally, methane and biogas exhibit very similar behaviour whereas methanol and ethanol do have some marked differences among each other but also as compared to methane and biogas. For the low temperature cases, the efficiency of both alcohols increases sharply before reaching a plateau. On the other hand, due to their relative reduced reactivity, methane and biogas delay to attain constant efficiency levels. For example, after a period of 3 s, for the T = 900 K and $\phi = 2$ case, methane and biogas feature only about 80% of their maximum efficiency value, while both alcohols have already reached their peak efficiency. This results in efficiency values, at that particular residence time, of ca. 45% for methane and of about 55% for the methanol case. Moving to higher temperatures, the most striking observation is the extremely high efficiencies in the cases of methane and biogas, which reach values of the order of 95%. This is due to relative sharp increase in reactivity exhibited by methane, as a function of temperature. On the other hand, increasing the temperature does not result in any appreciable change in the plateau values of ethanol and methanol efficiencies. The only effect is the almost instantaneous attainment of the above values and the rapid expulsion of CO in very short residence times, as explained in the previous section. Stoichiometry effects are more pronounced in the case of methane and biogas. For example, at a residence time of 5 s, a doubling in stoichiometry halves efficiency. This is attributed to the strong coupling between syngas production and molecular growth processes. On the other hand, for the same stoichiometry change, methanol efficiency increases form 65% to 80%. This is due to the fact that syngas production and molecular growth processes are completely decoupled.

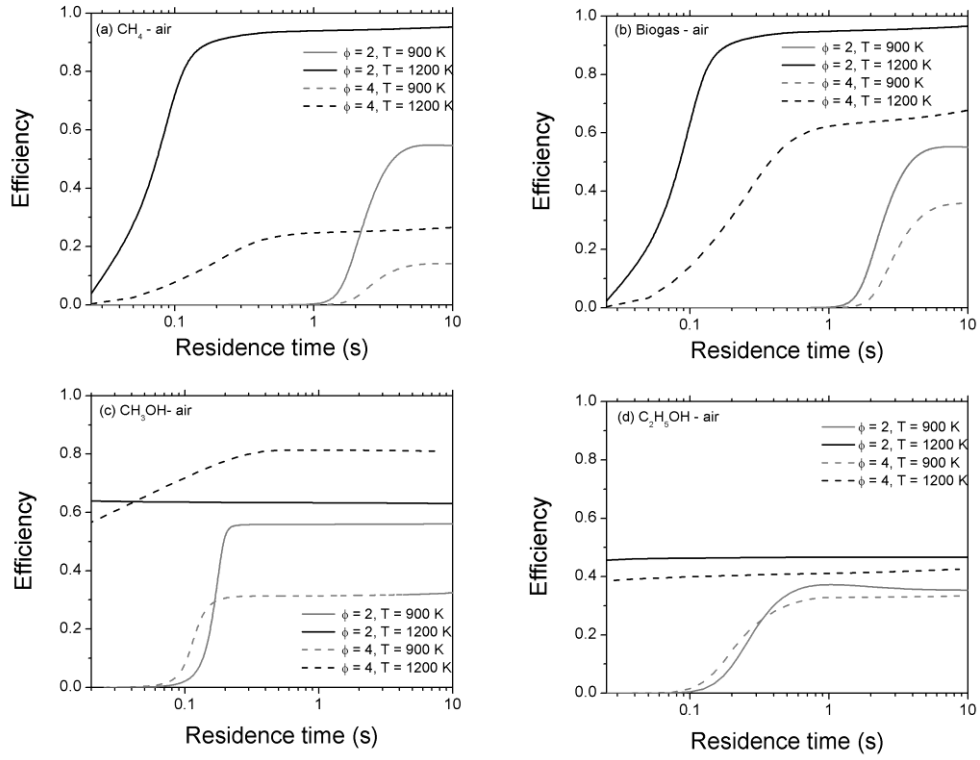

Figure 9. Computed efficiencies as a function of time in a PFR for temperatures of 900 K and 1200 K and for a stoichiometries range of $\phi = 2$ and $\phi = 4$. (a) methane (b) biogas (c) methanol (d) ethanol.

It is interesting to note that, for the temperature and stoichiometry range considered in the present study, efficiency values are significantly removed from their thermodynamic equilibrium values for all four fuels, see Table 2. The thermodynamic efficiency of each fuel is mainly independent of the operating temperature value, while this is not the case for the kinetically determined efficiency. On the other hand, as already discussed for the kinetically determined efficiency, the stoichiometry value has a strong influence on the thermodynamic efficiency for all four fuels considered. Generally, biogas and methanol have a somewhat higher thermodynamic efficiency than methane and ethanol respectively, for all cases considered. In particular, biogas appear to feature a greater than one thermodynamic efficiency value for the richer and higher temperature case, but this is due to the reforming efficiency definition. Finally note that the difference between the thermodynamic and kinetically determined efficiency values is more pronounced in short residence times.

Table 2. Equilibrium reforming efficiency values for the cases considered in Figure 9.

Stoichiometry	Temperature (K)	Methane	Biogas	Methanol	Ethanol
$\phi = 2$	900	0.669	0.697	0.641	0.622
	1200	0.668	0.699	0.641	0.621
$\phi = 4$	900	0.934	0.973	0.937	0.907
	1200	0.977	1.015	0.940	0.909

The obtained results have direct and significant implications for the practical operation of TPOx reformers and highlight the necessity of a detailed kinetic approach for the accurate quantification of reformer performance addressing issues of syngas yield (related to the stack efficiency of the fuel cell), thermal efficiency (related to fuel conversion and energetic output and having direct implications for fuel interchange-ability) and molecular growth processes (related to the formation and deposition of unwanted carbonaceous species and pollutants across the system). The results can serve to provide design guidelines towards identification of optimum operating conditions for a particular application and fuel.

A closer inspection of the results presented in Figures 6-9, identifies two major regimes of desired operation. The first is defined by reformer operation at very short residence times, generally of the order of some milliseconds and intermediate temperatures. This is relevant to fuels that are characterized by a decoupling between syngas and molecular growth processes. On the other extreme, fuels involving a more convoluted coupling between the two processes will require reforming over long residence times and high temperatures. In the context of the present study, the first case relates to alcohols which exhibit an oxidative mode of fuel conversion featuring early syngas yield and a delayed molecular growth. The second regime is relevant to the reforming of methane mixtures, exhibiting a pyrolytic mode of fuel conversion. Although all the above remarks are generally valid, each fuel is a distinct case, and a detailed kinetic analysis would reveal features that may appear to be counterintuitive. This is the case with methanol, which shows an exceptionally high efficiency for very rich conditions, in contrast to all other fuels. This, in turn, is due to complete absence of molecular growth processes in methanol reforming, at least for the conditions of the present work. Another interesting feature is the enhanced efficiency of biogas mixtures, as compared to methane, due to the chemical effect of the CO_2 presence in the fuel mixture. Additionally, useful conclusions can be drawn regarding the choice of reforming stoichiometry. For most fuels and cases studied here, there appears to be an optimum stoichiometry, beyond which the penalty paid for increased pollutant formation is not compensated by significant gains in syngas yield.

2.2 Non-catalytic biogas pyrolysis

There are numerous studies on practical TPOx reformers and related SOFC systems operating with methane (or natural gas) mixtures available in the literature e.g. [207]. However, non-catalytic biogas thermal partial oxidation for SOFC applications has not yet been reported in the open literature. It is well known that hydrogen production is enhanced under fuel rich conditions and it is anticipated that it could be maximized under pyrolytic conditions. In the latter case, however, soot and non-gaseous carbonaceous products may be maximized as well. Naturally, pyrolysis studies can in principle provide great insight in the thermal partial oxidation reforming since it can be considered as the TPOx extreme regime.

In the present study, the pyrolysis of atmospheric pressure methane mixtures has been experimentally investigated in an isothermal plug flow reactor (PFR) in the temperature range of 1000-1200 ºC under well controlled conditions. The isothermal PFR has been extensively used in the past for the pyrolysis studies of hydrocarbon fuels, such as acetylene [208], ethanol [209] and acetylene/ethanol mixtures [210-211], where a detailed description of the experimental setup is provided. Different methane mixtures, representative of natural gas and biogas operation, were experimentally studied in pure nitrogen and mixed N_2/CO_2 atmospheres (see Table 3). Exhaust gases, including methane, hydrogen, carbon monoxide and key pollutants, from the PFR were monitored and quantitatively analysed online, using a gas chromatographic (GC) system. Total soot was determined by collecting and weighing soot samples from the reactor's exit as well as from deposits along the reactor for each case. In addition, Polycyclic Aromatic Hydrocarbons (PAH), also collected along the reactor and at the reactor exit, were measured using a coupled gas chromatographic and molecular spectrometric system (GC-MS), at selected temperatures. Further computations have been performed in order to numerically assess the effects of CO_2 loading on syngas production efficiency from methane pyrolysis.

Table 3. Initial species mole fractions for the experiments of Cases A-C.
Gas residence time t_{res}(s) = 4550/T(K) Experiments reported in [196].

Case	CH_4 (%)	C_2H_6 (%)	CO_2 (%)	N_2 (%)
A	10	-	-	90
B	10	-	33	57
C	9	1	-	90

The importance of studying a methane/CO_2 mixture lies in two reasons. First, such a mixture can be typically encountered in SOFC applications utilizing the outcome of a biomass gasification processes. Additionally, the effect of CO_2 addition to methane mixtures is of particular importance since it is related to the increasing interest of incorporating biogas mixtures in practical applications e.g. [217]. From a chemical kinetic point of view, an investigation on the role of CO_2 as a diluent (as compared to N_2) or as an oxidant can be realized, both in terms of syngas yield and reforming efficiency. Literature data relating to the effect of CO_2 dilution of methane mixtures on soot formation are generally scarce. On the other hand there are several experimental e.g. [220] and numerical e.g. [221] studies of the effect of CO_2 addition on soot formation in flames. The effect of CO_2 addition on combustion performance and soot formation has mainly studied in flames. Additionally, the results of such an investigation can also be utilized for evaluating the performance and optimization of emissions in e.g. devices incorporating exhaust gas recirculation (EGR) strategies [217-219].

First, results for fuel conversion and major products are presented in section 2.2.1. Experimental data for key intermediate species participating into the molecular growth processes, and eventually, soot formation, are presented in section 2.2.2. Finally, in section 2.2.3 the effect of CO_2 loading on syngas production efficiency from methane pyrolysis is parametrically investigated by numerical means.

2.2.1 Fuel conversion and syngas production

Figure 10a and 10b present fuel conversion and hydrogen production data at the reactor exit for the pyrolysis of pure methane (Case A, see Table 3) and of a methane/ethane mixture (Case C), respectively. Results for methane pyrolysis in the presence of CO_2, Case B, are shown in Fig. 11. Numerical simulations using the detailed kinetic mechanism decribed in reference [199] are also presented for all cases.

Generally, the results confirm the enhanced reactivity of the methane/ethane mixture as compared to pure methane, which is also in agreement with earlier studies e.g. [214-215]. For example, methane conversion in Case A is of the order of 25% at a temperature of 1323 K, while total initial carbon (CH_4 and C_2H_6) conversion reaches almost 50%, at the same temperature, in Case C. This is due to the fact that, at such temperatures, the relatively more unstable ethane molecule decomposes to the ethyl and hydrogen radicals, reaction R181. The hydrogen radical subsequently feeds into reaction R94 and accelerates methane conversion [214]. At higher temperatures, reaction R181 becomes significantly slower than the ethane thermal decomposition reaction R80 and, as a result, hydrogen radical production diminishes.

$$C_2H_6 (+M) = C_2H_5 + H (+M) \quad \text{(R181)}$$
$$CH_3 + CH_3 (+M) = C_2H_6 (+M) \quad \text{(R80)}$$
$$CH_3 + H (+M) = CH_4 (+M) \quad \text{(R93)}$$
$$CH_4 + H = CH_3 + H_2 \quad \text{(R94)}$$

On the other hand, the addition of carbon dioxide has no discernible effect on methane conversion at low temperatures. As the temperature is increased, hydrogen radicals produced from methane pyrolysis reaction R93 favour the CO_2+H = CO+OH reaction leading to enhanced OH radical formation rate. The latter initiates H radical abstraction reactions from methane, thus enhancing its conversion.

Despite the differences in the respective fuel consumption rates, hydrogen yield is of the same level in both Cases A and C, as shown in Figure 10. On the other hand, H_2 production is greatly diminished when CO_2 is added; for example, at a temperature of 1473 K, experimentally determined molar H_2 exhaust levels in Case B are less than 8%, less than half of the H_2 yield in Cases A and C (about 18%). However, total syngas (H_2 and CO) yield is retained in terms of volume fraction but not in terms of energy content, due to the lower heat of formation of CO. This can have a direct effect on the reforming efficiency, as it will be further analyzed below.

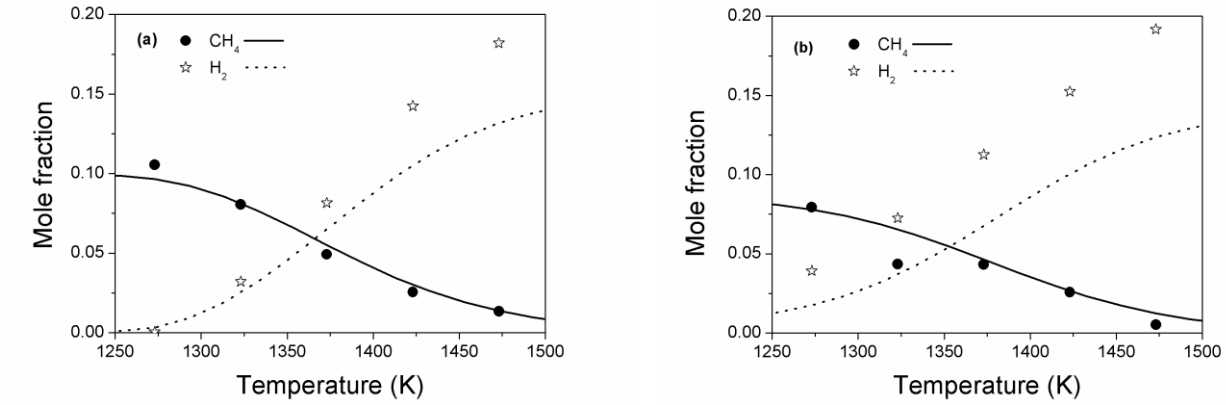

Figure 10. Comparison between experimental data and numerical simulations for methane conversion and hydrogen yield in (a) pure methane pyrolysis (Case A) and (b) methane/ethane pyrolysis (Case C).

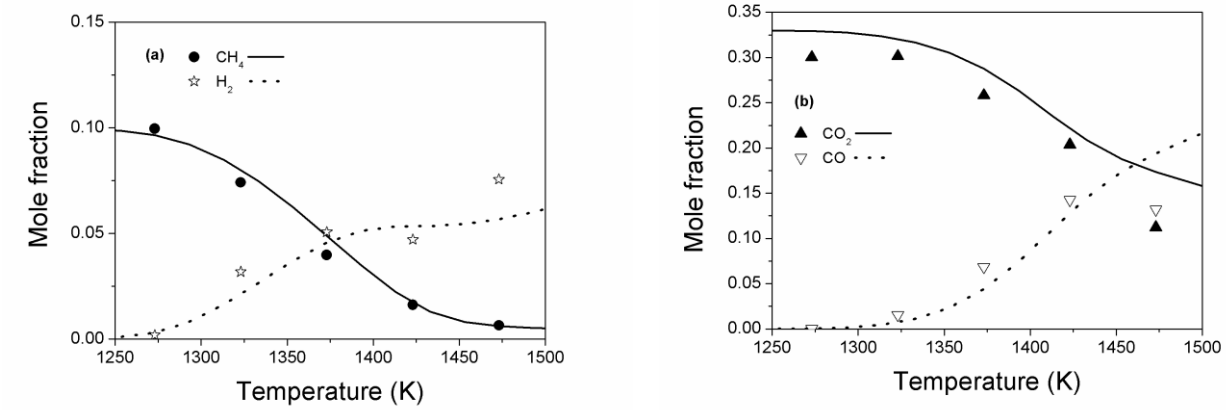

Figure 11. Comparison between experimental data and numerical simulation for (a) methane conversion and hydrogen yield and (b) CO and CO_2 exhaust levels in methane pyrolysis in the presence of CO_2 (Case B).

Overall, numerical predictions for major species lie within reasonable agreement with the experimental data for all cases. The mechanism is shown to be able to reproduce methane conversion and H_2/CO production trends along the temperature range studied, with hydrogen levels being a notable exception, particularly under high temperatures (T > 1400 K), mainly in Cases A and C. The reason for this discrepancy is discussed below.

Rate-of-production analysis has been performed in order to investigate the chemical processes occurring during methane and the methane/ethane mixture pyrolysis. Computations for all path analyses have been performed at the location of 50% fuel consumption inside the reactor. In all cases studied, the overall reaction starts with methane thermal decomposition to produce methyl and hydrogen radicals, through the unimolecular reaction R93. Subsequent H radical attack on methane (reaction R94), provides the system with more CH_3.

$$CH_3 + H\ (+M) = CH_4\ (+M) \quad \text{(R93)}$$

$$CH_4 + H = CH_3 + H_2 \quad \text{(R94)}$$

This is essentially a chain initiating sequence leading to the net generation of a methyl radical for each methane molecule consumed. The above sequence also contributes almost 50% of the total molecular hydrogen in Case A. Methyl radical is then exclusively consumed to C_2H_6, via the self-

recombination reaction R80, initiating the C_2 chain. Hydrogen radicals act as chain carriers to a sequence of H abstraction reactions leading from ethane down to acetylene and shedding H_2 molecules along the way.

$$CH_3 + CH_3 (+M) = C_2H_6 (+M) \quad \text{(R80)}$$
$$C_2H_6 + H = C_2H_5 + H_2 \quad \text{(R184)}$$
$$C_2H_5 (+M) = C_2H_4 + H (+M) \quad \text{(R182)}$$
$$C_2H_4 + H = C_2H_3 + H_2 \quad \text{(R163)}$$
$$C_2H_3 (+M) = C_2H_2 + H (+M) \quad \text{(R153)}$$

It is interesting to note that the above sequence is not a radical chain sequence since H radicals formed by reactions R182 and R153 are consumed at equal rates by reactions R184 and R163.
The above described paths (reactions R94, R184, R163) account for the H_2 production. However, the mechanism tends to under-predict hydrogen mole fractions at higher temperatures (T > 1350 K) and in particular in Cases A and C, with discrepancies of the order of 30%. Such discrepancies cannot easily be attributed to deficiencies of the two major H_2 production paths described above (reactions R184, R163). The reason is that methane consumption profile and total C_2 levels, particularly in higher temperatures, are adequately captured. This implies that, there may be additional hydrogen production paths, such as thermal cracking reactions, possibly involving higher aliphatic, e.g. C_4, or (poly-) aromatic species. However, analysis of trial computations including some molecular elimination reactions, such as reaction R.I[4], reveals that there is not any appreciable contribution to H_2 formation due to R.I. Also note that molecular hydrogen is "numerically" locked in higher PAH species, since the current version of the NTUA.HMCS mechanism does not include any soot reactions.

$$C_2H_4 + M = C_2H_2 + H_2 + M \quad \text{(R.I)}$$

On the other hand, hydrogen levels are satisfactorily reproduced in Case B. This is due to the CO_2 presence which induces an oxidative character into the pyrolytic process, resulting into a more balanced chemistry. For instance, and at a the case of 1473 K, in addition to reaction R94 and the C_2 chain paths discussed above, there is a substantial contribution to H_2 formation from reactions involving oxygenated species, such as formaldehyde, ketene and propionaldehyde.
As far as Case B is concerned, the picture is not totally different from the one described above. However, the H radical also initially produced by the thermal decomposition of methane, reaction R93, promptly attacks CO_2 molecules producing CO and a hydroxyl radical, reaction R23. Thus, in the presence of CO_2 abstraction reactions with OH constitute a considerable fraction of the total fuel abstraction reactions and lead to water formation, competing thus to H_2 production. As a result, hydrogen yield in Case B is almost half as compared to Cases A and C, The above discussion suggests that CO_2 act as an oxidizer and not as a mere diluent, like N_2. The issue is further numerically explored in section 2.2.3.

$$CO + OH = CO_2 + H \quad \text{(R23)}$$

In the experimental data set of [196], the production of a significant amount of water was found, which is in agreement with the findings of Abián et al. [216]. Figure 12 presents estimated water

[4] Reaction R.I rate constant: $k_{f,R.I.} = 3.5 \times 10^{16} \times \exp(-35984/T)$ with enhanced collision coefficients: N_2:1.5 and H_2O:10.

levels at the reactor exit. These estimated values were obtained through balancing the H atom content in the inlet mixture, with the total H atom content in the gaseous (C_1-C_7) species quantified at the reactors exit. The difference is roughly proportional to the water levels, since contributions from hydrogen contained in PAH species can be assumed to be minor. Estimated water values presented in Figure 12 are thus an upper threshold and carry an uncertainty level of 25%. Computations are also presented in Figure 12. The mechanism qualitatively captures the trend in water formation, with also satisfactory agreement in peak values. A closer examination of the numerical and estimated H_2O results, reveals that there are essentially two distinct regions; a sharp increase in exhaust water levels followed by a plateau. The transition point occurs at around

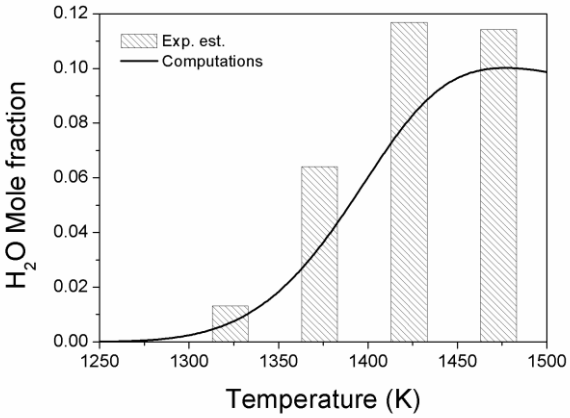

Figure 12. Comparison between estimated water levels against numerical predictions at the reactor.

1450 K. In order to explain such a behavior, rate-of-production analyses have been performed at 1325 K and 1475 K, the former being chosen as the starting point of the sharp increase while the latter is located well within the plateau. Under lower temperatures, water is still being formed by OH radical attack to the fuel, reaction R96, with a minor (up to 20%) contribution from reaction R3. At higher temperatures, water achieves steady state behavior; it is now formed through reaction R3 and destroyed mainly via addition reactions with C_2 (mainly acetylene) and C_3 (mainly propargyl radical) hydrocarbons leading to the formation of C_2 and C_3 oxygenated species.

$$CH_4 + OH = CH_3 + H_2O \quad \text{(R96)}$$

$$OH + H_2 = H_2O + H \quad \text{(R3)}$$

Changes in water behavior are directly related to a more subtle alteration in the overall system behavior, from a purely kinetically controlled to a partially equilibrated regime. This is clearly illustrated in Figure 13, which presents the values of the reaction species quotient of the water-gas-shift reaction calculated by using computational species profiles and compared with the equilibrium constant proposed by Moe [222], as commonly used [216, 223]. Clearly, above 1450 K, the water-gas-shift reaction quotient, although close, is markedly distinct from the thermodynamic equilibrium.

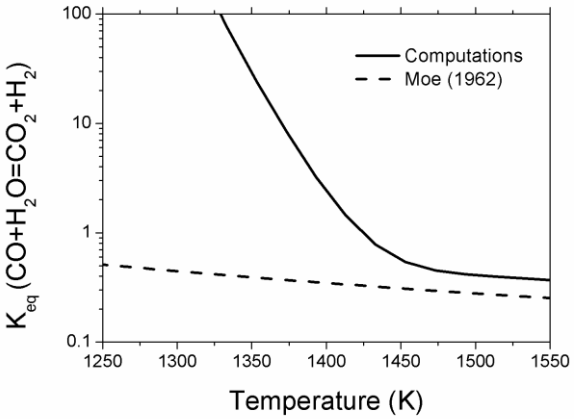

Figure 13. Reaction quotient and equilibrium constant for the water-gas-shift reaction.

2.2.2 Molecular growth processes and soot precursors chemistry

Soot formation tendency is closely linked to the chemistry of several key soot precursors. Acetylene and benzene, in particular, are closely linked both to PAH formation and soot mass growth processes. Acetylene is an indicative species for soot mass growth process while benzene largely determines soot nucleation. Accordingly, a quantification of the acetylene and benzene formation dynamics is expected to provide valuable information on carbonaceous formation and deposition processes.

Experimental and predicted data for C_2H_6, C_2H_4, C_2H_2, C_3H_6 and a-C_3H_4 (allene) are shown in Figures 14-18, respectively. The initiation of the C_2 chain, starting from C_2H_6 formation and finally leading to acetylene formation, has been described above (sequence of reactions R184-R182-R163-R153), and found to be directly linked to the fuel consumption chemistry. Overall, the agreement is satisfactory, although there is room for improvement.

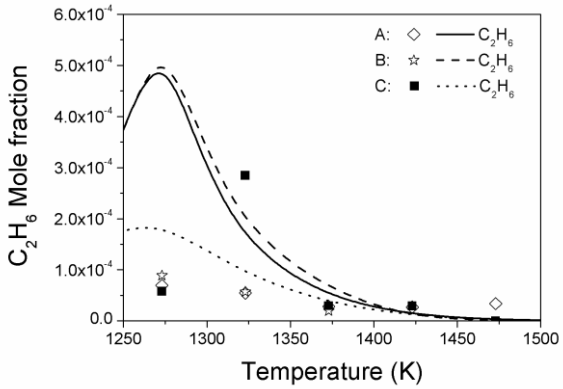

Figure 14. Comparison between experimental data (symbols) and numerical simulation (lines) for C_2H_6 exhaust levels in (a) Case A, (b) Case B and (c) Case C.

The mechanism over-estimates C_2H_6 levels under lower temperatures, for Cases A and B, by a factor of 5 (Figure 14). Since C_2H_6 comes exclusively from methyl radical recombination, and the latter in the low temperature regime is determined by the rate of reaction R93, it is reasonable to argue that the rate constant of the latter reaction is inappropriate. Reaction R93 is pressure dependent, with a temperature independent high pressure limit, and an enhanced collision efficiency for ethane of 5 for the low pressure limit [224]. Thus, the above reaction is catalyzed

under the studied conditions by the high C_2H_6 levels in the system, resulting in such an over-prediction. This further indicates that the rate is not appropriate for such pyrolytic conditions. At higher temperatures reaction -R93 becomes irrelevant for CH_3 production, since abstraction reaction R94 dominates, and the level of agreement between experimental and predicted data improves. Finally, for Case B, the sudden drop in C_2H_6 profiles for temperatures above 1373 K, is corroborated by the lack of detection in the same range implying that ethane levels are below TCD (Thermal Conductivity Detector) detection limit under the present conditions. Further downstream the C_2 chain, ethylene levels are in general satisfactorily described, Figure 15.

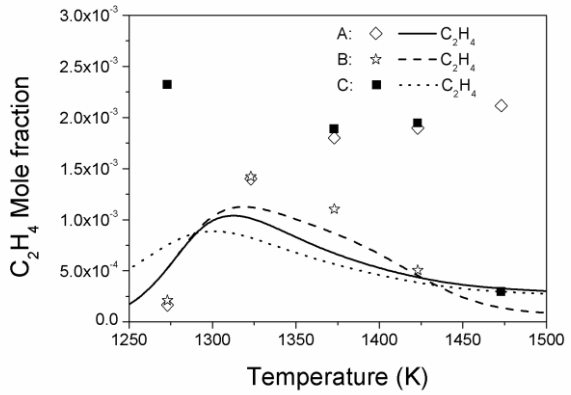

Figure 15. Comparison between experimental data (symbols) and numerical simulation (lines) for C_2H_4 exhaust levels in (a) Case A, (b) Case B and (c) Case C.

Acetylene levels are generally well reproduced, see Figure 16. Peak acetylene levels for all three cases, and within the studied temperature range, are similar, with values of around 2000 ppm. The acetylene formed, is quantitatively consumed to C_3H_4 species which, in turn, initiate further molecular growth reactions. In particular, the C_3 chain is initiated by CH_3 radical addition to acetylene, reactions R321 and -R322, leading to allene and propyne respectively.

$$C_2H_2 + CH_3 = a\text{-}C_3H_4 + H \quad \text{(R321)}$$
$$C_2H_2 + CH_3 = p\text{-}C_3H_4 + H \quad \text{(-R322)}$$

C_3H_4 species are exclusively consumed to the propargyl radical, which, in turn, recombines to form benzene. Propene (Figure 17) is also formed by CH_3 addition to C_2H_4 either directly, reaction -R382, or indirectly, through the n-propyl radical, reaction R401, and subsequently goes down the C_3 chain, as described above.

$$C_3H_6 + H = C_2H_4 + CH_3 \quad \text{(R382)}$$
$$n\text{-}C_3H_7 = C_2H_4 + CH_3 \quad \text{(R401)}$$

Further upstream in the C_3 chain, C_3H_6 levels are over-predicted by a factor of two, see Figure 17. Since propene formation is solely due to the methyl vinyl radical recombination, the above over-prediction can be attributed to the overall CH_3 over-prediction, as discussed earlier. Exhaust benzene levels as a function of temperature are shown in Figure 19. Experimental data appear to be insensitive to temperature, while numerical results show distinct peaks at intermediate temperatures. Generally, the simulated pyrolysis of the methane/ethane mixture (Case C) appears to result in significantly higher benzene levels, particularly at lower temperatures and as compared to the pure methane pyrolysis case (Case A). Since numerical results are generally higher than experimental data, the discrepancies found are attributed to the fact that the formation of soot is

not included in the models and this suggests the need for further improvement in the current models [211] in order to reproduce the complex behavior of soot formation.

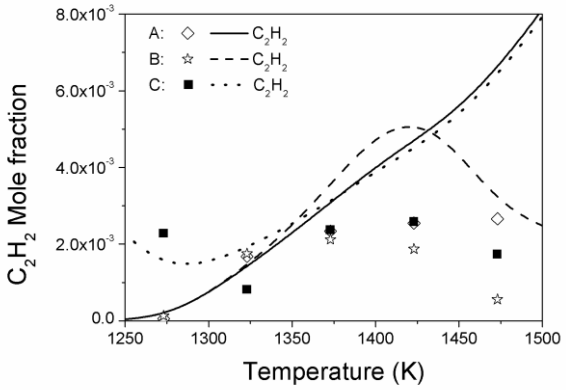

Figure 16. Comparison between experimental data (symbols) and numerical simulation (lines) for C_2H_2 exhaust levels in (a) Case A, (b) Case B and (c) Case C.

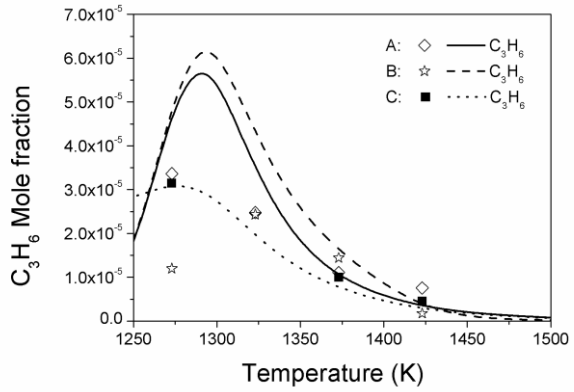

Figure 17. Comparison between experimental data (symbols) and numerical simulation (lines) for C_3H_6 exhaust levels in (a) Case A, (b) Case B and (c) Case C.

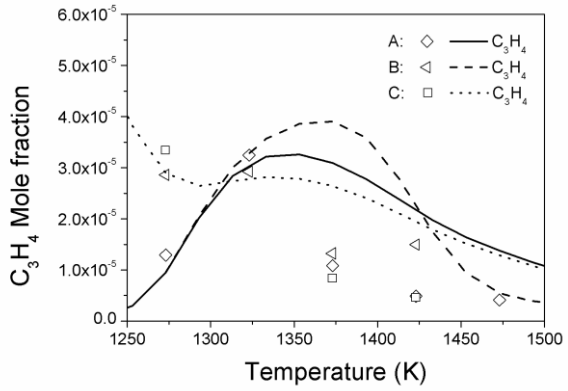

Figure 18. Comparison between experimental data (symbols) and numerical simulation (lines) for a-C_3H_4 (allene) exhaust levels in (a) Case A, (b) Case B and (c) Case C.

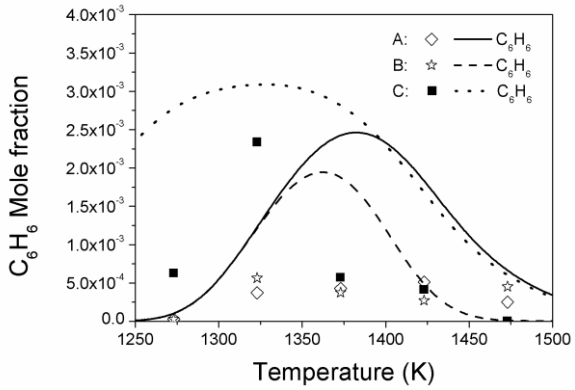

Figure 19. Comparison between experimental data (symbols) and numerical simulation (lines) for C_6H_6 exhaust levels in (a) Case A, (b) Case B and (c) Case C.

2.2.3 CO_2 content on syngas produciton - numerical parametric study

In order to further investigate the effect of CO_2 in syngas yield as well as the role of CO_2 as a diluent or oxidizer a parametric study was conducted. The computations were performed for 10% methane and 90% diluent, corresponding to the previously described conditions, as far as PFR geometry and flow rate are concerned. The first case corresponds to pure nitrogen diluent (Case A) and the last to pure CO_2 diluent, resembling dry reforming for SOFC applications. Naturally, the intermediate cases correspond to varying N_2/CO_2 ratios, including Case B which was also experimentally described earlier in the present work. The studied mixtures are listed in Table 4.

Table 4. Initial species mole fractions for the CO_2 dilution parametric study.

Mixture	CH_4 (%)	N_2 (%)	CO_2 (%)	Comments
I	10	90	-	Case A
II	10	80	10	
III	10	57	33	Case B
IV	10	30	60	
V	10	-	90	

Figure 20a demonstrates the effect of the CO_2 content in the mixture on the syngas yield. It can be seen that the presence of 10% CO_2 does not significantly affect syngas yield whereas, hydrogen production is significantly depressed with increasing CO_2 content in the mixture, in agreement with the experimental data. Naturally, when the CO_2 becomes the dominant diluent in the mixture, CO increases dramatically. In addition, Figure 20b presents the difference in mixture reactivity through monitoring the fuel consumption. It is clear that the CO_2 presence acts in favor of faster fuel conversion in lower temperatures (1050-1100 ºC), whereas the fuel is totally consumed when higher temperatures (1200 ºC) are reached, in all cases. Nevertheless, it can be anticipated that even with higher amounts of CO_2 in the initial mixture, the syngas yield in higher temperatures is satisfactory and resemble SOFC operating conditions with biogas. For assessing the effect of the mixture conversion upon the final energy content the reforming efficiency was computed according to expression (1). The results of the later computations are presented in Figure 21. It is clear that since the diluent contributes on the energy content of the final products, the total yield reaches unrealistic values and this remains an issue for adopting a more appropriate formula. However, the

results suggest that a small addition (e.g. 10%) of CO_2 diluent affects dramatically the syngas energy content, whereas higher amounts of CO_2 diluent do not come with the same impact.

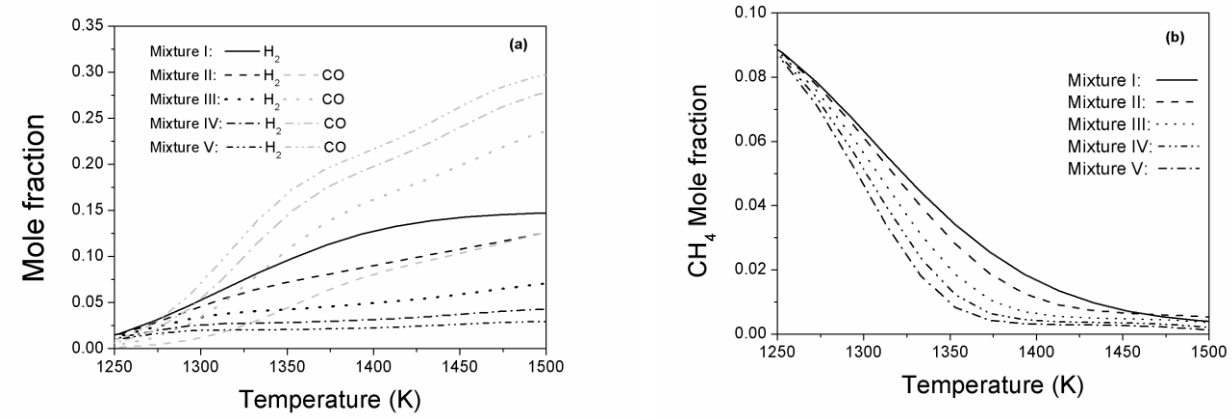

Figure 20. Exhaust syngas yield (a) and fuel consumption (b) as a function of CO_2 dilution and reactor temperature.

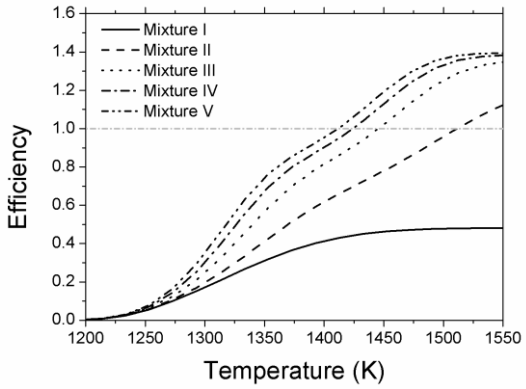

Figure 21. Overall syngas efficiency for parametric computations I-V.

2.3 Summary of biogas non-catalytic reforming strategies

Non-catalytic reforming strategies of biogas such as TPOx reforming appear to be advantageous due to their fuel flexibility, absence of catalyst deactivation issues and the low fuel cleaning requirements. However thermal POx reforming requires higher operation temperatures than catalytic POx reforming which imply a higher energy cost. Moreover, as stated before, the high temperature values along the manifolds can lead to kinetically controlled undesirable effects decreasing the overall system efficiency.

3. Catalytic reforming strategies of biogas

This section reviews four catalytic reforming strategies commonly applied for hydrocarbon fuels: dry reforming, steam reforming, partial oxidation and autothermal reforming. Since catalytic partial oxidation is the strategy that is employed for fuel reforming in the FC-District micro-CHP unit more emphasis will be given to this technology. Thus, Section 3.1 is dedicated exclusively to catalytic partial oxidation while the three remaining strategies are presented in section 3.2. The review for each strategy starts by providing an in-depth insight for methane as the fuel and further extended to biogas in an extensive literature review.

3.1 Catalytic partial oxidation

3.1.1 Methane catalytic partial oxidation

The first papers dealing with catalytic partial oxidation (CPOx) of methane are dated of late 1920's to 1940's [64-66]. However, at the time the methane reforming with sub stoichiometric amounts of oxygen in the presence of a catalyst revealed some disappointing features such as the strong tendency to coke deposition on Ni catalysts, which was not studied in detail, and the huge inlet feed temperature required to achieve high syngas selectivity. This poor knowledge combined with the success of steam reforming was responsible for the decaying attention for decades on this process [67]. Catalytic partial oxidation has received an increasing attention from the beginning of the 1990's after Schmidt and co-workers reported excellent fuel conversion and synthesis gas selectivity under autothermal and short contact time conditions using Rh and Pt noble metals over monoliths [68-69].

This process has several advantages over other well established technologies to produce synthesis gas like high energy demanding steam reforming technology. Globally, the catalytic partial oxidation of methane is mildly exothermic ($\Delta H_R^\circ = -36\ \mathrm{kJ/mol}$), it has H_2/CO ratio of 2 and it is described by reaction R1.

R1 $$CH_4 + \frac{1}{2}O_2 \rightarrow CO + 2H_2 \qquad \Delta H_R^\circ = -36\ \mathrm{kJ/mol}$$

The H_2/CO ratio achieved through methane CPOx reaction is acceptable for downstream applications, such as the methanol synthesis and the Fischer-Tropsch synthesis of liquid fuels [67,70]. Due to its global exothermicity this reaction can be performed in an autothermal regime (adiabatic conditions) and then this technology is more economical than steam reforming requiring much simpler and compact equipment, with a low thermal inertia allowing a fast dynamic response to transients [71]. As the reaction proceeds at low residence times (0.1-10 ms) high throughputs are expected with CPOx technology [68]. For these reasons CPOx reforming is a suitable candidate for mobile or stationary decentralized applications.

Since natural gas has a high dissemination in the industrialized countries, catalytic partial oxidation offers a promising route to produce H_2 rich mixtures for domestic appliances, namely fuel cells for electrical generation purposes at residential level. A direct combination between a CPOx reactor and a fuel cell stack without intermediate H_2-enrichment and CO mitigation reactions can be implemented being in this case the SOFC the most appropriate fuel cell type due to its relative insensitivity to CO in the inlet feed mixture. Heat generation from thermal recovery of fuel cell

anode off-gas is also an opportunity to increase even more the overall efficiency of the primary energy utilization into final energy. Indeed, combined decentralized production of heat and power can reduce the energy distribution losses [83].

3.1.1.1 Catalysts

There are three main catalyst groups that have been proposed as active for methane CPOx namely supported first-row transition metal catalysts (Ni, Co and Fe), supported noble metal catalysts (Ru, Rh, Pd, Pt and Ir) and transition metal carbide catalysts [67]. The last catalyst group has received less attention in the literature which may reflect their lower performance for methane CPOx. In the following a brief literature survey on the topic of supported Ni, Co and Fe catalysts (a) and supported noble metal catalysts (b) is presented.

(a) Supported Ni, Co or Fe catalysts

It is generally acknowledged the following order of catalyst activity towards methane CPOx: Ni >> Co > Fe [67]. Co and Fe have much lower performance for CPOx of methane compared with Ni because CoO and Fe2O3 have higher activity for total oxidation of methane.
Lunsford studied supported Ni catalysts for CPOX of methane in the temperature range 450-900 ºC. At about 700 ºC complete methane conversion with about 95% of selectivity to CO and H_2 could be achieved. They also found that three regions exist in the catalyst bed with different states of the catalyst, $NiAl_2O_4$, NiO/Al_2O_3 and supported nickel metal particles [121].
Ni- and Co-based catalysts have been widely explored but their propensity for coking and metal loss at high temperatures and flow rates has been revealed a major disadvantage [67,111]. To decrease the tendency for carbon lay down during methane CPOx it was proposed the addition of a second or third metal (mostly precious metals) [112-114], addition of rare earth metal oxides [115] and addition of basic metal oxides [114-115]. The beneficial effect of adding earth metal or alkaline metal oxides is attributed to the capability for oxygen storage of these metal oxides, which help by oxidizing the surface carbon deposited [122]. The catalyst preparation method [116] and the supports applied have also an important role on the catalyst stability since it is broadly recognized that high active phase dispersion with small metal ensembles contribute to a lower carbon deposition [20,118].

(b) Supported noble metal catalysts

On the other hand noble metal catalysts exhibit a lower propensity for carbon deposition. Claridge et al. [117] found the relative order for carbon deposition:

Ni > Pd >> Rh, Ru, Ir, Pt (1 atm; 1050 K; CH_4/CO_2=2; 8 mL/min; 24 h)

Besides the low susceptibility to deactivate by fouling, noble metal catalysts are highly active for the methane CPOx reaction. Recently, based on methane conversion values Nematollahi et al. [119] showed the following relative order of catalyst activity for methane CPOx:

Rh, Ru > Ir > Pt > Pd (1 atm, 500-700 ºC, CH_4/CO_2=2, GHSV=160000 mL/(h g_{cat}))

In fact, noble metal catalysts have attracted great attention and have been widely studied in the last three decades. Schmidt [69, 123-124] and Poirier [125] studied CPOx of methane over Rh

catalysts and Pt-Pd catalysts at extremely high flow rates, respectively. It was reported that these noble metal catalysts, even with very low metal loadings, were much more active than Ni catalysts. It was shown by Green [82,126] that high yields of synthesis gas can be obtained over nearly all noble metals. Preparation method and support properties also influence the catalytic performance of noble metal catalysts. The effect of the support on the performance of Rh based catalysts in the partial oxidation of methane to synthesis gas was investigated by Ruckenstein [127]. It was concluded that in general noble metal catalysts supported on reducible oxides (e.g., CeO_2, Nb_2O_5, Ta_2O_5, TiO_2 and ZrO_2) are much less active and selective to CO and H_2 than noble metal catalysts supported on irreducible oxides (e.g., γ-Al_2O_3, La_2O_3, MgO, SiO_2 and Y_2O_3). Among the irreducible oxide supports, γ-Al_2O_3, La_2O_3 and MgO supported Rh_2O_3 catalysts provided stable catalytic performance [139-140]. This high stability was attributed to formation of $MgRh_2O_4$ due to the strong interaction between Rh and MgO. Guerrero-Ruiz [128] studied CPOx of methane and CO_2 reforming of methane over Ru/Al_2O_3 and Ru/SiO_2 using isotopic tracing technique. It was reported that the support was also involved in reactions, somewhat modifying the catalytic behaviour. To realize CPOx of methane over noble metal catalysts at extremely short contact time (in the order of milliseconds), monolith-supported noble metal catalysts have been also studied [129]. At a contact time of 10-3 second, more than 90% of methane and complete oxygen (CH_4/O_2=2:1) can be converted over Rh-coated ceramic monoliths to synthesis gas with a selectivity of 90%.

3.1.1.2 Reaction mechanisms for methane CPOx over metal catalysts

Two different mechanisms have been proposed for CPOx of methane over metallic catalysts. One is socalled “two-step reaction mechanism”, which is mainly proposed for CPOx of methane over non noble metal catalysts, e.g. Ni, Co and CPOx of methane over noble catalysts (Pt and Rh) at relatively low temperatures (<800 °C). The other is “direct partial oxidation mechanism”, which is mainly proposed for CPOx of methane over noble catalysts e.g. Pt and Rh, especially at very high temperatures (>1000°C) and with an extremely short contact time (in the order of milliseconds).

(a) Two-step reaction mechanism

Ashcroft and co-workers [18,82,141-143] reported that synthesis gas can only be produced when part of the metal oxide catalyst is reduced to metal, although methane can be oxidized over metal oxides. They also studied the effect of contact time, and found that with a decrease in contact time the conversion and selectivity decrease. Therefore, they suggested that the reaction pathway may involve initial deep oxidation of some CH_4 to CO_2 and H_2O, followed by a sequence of steam - and CO_2 - reforming of unconverted CH_4 to synthesis gas and reverse water-gas shift reactions to give equilibrium product yields. By carefully measuring the temperature gradients in Ni-based catalyst bed, Vermeiren [130] observed pronounced exothermic reactions near the inlet of the catalyst bed and endothermic reactions in the latter half of the bed. Their results further confirmed that CPOx of methane proceeds via a sequential reaction mechanism.

(b) Direct partial oxidation mechanism

In contrast to previous proposal of the generation of synthesis gas via a sequence of total oxidation followed by reforming, Schmidt [123] demonstrated that both H_2 and CO are primary products of the direct oxidation of methane at high temperatures and an extremely short contact time (in the order of milliseconds). The direct partial oxidation mechanism is illustrated in Figure 22. It was

suggested that the mechanism involved direct formation of H_2 initiated by CH_4 pyrolysis on the surface of noble catalysts to give surface C and H species.
The H adatoms dimerize and desorb as H_2, while the surface C atoms react with adsorbed O atoms and desorb as CO.

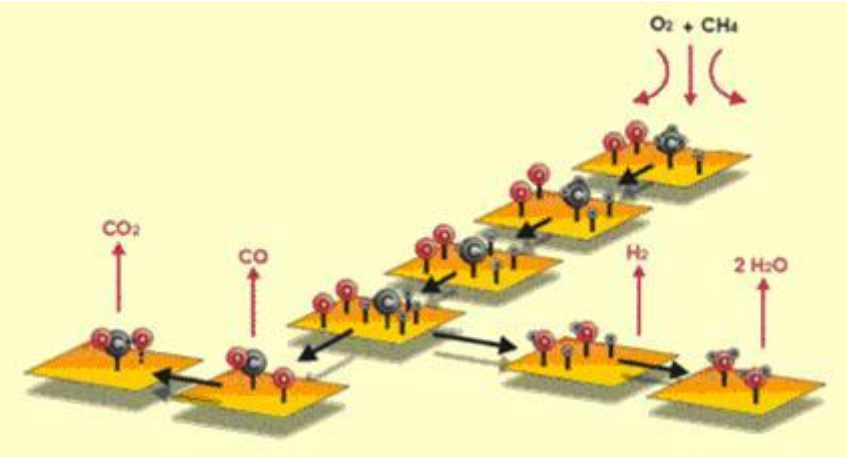

Figure 22. Schematic mechanism of direct partial oxidation of methane to synthesis gas [138].

They also modeled CH_4 oxidation in a plug flow reactor using the CH_4 pyrolysis mechanism [124]. Their model agreed well with the experiments, confirming that direct oxidation was the mechanism for oxidation over Rh coated monolith catalyst. However, it still cannot be completely excluded that both deep oxidation and consecutive reforming reactions occur, because both reaction zones could be too close to be distinguishable under the extreme conditions (very high temperatures and very short contact time).

3.1.1.3 Problems with metal catalysts

CPOx of methane is normally carried out at high reaction temperatures to reach high methane conversion and high selectivity to CO and H_2. Moreover, according to the “two-step reaction mechanism” [82], CPOx of methane over metal catalysts proceeds via deep oxidation followed by steam and CO_2 reforming as consecutive reactions. High exothermicity of the deep oxidation results in temperatures in the catalyst bed amounting to more than 1000 ºC at the top of the catalyst bed. In the second part of the reactor bed the endothermic reforming reactions lead to lower temperatures. Over noble metal catalysts, e.g. Rh, synthesis gas seems to be produced by directly partial oxidation of CH_4 at very high temperature (>1000 ºC) and with a very short contact time [123]. However, the catalyst still suffers from extremely high temperatures, although this provides an elegant solution to the temperature gradients over the reactor. The volatility of support materials or that of the active catalytic components is usually not considered as a problem. However, in the case of catalytic oxidation at these high temperatures volatilization of the active phase must be considered as an important factor for deactivation of the catalyst. Significant loss of Pt via formation of volatile oxides is observed at 1000 ºC in the presence of oxygen. Hermans [131] studied platinum volatilization from supported Pt catalysts at temperatures above 600 ºC. It was found that PtO_2 is the most dominant volatile species and high dispersion of Pt on the support results in even higher volatilization of PtO_2 than expected from thermodynamic equilibrium. Metal loss in the form of volatile oxide, which contributes to deactivation of the catalyst, is also a serious

problem in the ammonia oxidation process over Pt-Rh gauzes operated at similar conditions as CPOx of methane [132].

Sintering of catalyst particles and phase changes of the support structure are also an issue that concerns the applicability of metal catalysts supported on a highly porous structure at very high operating temperatures. These thermal driven deactivation mechanisms lead to a reduction of the active surface area and a decrease in the catalyst activity is expected.

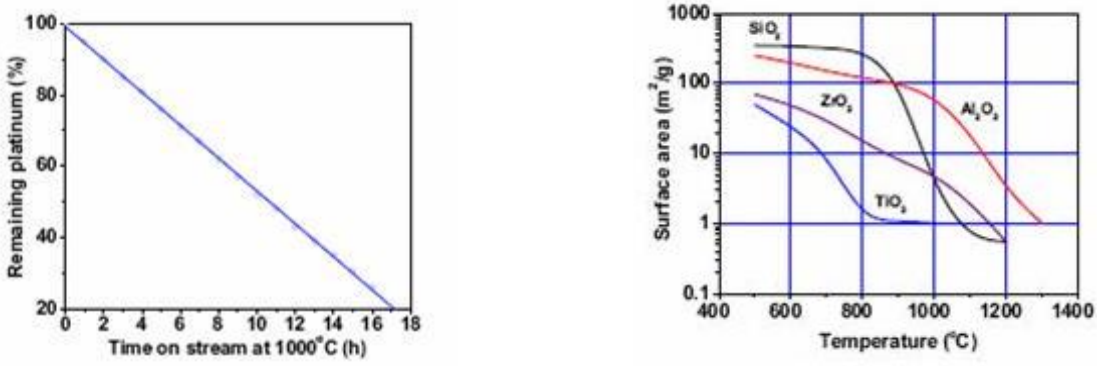

(a) (b)

Figure 23. Loss of Pt from 1% Pt monolith catalyst at 1000 ºC in moist air (a) and loss of surface area of oxide support due to sintering (b).

Figure 23 shows that surface areas of oxide supports decrease significantly with increasing operation temperature. Vaccari [133] studied deactivation of a Pt/γ-Al_2O_3 catalyst used for CPOx of methane causing at 900 ºC. Significant sintering of both Pt and γ-Al_2O_3 was observed, which results in deactivation of the catalyst.

3.1.1.4 CPOx of methane over oxide catalysts

Compared to metal catalysts, oxide catalysts have almost not been studied for CPOx of methane. However, CPOx of methane has been often mentioned as a major side reaction in both oxidative coupling of methane over rare oxides [134] and partial oxidation of methane to formaldehyde on TiO_2 [135]. CPOx of methane over some irreducible or hardly reducible metal oxides such as TiO_2, La_2O_3, and ZrO_2-based mixed oxides was studied by Steghuis [136-137] and Stobbe [138]. Yttrium stabilized zirconia (YSZ) showed the best catalytic performance among these oxide catalysts. Stobbe concluded, based on the relation between methane conversion and selectivities over ZrO_2, that CO and H_2 are primary products of CPOx of methane over ZrO_2, whereas CO_2 is formed by water-gas shift and oxidation of CO. Steghuis proposed a reaction mechanism of CPOx of methane over YSZ, including homolitic dissociation of methane over O-(S) sites followed by conversion to CO, H_2 and H_2O via the formation and decomposition of formaldehyde as an intermediate. CO_2 is produced by further oxidation of the reaction intermediate. As reported by Steghuis [136], YSZ catalyzes direct partial oxidation of methane to synthesis gas with a reasonable activity and selectivity, although they are still as compared with metal catalysts. Moreover, YSZ is much more thermally stable as compared with metals under CPOx of methane conditions (in the presence of oxygen at high temperature). These features make YSZ a very interesting catalyst for CPOx of methane. However, the details of catalysis of YSZ during CPOx of methane are not fully understood yet. The defective structure of YSZ seems to play an important role in CPOx of methane.

Comprehensive reviews on the topic of methane catalytic partial oxidation can be found in references [5,67,71,110-111].

3.1.2 Biogas catalytic partial oxidation

Biogas catalytic partial oxidation corresponds to the combination of dry reforming and catalytic partial oxidation of methane (also known as oxidative dry reforming, oxy-CO_2 reforming or dry autothermal reforming of methane) with a CH_4/CO_2 ratio typical of the biogas composition. The addition of O_2 to an inlet biogas feed stream has several advantages namely the suppression of carbon formation, the reduction or complete elimination of external heat requirements and the enhanced methane conversion to H_2 and CO [25, 73]. Moreover by controlling the amount of O_2 co-fed with biogas the H_2/CO ratio can be tuned [79].
During biogas catalytic partial oxidation the set of reactions presented below (R2-R11) as well as reaction R1 can describe the global mechanism between reactants and products.

R2	$\mathrm{CH_4 + CO_2 \rightleftharpoons 2CO + 2H_2}$	$\Delta \mathrm{H_R^\circ} = +247\ \mathrm{kJ/mol}$
R3	$\mathrm{CH_4 \rightleftharpoons C(S) + 2H_2}$	$\Delta \mathrm{H_R^\circ} = +75\ \mathrm{kJ/mol}$
R4	$\mathrm{2CO \rightleftharpoons C(S) + CO_2}$	$\Delta \mathrm{H_R^\circ} = -172\ \mathrm{kJ/mol}$
R5	$\mathrm{CH_4 + H_2O \rightleftharpoons CO + 3H_2}$	$\Delta \mathrm{H_R^\circ} = +206\ \mathrm{kJ/mol}$
R6	$\mathrm{CH_4 + 2H_2O \rightleftharpoons CO_2 + 4H_2}$	$\Delta \mathrm{H_R^\circ} = +165\ \mathrm{kJ/mol}$
R7	$\mathrm{CO + H_2O \rightleftharpoons CO_2 + H_2}$	$\Delta \mathrm{H_R^\circ} = -42\ \mathrm{kJ/mol}$
R8	$\mathrm{CO + H_2 \rightleftharpoons C(S) + H_2O}$	$\Delta \mathrm{H_R^\circ} = -131\ \mathrm{kJ/mol}$
R9	$\mathrm{CH_4 + 2O_2 \rightarrow CO_2 + 2H_2O}$	$\Delta \mathrm{H_R^\circ} = -803\ \mathrm{kJ/mol}$
R10	$\mathrm{H_2 + \frac{1}{2}O_2 \rightarrow H_2O}$	$\Delta \mathrm{H_R^\circ} = -242\ \mathrm{kJ/mol}$
R11	$\mathrm{CO + \frac{1}{2}O_2 \rightarrow CO_2}$	$\Delta \mathrm{H_R^\circ} = -283\ \mathrm{kJ/mol}$

Thermodynamic equilibrium calculations give usually a starting point about ideal operating windows for further experimental/numerical pursuing. The method of minimisation of Gibbs free energy was herein employed in spite of the use equilibrium constants due to its well-recognised difficulty in the prediction of equilibrium states where condensed species exits simultaneously with gaseous species [11,12]. CH_4, CO_2, O_2, H_2O, CO, H_2 and C(S) were considered for equilibrium calculations. C(S) corresponds to solid carbon (graphite). In all thermodynamic equilibrium calculations herein reported the total reactor pressure was considered constant (isobaric conditions) and equal to the atmospheric pressure along with temperature (isothermal conditions) or enthalpy (adiabatic conditions) forming two different sets of thermodynamic constrains. Thermodynamic equilibrium calculations were performed with the CANTERA software [13].
The performance of the catalytic partial oxidation of biogas co-fed with air under the thermodynamic equilibrium conditions is carried out analysing the mixture composition (in a molar basis) and reactants (CH_4, CO_2 and O_2) conversion and H_2, CO and C(S) selectivities. The conversion of a reactant species k is given by expression (2) and the H_2, CO and C(S) selectivities are computed through expressions (3), (4) and (5) respectively. $\dot{n}_k$ is the molar flux of species k.

$$\mathrm{X}_k = \frac{(\dot{n}_k)_{in} - (\dot{n}_k)_{out}}{(\dot{n}_k)_{in}} \qquad (2)$$

$$S_{H_2} = \frac{\dot{n}_{H_2}}{\dot{n}_{H_2} + \dot{n}_{H_2O}} \quad (3)$$

$$S_{CO} = \frac{\dot{n}_{CO}}{\dot{n}_{CO} + \dot{n}_{CO_2} + \dot{n}_{C(S)}} \quad (4)$$

$$S_{C(S)} = \frac{\dot{n}_{C(S)}}{\dot{n}_{CO} + \dot{n}_{CO_2} + \dot{n}_{C(S)}} \quad (5)$$

Figures 24-26 present the thermodynamic equilibrium analysis for catalytic partial oxidation of a clean model biogas with a CH_4/CO_2 ratio of 1.5 for different air/biogas ratios (or air ratios - λ) and different temperatures at atmospheric pressure. The air ratio (λ) evaluated according to expression (6) where X_k corresponds to the molar fraction of species k.

$$\lambda = \frac{X_{O_2}}{2X_{CH_4}} \quad (6)$$

For isothermal conditions Figure 24a shows that as the air ratio (λ) decreases the carbon formation increases until the value achieved corresponds to the case of biogas catalytic decomposition (for the absence of air addition). Moreover a decreasing trend on air ratio leads to an increase in the H_2/CO ratio. Figure 24b shows a complete conversion of O_2 and a negative conversion of CO_2 for an air ratio of 0.4 at medium temperatures which points out an overall CO_2 production instead of consumption. Figure 24b also shows that increasing the reactor temperature the selectivity of C(S) decreases whereas the selectivity of CO increases. The H_2 selectivity at high reactor temperatures starts to decrease which reveals a competition between partial and total oxidation reactions of methane.

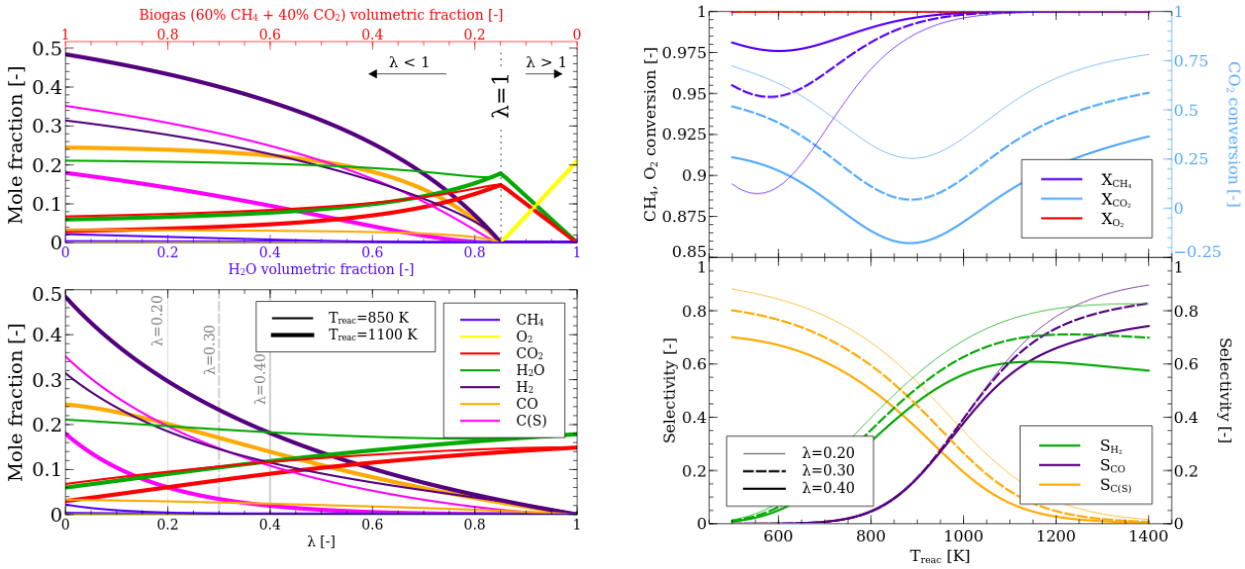

(a) (b)

Figure 24. Thermodynamic equilibrium calculations considering isothermal and isobaric (1 atm) conditions: a) product composition as a function of the O_2/CH_4 ratio (or λ) for two reactor temperatures; b) CH_4, CO_2 and O_2 conversions and H_2, CO and C(S) selectivities as a function of the reactor temperature for three λ values.

The O_2 addition to the biogas mixture allows the conversion of methane through an exothermic route (see reactions R1 and R9). The heat release will be utilized to drive endothermic reforming reactions allowing a higher H_2 and CO yields and a higher fuel conversion. For these reasons the operation of biogas CPOx is suitable in adiabatic reactors (through an autothermal ($\Delta H_R < 0$) or thermoneutral ($\Delta H_R = 0$) regime) unlike the previous strategies for biogas reforming (catalytic decomposition and steam reforming) which require an operation in an allothermal regime.

Figure 25 presents the equilibrium reaction results at adiabatic and atmospheric conditions for different air ratio values and inlet temperatures. Figure 25a shows that the coking boundary slightly decreases as the inlet reactor temperature increases: it decreased from λ=0.38 to λ=0.34 when the inlet temperature increased from 600 to 850 K. Low air ratio values allow a higher H_2 molar fraction however the carbon formation increases significantly. Figure 25b demonstrates a complete O_2 conversion and a significant loss in the H_2 selectivity clearly visible at high temperatures as the air ratio increases.

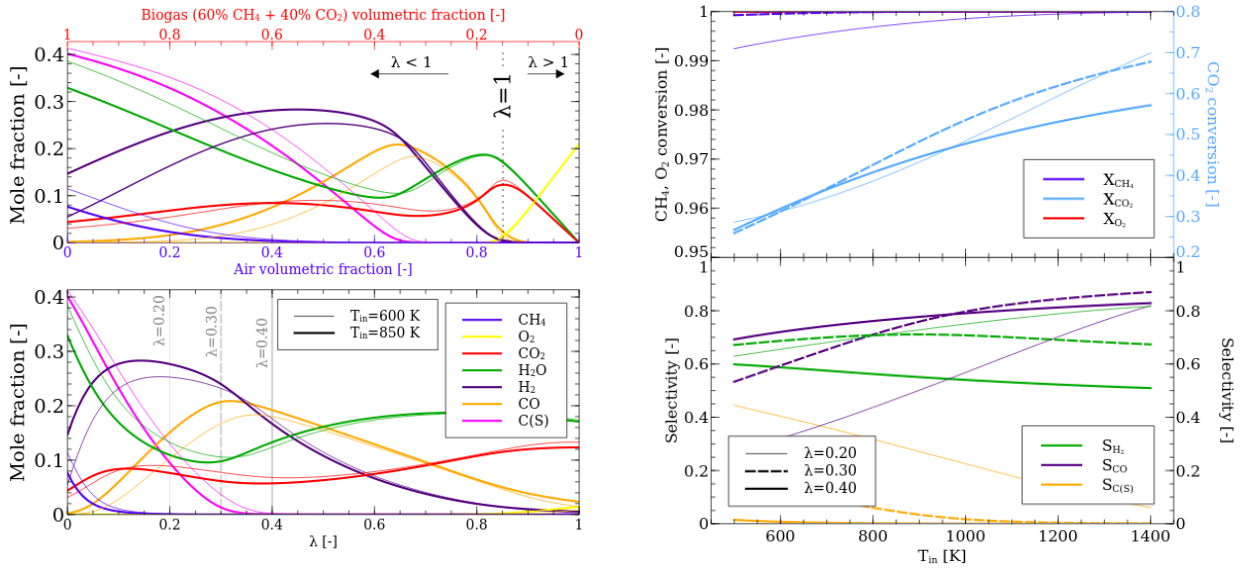

(a) (b)

Figure 25. Thermodynamic equilibrium calculations considering adiabatic and isobaric (1 atm) conditions: a) product composition as a function of the O_2/CH_4 ratio (or λ) for two inlet temperatures; b) CH_4, CO_2 and O_2 conversions and H_2, CO and C(S) selectivities as a function of the inlet temperature for three λ values.

The adiabatic temperature rise for several inlet mixture conditions is presented in Figure 26. As the air ratio increases (until slightly before unity) the overall reaction exothermicity increases as Figure 26a shows. In Figure 26b the reaction exothermicity decreases with the inlet reactor temperature well noticeable for the two lower air ratio values (0.20 and 0.30). Particularly, for the lowest air ratio value at temperatures above 1100 K an overall reaction endothermicity is observable.

Thermodynamic equilibrium analysis of the simultaneous dry reforming and partial oxidation of methane can be found in reference [2,75,120].

A compilation of the relevant experimental works available in the area of biogas catalytic partial oxidation is presented in Table 5.

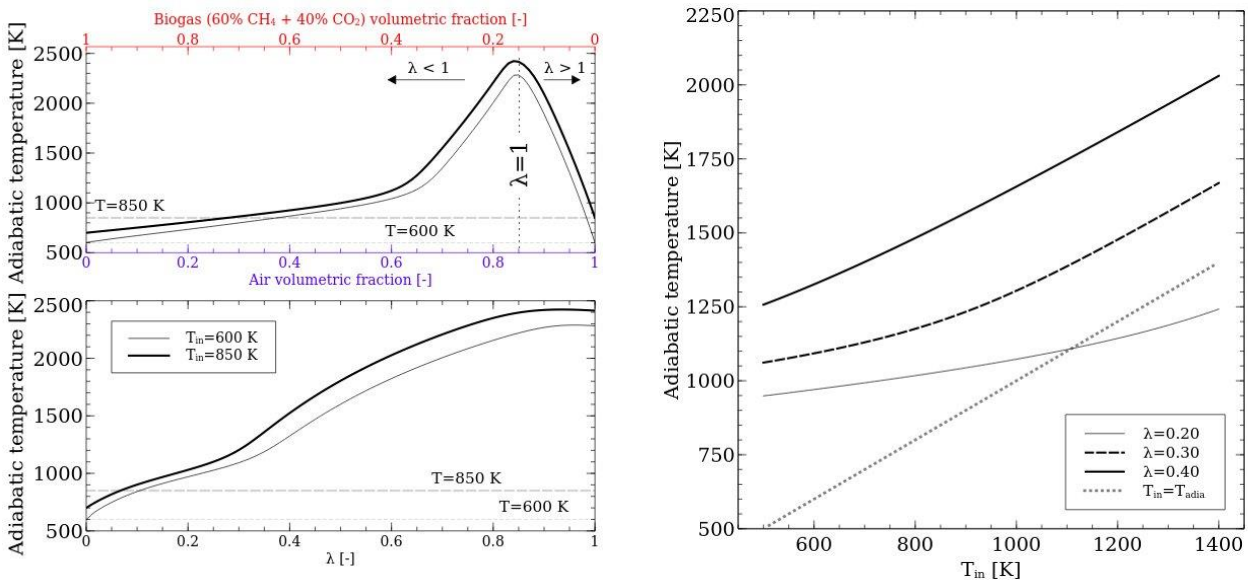

(a) (b)

Figure 26. Adiabatic temperature rise: as a function of the O_2/CH_4 ratio (or λ) for two inlet temperatures (a); as a function of the inlet reactor temperature for three λ values (b).

Table 5. Literature survey on catalytic partial oxidation of biogas (oxidative dry reforming of methane).

Metal	Support	Motivation	Mix. Conditions		Ref.
			CO_2/CH_4	λ	
Ni	MgO; Al_2O_3; SiO_2	Support effect on catalyst stability and activity; effect of O_2/CO_2 ratio on the product H_2/CO ratio	0.05-0.50	0.12-0.18	80
Co	MgO; CaO; SiO_2	Effect of the support; catalyst stability and activity; effect of O_2/CO_2 ratio on the product H_2/CO ratio	0-1	0-0.13	79
Rh; Ru; Pt; Pd; Ir	$MgAl_2O_4$	Catalyst activity and stability; effect of temperature, λ and SV	1.0	0.15-0.50	119
Rh	Al_2O_3	**Catalyst stability; hot-spot formation; validation of CFD predictions**	**1; 1.18**	**0.25; 0.29**	**72**
Rh	**Al_2O_3**	**1D model validation; process optimization; reforming strategy adequacy for SOFC**	**0.54**	**0.20-0.39**	**54**
Pt-Rh	$Ce_{0.75}Zr_{0.25}O_2$ – Al_2O_3	Effect of inlet temperature, GHSV and O_2/CH_4 ratio on reactor temperature and performance	0.67	0.08-0.29	26
Rh	**Al_2O_3**	**Catalyst deactivation; carbon formation; comparison with biogas catalytic decomposition**	**1; 0.71**	**0.23**	**25**
Pt-Rh	CeO_2 – Al_2O_3	Effect of operation conditions on methane conversion and syngas selectivity; coke formation	0-1	0.25-0.50	74
Ni	ZrO_2; MgO	Influence of MgO on NiO/ZrO_2 in terms of overall catalyst performance; catalyst stability	0.67	0.08	81
Ni	ZrO_2; Y_2O_3	Role of Y_2O_3 on NiO/ZrO_2 in terms of overall catalyst performance; catalyst stability	0.67	0.08	78
Ni	Al_2O_3	Comparison with biogas catalytic decomposition, coke deposition, biogas CPOx reactor integration in a pilot-scale unit for H_2 production	0.77	0.05-0.38	2

Studies in bold are referred along the main text.

Most of the earlier work found in the open literature on the subject of simultaneous dry and catalytic partial oxidation of methane does not even refer to biogas applications. Ashcroft et al. [18]

recommended the addition of oxygen to the inlet feed stream in order to decrease the heat requirements of dry reforming. Ruckenstein and Hu [80] suggested that the addition of CO_2 to the partial oxidation of methane could decrease the hot-spot formation. Other earlier works focused on the catalyst development and their characterization. Even with no direct reference to biogas, most of these works are a valid and valuable contribution to the biogas reforming if the catalyst characterization experiments were performed under CH_4/CO_2 ratios typical of those encountered in clean model biogas mixtures. This is the case of the first three works in Table 5.

Due to the advantages mentioned for biogas reforming through catalytic partial oxidation over the catalytic decomposition or steam reforming route, the CPOx of biogas has received more attention concerning practical applications. Murphy et al. [54] assessed the fuelling of a SOFC with reformate derived from different biogas reforming strategies: CPOx with air and pure oxygen and steam reforming. They found that the biogas CPOx with pure O_2 return the highest cell performance among the remaining biogas reforming strategies, just 3% lower than the performance achieved with pure H_2. The applicability of biogas CPOx for downstream Fischer-Tropsch synthesis and for PEM fuel cells is slightly discussed by Kohn et al. [25] due to the tunable H_2/CO ratio with the reactor temperature.

Several numerical works were carried out under the topic of biogas catalytic partial oxidation (or oxidative dry reforming of methane with appropriate CH_4/CO_2 ratios). The main focus and remarks in the computational modelling were attributed to the employed kinetic model. In particular Ding et al. [72] found that the CO_2 adsorption rate of the detailed reaction mechanism from Deutschmann et al. [76] for methane CPOx over Rh catalysts was inadequate for the case of a relevant addition of CO_2 to the inlet feed stream, as the case of biogas. They proposed a modification for the kinetics of CO_2 adsorption and the CO_2 conversions predicted by the model agreed well with their experimental data. A similar conclusion was drawn by Murphy et al. [54] during numerical analysis of biogas CPOx with pure oxygen. They applied the microkinetic mechanism from Schädel et al. [77] (which is an improvement of the earlier methane CPOx mechanism from Deutschmann et al.) and found that the methane dry reforming reaction was under predicted, especially at low reactor temperatures, leading to a lower methane conversion than that experimentally measured.

3.2 Other catalytic reforming strategies

In the present section the discussion is prolonged to other three catalytic routes with practical interest to obtain synthesis gas from biogas mixtures. The discussion intends to expose in a brief overview the well-known principles of such reforming strategies directed for methane as the fuel and further extended to methane-carbon dioxide mixtures mimicking clean biogas compositions in a deep literature review.

3.2.1 Catalytic decomposition

Overview

In practice the catalytic decomposition of biogas consists in the well-known CO_2 reforming of methane (also recognized as stoichiometric reforming or dry reforming of methane, shortly DRM) with a specific CH_4/CO_2 ratio dictated by the biogas composition [30,41]. Methane dry reforming was proposed by Fischer and Tropsch in 1928 [3] and it has been exhaustively studied well before the current concern on the valorisation of biomass-derived gases into a higher added-value

compounds such as synthesis gas. Due to this reason a large number of experimental and theoretical studies on methane dry reforming can be directly considered relevant for the biogas catalytic decomposition process.

Dry reforming of methane, globally expressed through reaction (R2), is a strongly endothermic reaction ($\Delta H_R^\circ = 249\ kJ/mol$) being favoured by high temperatures and low pressures. Alongside with the direct reaction route from the fuel mixture to the desired products (R2) other competitive reactions may take place, namely the methane thermal decomposition (methane cracking reaction) (R3), CO disproportionation reaction (Boudouard reaction) (R4), methane steam reforming to CO (R5) and to CO_2 (R6), water-gas shift (R7) and CO reduction reaction (R8). Reactions R3, R4 and R7 explain the elemental carbon predicted by thermodynamic equilibrium calculations and also the carbonaceous deposits encountered in experimental studies. In general reactions R3 and R4 are claimed to be the main reaction pathways for carbon formation [21] but reaction R8 cannot be ruled out [9]. Methane decomposition reaction (R3) is favoured by high temperatures (above 560 ºC) and low pressures while the presence of CO disproportionation reaction (R4) in the overall reaction scheme decreases by increasing the temperature (above 700 ºC its contribution is negligible) and decreasing the pressure [4-5].

Due to its overall endothermicity dry reforming of methane is usually carried out in reactors placed inside ovens/furnaces to keep the catalyst temperature near isothermal conditions. Its industrial and large scale application is limited due to the several reasons, namely the high pressures usually applied to make the process economically sustainable are not adequate for high methane conversion (according to thermodynamics) [4-5], the loss of catalytic activity due to sintering and support phase transformations [7] but mainly the strong tendency to carbon deposition onto the catalyst surface that leads to its rapid deactivation is by far the major problem that concerns a large scale implementation of the dry reforming technology [4-6,7-9, 16].

The deposition of carbon on the catalytic surface leads to the blockage of catalytic active sites and pores of the catalyst support structure leaving the catalyst particles inaccessible to reactant species and ultimately leading to a complete support disintegration due to growth of carbon particles in the pore structure [1-2]. Moreover, the carbon deposits may also cause an increase in the pressure drop [57] along the reactor or limit the heat transfer in externally heated reforming units [45]. Several strategies have being proposed to avoid carbon lay down namely adding oxidizing agents to the feedstock mixture, employing catalysts that inhibit methane decomposition and coke formation and operate under conditions that thermodynamically do not favour carbon formation.

Nevertheless, dry reforming of methane presents several advantages over other reforming strategies. Dry reforming allows the mitigation of two greenhouse gases while producing synthesis gas with a low H_2/CO ratio which is preferable for downstream Fischer-Tropsch synthesis [6,8] and oxygenated compounds [4]. DRM can also be used to reform a poor quality natural gas with a high CO_2 content [9] or biomass-derived gases without using other oxidizing agent, such as H_2O or O_2 [2,10, 27].

The performance of the dry reforming of methane under isothermal and isobaric conditions predicted by the chemical equilibrium calculations is presented in Figure 27a for the product composition and in Figure 27b for CH_4 and CO_2 conversions and H_2, CO and C(S) selectivities.

Figure 27a reveals that solid carbon is always present in some quantity depending on the mixture composition and the reactor temperature. In particular as the reactor temperature increases the maximum value of C(S) is shifted towards higher values of CH_4/CO_2 ratio in such a way that at 1100 K the maximum molar fraction of C(S) is observed in the absence of CO_2. The equilibrium composition of the pure methane decomposition reaction (CO_2/CH_4=0) reveals that as the reactor

temperature increases a higher methane conversion is achieved (denoting the overall endothermicity of reaction R3) and the H_2/C(S) ratio equals to 2.

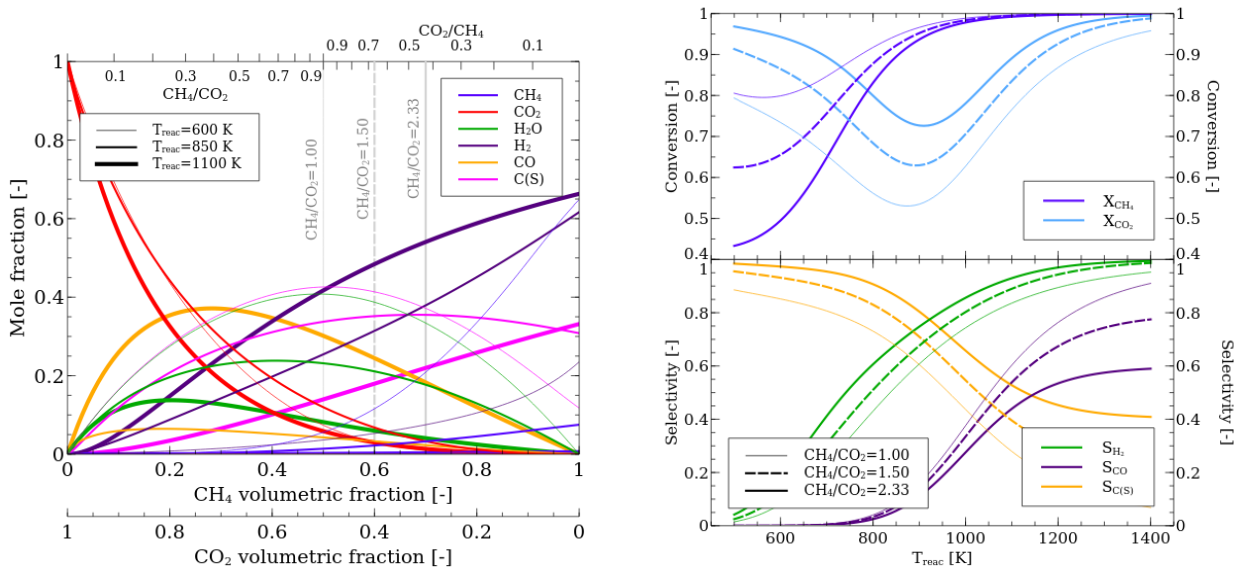

(a) (b)

Figure 27. Thermodynamic equilibrium calculations considering isothermal and isobaric (1 atm) conditions: a) product composition as a function of the CH_4/CO_2 ratio for three reactor temperatures; b) CH_4 and CO_2 conversions and H_2, CO and C(S) selectivities as a function of the reactor temperature for three CH_4/CO_2 ratios.

Figure 27b shows that as the CH_4/CO_2 ratio increases for each reactor temperature the CO_2 conversion increases as well as H_2 and C(S) selectivities whereas the CH_4 conversion and CO selectivity decrease. Independently of the mixture composition C(S) has a high selectivity at low reactor temperatures. As the reactor temperature increases the selectivities of H_2 and CO increase as well whereas the C(S) selectivity decreases. For the particular case of an equimolar reacting mixture (CH_4:CO_2=1:1) the selectivity of C(S) become negligible at high reactor temperatures whereas the equilibrium H_2/CO ratio approximates a value of 2 in agreement with the stoichiometry of methane dry reforming reaction (R2). However, for mixtures with a CH_4/CO_2 ratio higher than 1 carbon formation is always expected at high reactor temperatures as well as an increase in the H_2/CO ratio as result of an increasing contribution of the methane cracking reaction.

Regarding adiabatic and isobaric conditions Figure 28a presents the thermodynamic equilibrium composition of the product mix whereas Figure 28b shows the CH_4 and CO_2 conversions and H_2, CO and C(S) selectivities. By direct comparison between Figures 27 and 28 one can see a lower ability towards the decomposition reaction of CH_4-CO_2 mixtures in adiabatic reformers which in practice justify the external heat supply required for dry reforming reactors. In particular, considering an equimolar CH_4-CO_2 mixture the H_2 selectivity during adiabatic operation attains a maximum value of about 0.6 for 1400 K whereas at isothermal conditions a selectivity of H_2 near 0.95 is expected for the same temperature value (see Figures 28b and 27b).

Figure 29a shows the adiabatic temperature rise as a function of the CH_4/CO_2 ratio for three reactor temperatures (600, 850 and 1100 K). Considering an inlet temperature of 600 K it can be seen that the overall reaction can be slightly exothermic up to CH_4/CO_2 ratio equal to 1.5. However, this range of CH_4/CO_2 ratio at the mentioned inlet temperature gives poor reformates with H_2 and CO concentrations quite far from the reaction capabilities at isothermal conditions.

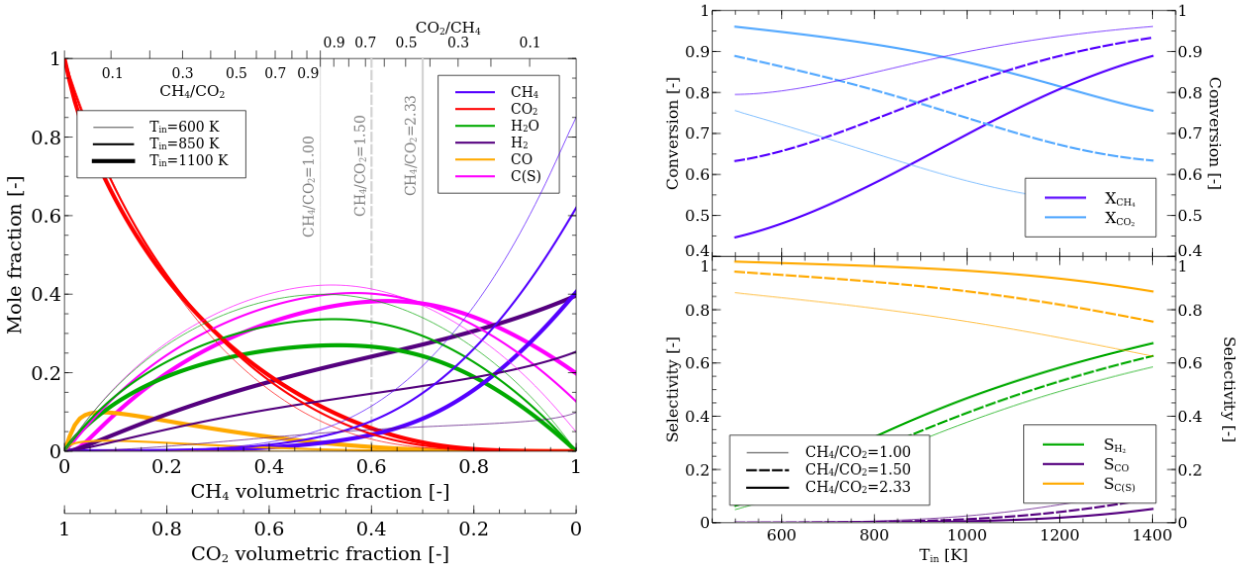

(a) (b)

Figure 28. Thermodynamic equilibrium calculations considering adiabatic and isobaric (1 atm) conditions: a) product composition as a function of the CH_4/CO_2 ratio for three inlet temperatures; b) CH_4 and CO_2 conversions and H_2, CO and C(S) selectivities as a function of the inlet temperature for three CH_4/CO_2 ratios.

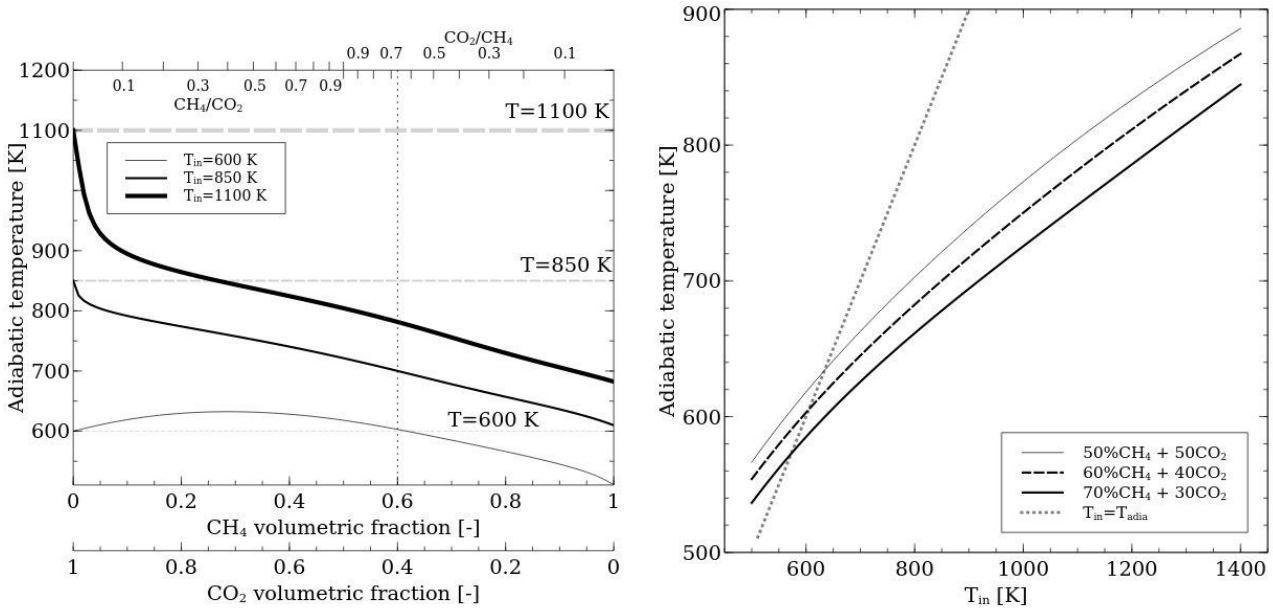

(a) (b)

Figure 29. Adiabatic temperature rise: as a function of the CH_4/CO_2 ratio for three inlet temperatures (a); as a function of the inlet temperature for three CH_4/CO_2 ratios (b).

The presence of large amounts of C(S) predicted in the equilibrium mix turns unattractive, at the first glance, the catalytic decomposition of biogas. As it was seen CH_4/CO_2 ratios below unity at high temperatures decreases the tendency to coking (see Figure 27a). However, in practise and for biogas mixtures these conditions may not be fulfilled due to the biogas composition and the high energy requirements [6].

Extensive thermodynamic equilibrium studies on the catalytic decomposition of biogas or on methane dry reforming with appropriated CO_2/CH_4 ratios can be found elsewhere [61, 39, 2].
An alternative to avoid carbon deposition under practical operating conditions that thermodynamic calculations predict a high level of carbon formation consists in the selection of adequate catalyst formulations and supports that under kinetic control inhibit coke formation [4,6].
The development of catalyst formulations that exhibit high activity, stability and selectivity towards dry reforming of methane has become an extremely active research area [7-9, 20, 24]. This development has been focused mainly in the nature of the support [21], the catalyst preparation method [16] and effect of promoters [23]. Ni-based catalysts due to the reasons mentioned above are the by far the most preferred catalyst to develop and improve [16, 20-21].
Dry reforming of methane has been conducted over a wide range of catalysts [4,6,14-15]. Rostrup-Nielsen and Hansen [17] performed a series of experiments with MgO supported Ni and noble metal catalysts at 550 ºC and concluded the following relative order of activity for dry reforming of methane:

$$Ru > Rh, Ni, Ir > Pt > Pd \ (550ºC;\ 1atm,\ CH_4/CO_2=0.25;\ CH_4/H_2=2.5)$$

Ni-based catalysts are by far the most preferable due to the Ni high availability and its low cost comparing with other transition metal catalysts, in particular with precious metal catalysts [7,16]. Ni-based catalysts present high activity for dry reforming of methane but at the same time are highly active for methane decomposition, CO disproportionation and CO reduction reactions and for this reason these catalyst are prone to deactivate by carbon deposition [17]. Conversely, noble metal catalysts (Platinum Group Metal catalysts expect Os) are known to be less active for carbon-forming reactions and then present a higher coking resistance [17-18]. Rostrup-Nielsen and Hansen [17] found the following decreasing sequence of carbon deposition:

$$Ni >> Rh > Ir > Ru\ ,\ Pt,\ \ Pd \ (500ºC;\ 1atm,\ CH_4/H_2=95/5\ vol/vol)$$

Bimetallic catalyst formulations, such as Ni-Pd, Ni-Pt, Ni-Ru, Ni-Cu or Ni-Co, are also used in practice due to the better performance achieved when compared to the monometallic formulations [16,20,22]. Steinhauer et al. found that the activity of Ni-Pd bimetallic catalysts for DRM depends strongly on the nature of the supports with the following activity decreasing sequence: ZrO_2-La_2O_3, $La_2O_3 > ZrO_2 > SiO_2 > Al_2O_3 > TiO_2$ [22].
Several types of supports have been used as carriers for catalyst particles, such as Al_2O_3, SiO_2, TiO_2, MgO or ZrO_2 [4,6,15]. Mixed metal oxides such as $MgAl_2O_4$, La_2NiO_4 or $Ce_xZr_{1-x}O_2$ have also been used [7]. During operation the supports must be resistant to thermal degradations and they have to guarantee a high dispersion of the metal crystallites onto their surfaces [7]. It is well known that the support composition through its interaction with the metal catalyst also controls the carbon formation rate [19,21,49]. In particular a strong interaction metal-support increases the catalyst stability against thermal sintering [48,80] and consequently against carbon deposition since metal sintering contributes to enlarge the metal ensembles onto the support surface which leads to a higher carbon formation [49]. The Lewis acidity of the metal oxide supports has also an important role on the catalyst stability. Supports with a high basicity present a lower susceptibility to deactivate by coke deposition due to strong CO_2 adsorption with the surface that favors the carbon gasification through the reverse Boudouard reaction [47]. For metal-oxide supported Pt catalysts Bitter et al. observed that the rate for carbon deposition decreases in the order Pt/γ- Al2O3 >> $Pt/TiO_2 > Pt/ZrO_2$ [19].

It has been shown that a minimization of the carbonaceous deposits can also be achieved through the packing arrangement of the catalyst bed. Fluidized-bed reactors instead of fixed-bed reactors are less prone to carbon deposition [104-105]. Moreover, the temperature field in a fluidized-bed reactor is expected to be more uniform hindering the presence of cold spots that appear in the fixed-bed configuration which are responsible for a decrease in the fuel conversion [106, 42]. However, a loss of the active phase through attrition is also expected as the time-on-stream increases [42].
Comprehensive reviews on the DRM topic can be found elsewhere [4,6,9,14,15].

Biogas catalytic decomposition

Regarding the catalytic decomposition of biogas which is in fact the DRM with a characteristic CH_4/CO_2 ratio, only recently it received a considerable attention in the open literature. Perhaps due to the high propensity to coke deactivation during catalytic decomposition of biogas under typical conditions, limited applications involving biogas catalytic decomposition have been reported. The main focus has been related to the development of catalytic formulations that under typical CH_4 rich CH_4-CO_2 mixtures present high stability (against carbon formation and metal sintering) high activity and high selectivity to synthesis gas. Therefore, in the following it is provided a literature survey on the catalytic decomposition of biogas denoting the experimental effort on the catalyst development. Table 6 presents briefly the work available in the literature involving a direct reference of biogas catalytic decomposition or dry reforming of methane with a suitable CH_4/CO_2 ratio.

Table 6. Literature survey on catalytic decomposition of biogas (dry reforming of methane).

Metal	Support	Motivation	Mix. Conditions CO_2/CH_4	Ref.
Rh; Pt; Pd; Ir; Ru; Ni; NiO	Al_2O_3 (for noble metals); Al_2O_3, kieselguhr; Ca aluminate	Catalyst selectivity, activity and stability; carbon deposition; applicability to Fischer-Tropsch synthesis	0.77	1
Rh	Al_2O_3	Performance of a 400 cpsi cordierite honeycomb monolith; catalyst activity; carbon deposition; catalyst regenerability capacity	0.71;1.0	25
Pt-Rh	CeO_2 – Al_2O_3	Effect of operating conditions (GHSV, temperature) on integral product distribution and thermal profiles	0.67	26
Ru; Rh	Al_2O_3 (for Ru); CeO_2 (for Rh)	Effect of temperature on catalyst activity and stability; carbon formation; metal sintering	0.43; 0.67; 1.00; 1.50	28
Ni	Al_2O_3; CeO_2 – Al_2O_3	Effect of Ceria addition to alumina; catalyst activity selectivity and stability; carbon deposition	0.67	29
Ni; Ni-Pd	Al_2O_3; P- Al_2O_3	Effect of Phosphorus content on the activity and selectivity of alumina supported Ni-Pd catalysts	1.00	36
Ni	La_2O_3 - Al_2O_3	Catalyst stability and activity; H_2/CO ratio achieved	1.00	33
Ni-Co	La_2O_3 - Al_2O_3	Effect of operating conditions on the catalyst performance; catalyst stability; effect of reactor lining material and packing manner	1.00	30
Ni	Al/Mg; La/Al/Mg	Effect of La addition; catalyst activity and stability; carbon deposition	1.00	35
Ni	La/Al/Mg	Influence of catalyst calcination temperature on its activity and stability; coke deposition	1.00	36
Ni-Rh; Ni	La_2O_3 - Al_2O_3; Al_2O_3	Effect of Rh and La_2O addition on Ni/ Al_2O_3 catalyst; CH_4 conversion; carbon deposition	0.67	32

Ni; Co; Ni-Co	$MgO-Zr_2O_3$	Catalyst activity and stability; synergy between Ni-Co metals; coke deposition; regenerability capacity	1.00	37
Ni	Al_2O_3	Catalyst activity, selectivity and stability under different reactor temperatures; formation of carbon nanofibres with high added value.	1.00	39
Ni	Al_2O_3	Effect of temperature, SV and CH_4/CO_2 on biogas conversion, H_2/CO ratio and carbon formation; catalyst deactivation	0.43; 0.67; 1.00	40

Muradov and Smith [1] preformed an experimental campaign to determine the selectivity, activity and stability of noble metal (Rh, Pt, Pd, Ir and Ru) and Ni-based catalysts during the decomposition of a biogas mixture with a CH_4/CO_2 ratio of 1.3. After 5h operation under a catalyst temperature of 850 ºC and 1 atm Ru and Ir were the catalysts with the highest activities and selectivities for dry reforming of methane with undetectable amounts of graphite followed by Pt, Rh and Pd. Ni-based catalysts presented initially a high activity with its product distribution comparable with thermodynamic predictions but as the time-on-stream increased this catalyst revealed the worst performance with a rapid deactivation and further disintegration due to carbon particle growth in the porous structure of the support (Al_2O_3). The authors also reported that due to the low H_2/CO ratio (ca. 1) and unconverted methane in the reformate mixture the catalytic decomposition may not be suitable for production of liquid hydrocarbons through the Fischer-Tropsch synthesis.

Kohn et al. [25] explored the performance of a 400 cpsi cordierite honeycomb monolith washcoated with 4% $Rh/\gamma-Al_2O_3$ during the catalytic decomposition of two CH_4/CO_2 mixtures (with molar ratios of 1.0 and 1.4) diluted in N_2 under 1 atm and a temperature range from 300 to 700 ºC. No traces of carbonaceous deposits were observed with the lower CH_4/CO_2 ratio (although it should be highlighted the high N_2 dilution of about 87%). For the CH_4/CO_2 ratio of 1.4 a dilution with 14% N_2 was considered to simulate a typical landfill gas mixture and carbon formation was observed after 24h operation by the darkening of the catalyst and its noticeable loss of activity. However, the spent catalyst showed the ability to its regeneration, covering its initial activity after exposure to an air stream.

Lau et al. [26] employed a 900 cpsi cordierite honeycomb monolith coated with a commercial catalyst formulation discriminated as a bimetallic 2% Pt – 1% Rh catalyst dispersed on a mixed oxide support (30% $Ce_{0.75}Zr_{0.25}O_2$ – 70% $\gamma-Al_2O_3$). They considered a clean model biogas mixture with only CH_4 and CO_2 with a CH_4/CO_2 ratio of 1.5 under an inlet temperature range between 400 and 900 ºC and 1 atm. For two GHSV values the product distribution was recorded along the stated temperature range as well as the thermal profile along the catalyst bed for an inlet temperature of about 700 ºC. The experimental mixture composition observed was in qualitative agreement with thermodynamics in the temperature range and for the higher GHSV value a decrease in the catalytic activity was observed as a result of a decrease in the overall residence time. Regarding the carbon formation issue, no data was provided even that from thermodynamic equilibrium calculations in the range of operating conditions mention C(S) presents a high molar fraction (see Figure 27b).

The performance of 3% Ru/Al_2O_3 and 2% Rh/CeO_2 catalysts to catalytic decomposition of undiluted CH_4-CO_2 mixtures with CH_4/CO_2 ratios of 0.67, 1, 1.5 and 2.33 was conducted by Djinovíc et al. [28] at reactor temperatures from 400 to 750 ºC with a constant total flow rate of 92 NmL/min. An increasing trend for coking in both catalysts for each temperature step was observed increasing the CH_4/CO_2 ratio leading the authors to conclude that CH_4 is the primary source of carbon. Nevertheless, the carbon formation registered was in general negligible contradicting thermodynamic predictions. During the temperature programmed activity tests the Ru-based catalyst started to deactivate at temperatures above 500 ºC which was attributed to sintering of

metal clusters. Rh-based catalyst achieved a higher activity towards CH_4 and CO_2 conversion in all tested conditions.

The effect of adding ceria to alumina supports of Ni catalyst was investigated by Bereketidou and Goula [29]. They characterized the performance of 3 alumina supported Ni catalysts (8% Ni/ γ-Al_2O_3, 8% Ni/10% CeO_2 - γ-Al_2O_3 and 8% Ni/20% CeO_2 - γ-Al_2O_3) under 1atm, over a temperature range between 700 to 900ºC and with a total flow rate of 200 mL/min. A CH_4/CO_2 ratio of 1.5 was considered as well as a 50% dilution with He. At temperatures above 800 ºC the CeO_2 - γ-Al_2O_3 supported Ni catalysts showed a slightly higher fuel conversions then the Ni/ γ-Al_2O_3 catalyst. Moreover, the catalyst with the higher Ce content evolved the best catalytic performance with an H_2/CO ratio of about 1.3 being suitable for methanol and Fischer-Tropsch synthesis. A 5 h exposure of the Ni catalyst with the higher Ce content at 860 ºC revealed an insignificant carbon formation.

The influence of Phosphorus content on the activity of alumina supported Ni-Pd catalysts for a stoichiometric methane dry reforming reaction at atmospheric pressure and 973 K was discussed by Damyanova et al. [36]. Over a period of 400 min they examined the catalytic activity and stability of Ni/AL2O3, Ni-Pd/Al2O3 and four Ni-Pd/P-Al2O3 catalyst samples containing different amounts of P (0.5,1, 3 and 5 wt%). The best catalytic performance (higher fuel conversion and syngas yield) was verified with the catalyst sample containing the minimum amount of P.

An interest on the role of Lanthanum oxide or Lanthana (La_2O_3) in the support composition has been visible in several literature works for biogas reforming applications through dry reforming of methane. This is due to the well-known Lanthana role in preserving the catalyst stability against coke deposition [34]. Benito et al. found that the 5%Ni / 5% La_2O_3 – γ-Al_2O_3 catalyst achieved an excellent stability after 40 h exposure to an undiluted CH_4-CO_2 mixture (CH_4/CO_2=1) under kinetic regime [33]. Xu et al. [30] performed a detailed characterization of the influence of operating conditions on the performance of a 7% Ni - 3% Co/6% La_2O_3-Al_2O_3 catalyst previously suggested by them as an excellent catalyst for biogas decomposition [31]. They recall that the reaction temperature and the operating pressure can considerably influence the catalyst performance. In long term stability experiment (310 h) carried out in a quartz reactor a dynamic equilibrium between the rate of carbon deposition and gasification can be reach. A similar experiment using a stainless steel reactor revealed that with the quartz reactor a lower carbon deposition on the catalyst is observed denoting the effect of the stainless steel to catalyze carbon formation. Serrano-Lotina et al [35] after a 50 h operation experiment with Ni/Al/Mg and La-promoted Ni/Al/Mg catalysts exposed to a clean and undiluted biogas mixture (CH_4/CO_2=1) at 700 ºC found that the catalyst without La had an higher activity but on the other hand the La addition provided a significant improvement of catalyst stability with no coke deposition. In other work Serrano-Lotina warns about the preparation method (namely the selection of the calcination temperature) of La promoted NiMgAl catalyst on its activity and stability [36].

Experimental investigations considering a synthetic biogas mixture with a CH_4/CO_2 ratio of 1.5, diluted in 25% of N_2 showed that bimetallic Ni-Rh catalyst supported on La_2O_3-Al_2O_3 return an higher CH_4 conversion and an insignificant carbon deposition compared to monometallic Ni catalysts supported on La_2O_3-Al_2O_3 or only on Al_2O_3 and bimetallic Ni-Rh catalysts supported only on Al_2O_3 [32]. Similar results were reported by Fan et al. [37] but for bimetallic Ni-Co supported on MgO-Zr_2O_3 catalyst. After a 40 h time-on-stream test at 750 ºC with an equimolar CH_4-CO_2 mixture a constant catalytic activity and high fuel conversion were observed. The performance of the bimetallic catalyst was considered better than the performance of monometallic Ni and Co supported on MgO-Zr_2O_3 catalysts. Moreover the bimetallic catalyst demonstrated an excellent regenerability capacity after to coke deposition by restoring almost 100% of its catalytic activity.

The valorization of nanostructured carbonaceous materials that are produced along with syngas during the catalytic decomposition of biogas in Ni/Al_2O_3 catalysts was also suggested to increase the overall process sustainability [39-40].

3.2.2 Steam reforming

Overview

The first historical efforts available on the description of the hydrocarbons conversion with steam were reported in 1868 with CaO [50] and latter in 1890 with a Ni catalyst [51]. Today, the steam reforming (SR) of methane is a well-stabilised technology being the most important industrial process to produce synthesis gas and H_2. For more than 40 years steam reforming is a commercially available technology [44] and nowadays it is estimated that 40% of the worldwide hydrogen production is accomplished in steam reformer units consuming mainly natural gas and naphtha [5, 110]. In large-scale facilities steam reforming of methane is carried out in fired tube furnaces at temperatures between 850-900 ºC, under high pressures (2 – 4 MPa) to keep the whole reactor compact and decrease its capital cost [45] and with steam to methane ratios of 2.3 to 3.0, higher than the suggested by the stoichiometry of the steam methane reforming reaction R5 to avoid the carbon formation regime [46]. Ideally, steam reforming as dry reforming of methane would be conducted at low pressures and high temperatures.
Rostrup-Nielsen and Hansen [17] observed the following order of catalyst activity for methane steam reforming:

$$Ru, Rh > Ir > Ni, Pt, Pd \ (550ºC;\ 1atm,\ CH_4/H_2O=0.25;\ CH_4/H_2=2.5)$$

Despite the higher activity shown by noble metals Ru, Rh and Ir, Ni-based catalysts supported on alumina are extensively preferred due to its large availability and relative low cost. Besides Al_2O_3 (α and γ phases) also SiO_2, ZrO_2, MgO, TIO_2 or $MgAL_2O_4$ supports have been used [5]. Even not being so alarming when compared to the dry reforming case, the carbon deposition is also an issue that concerns the steam methane reforming technology due to the high propensity for carbon formation in Ni-based catalysts [17, 45]. Besides the excess of steam in the feedstock or the alkalization of the catalyst carrier [44] the sulphur passivation of the catalyst was also proposed to decrease the carbon formation since it allows to control the size of the metal crystallites disfavoring the larger metal ensembles [52]. Despite carbon formation, three other challenges, catalyst activity, sulphur poisoning and sintering were highlighted in the literature for the industrial steam reforming technology [45].

Biogas steam reforming

Biogas steam reforming is essentially the simultaneous dry and steam reforming of methane with a CH_4/CO_2 ratio typical of the biogas composition. The set of reactions R2-R8 presented before (see Section 2.1.2) may explain the global dominant reaction pathway in case of simultaneous dry and steam reforming of methane [42]. However, the relative importance of such reactions during biogas steam reforming is not expected to be the same during the catalytic decomposition of biogas. This is the case of methane dry reforming reaction (R2) that will play a minor role in the overall reaction scheme in excess of steam [43].

Figures 30a and 30b present the equilibrium performance at isothermal and isobaric conditions for biogas-H_2O feed mixtures. The biogas composition consists in a clean and undiluted CH_4-CO_2 mixture with a CH_4/CO_2 ratio equal to 1.5 according to a typical biogas composition. The effect of the CH_4/H_2O ratio for two reactor temperatures on the species molar fractions at thermodynamic equilibrium conditions is shown in Figure 30a. For both operating temperatures a similar trend is denoted concerning carbon formation: as the steam content in the inlet mixture increases the carbon formation decreases considerably. For instance, at 1100 K the C(S) mole fraction decreases from 0.18 during the biogas catalytic decomposition (without steam in the feedstock) to 0.07 for the CH_4/H_2O ratio equal to 1. Figure 30b shows that the CH_4 conversion is rather insensitive to the CH_4/H_2O ratio. However, at low reactor temperatures the H_2O and CO_2 conversions reveal that the methane steam reforming reaction (R5) seems to be a preferential reaction pathway to syngas production in spite of the methane dry reforming reaction (R2) which is in accordance to their reaction enthalpies. The increase in the H_2 and CO selectivities as the reactor temperature increases also outstands the strong endothermicity of the steam and dry reforming reactions.

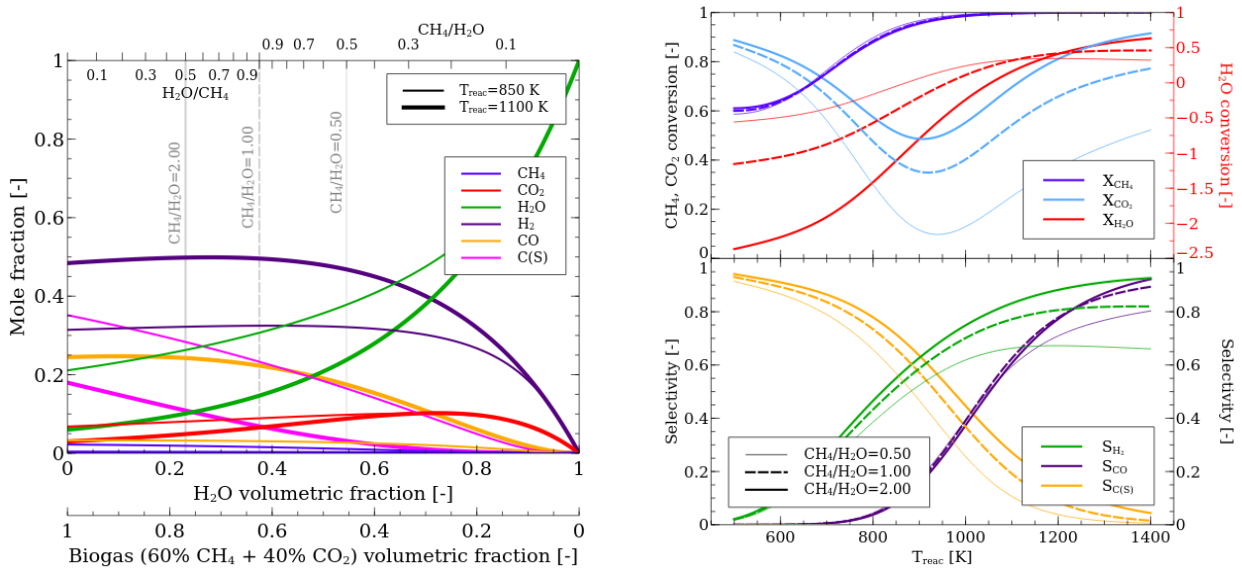

(a) (b)

Figure 30. Thermodynamic equilibrium calculations considering isothermal and isobaric (1 atm) conditions: a) product composition as a function of the CH_4/H_2O ratio for two reactor temperatures; b) CH_4, CO_2 and H_2O conversions and H_2, CO and C(S) selectivities as a function of the reactor temperature for three CH_4/H_2O ratios.

Figures 31a and 31b demonstrate the equilibrium results at adiabatic and isobaric conditions for biogas-H_2O feed mixtures. Both figures exhibit a lower reforming performance than that observed in the isothermal case (compare with Figures 30a and 30b, respectively). Furthermore, Figures 32a and 32b indicate the strong need of external heat supply to convert the biogas-H_2O feedstock into synthesis gas. This explains that an operation under externally heated conditions is by far most profitable for biogas steam reforming than an adiabatic operation.

Thermodynamic equilibrium analysis on the topic of biogas steam reforming or simultaneous steam and dry reforming of methane with appropriated CO_2/CH_4 ratios can be found in references [2,62,63].

The addition of H_2O to the biogas feed stream mixture has advantageous effects over the catalytic decomposition of biogas. It improves the catalyst stability, namely reducing from the

thermodynamics standpoint the carbon deposition and it can be useful to modify the H_2/CO ratio by varying the CH_4/H_2O feed ratio which turns this process flexible and attractive for downstream Fischer-Tropsch synthesis. However, it also requires large amounts of latent heat for its evaporation, increasing the energy cost, and it leads to a decrease in CO_2 conversion [56] (see thermodynamic equilibrium calculation – Figure 30). Nevertheless, the steam reforming of biogas has involved more enthusiasm for practical applications than the biogas catalytic decomposition.

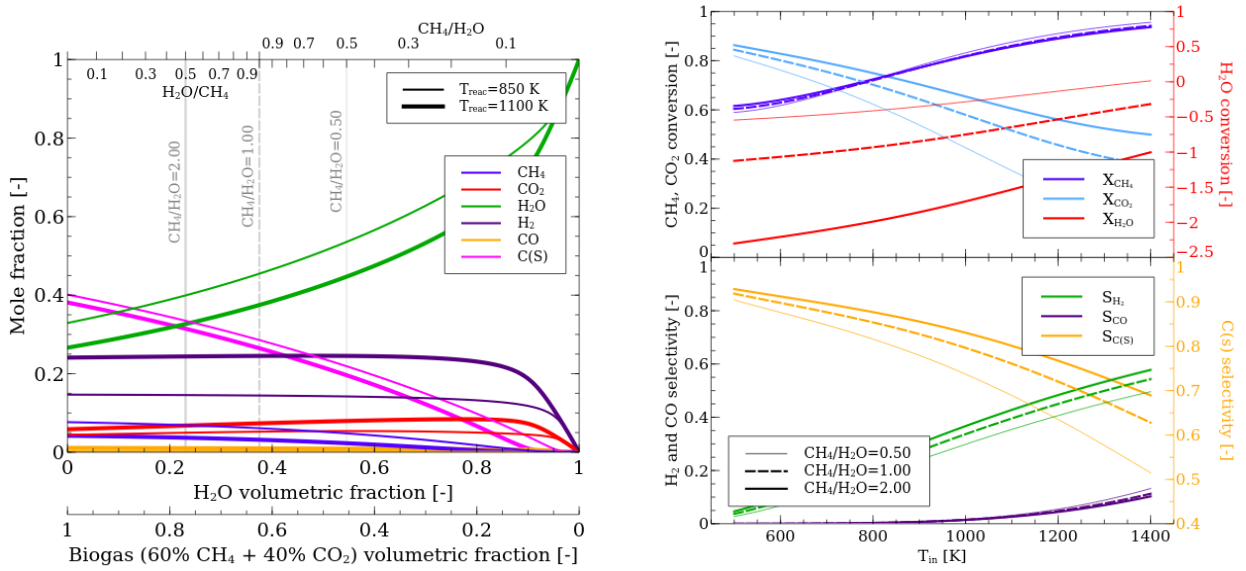

(a) (b)

Figure 31. Thermodynamic equilibrium calculations considering adiabatic and isobaric (1 atm) conditions: a) product composition as a function of the CH_4/H_2O ratio for two inlet temperatures; b) CH_4, CO_2 and H_2O conversions and H_2, CO and C(S) selectivities as a function of the inlet temperature for three CH_4/H_2O ratios.

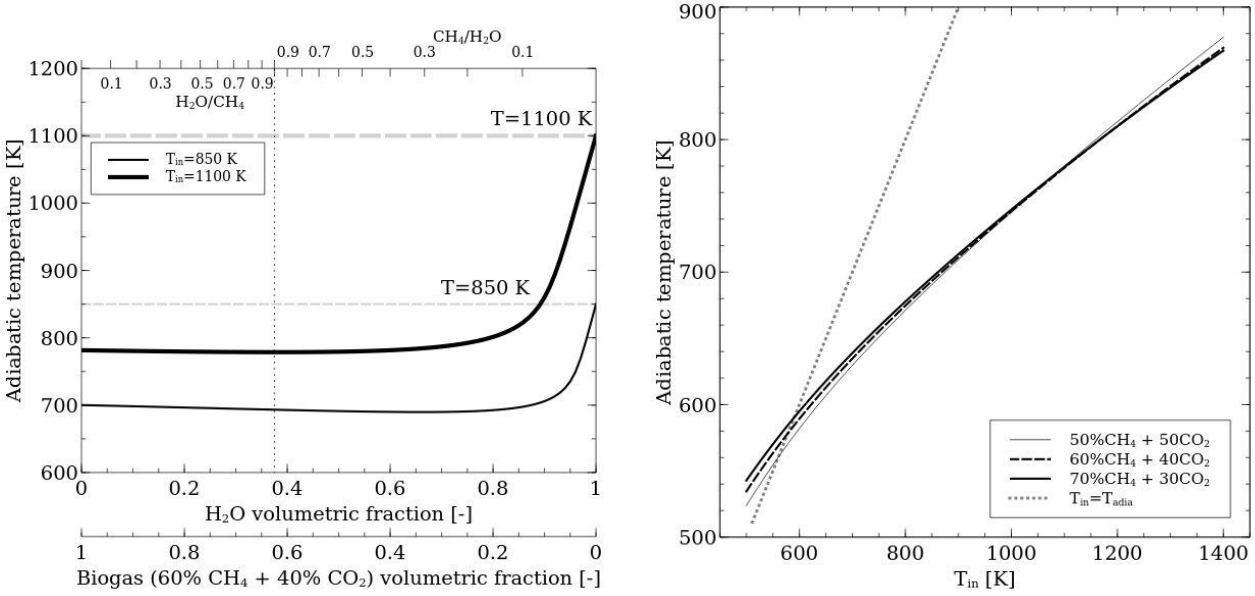

(a) (b)

Figure 32. Adiabatic temperature rise: as a function of CH_4/H_2O ratio for two inlet temperatures (a); as a function of the inlet temperature for three CH_4/H_2O mixture compositions (b).

In the following a literature survey on the specific topic of steam reforming of biogas is presented. Table 7 presents succinctly the main experimental work done so far focusing on the catalyst systems, the ratios CO_2 and H_2O to CH_4 and the main motivation along with the respective references.

Table 7. Literature survey on steam reforming of biogas (simultaneous steam and dry reforming of methane).

Metal	Support	Motivation	Mix. Conditions		Ref.
			CO_2/CH_4	H_2O/CH_4	
NiO	Unsupported	Catalyst activity and stability; carbon formation	0.05-0.71	0.39-1.72	57
NiO	MgO-SA-5205*	Catalyst activity and stability; fuel conversion; H_2/CO ratio; carbon formation	0.00-0.57	0.29-0.86	58
Ni	**$CaO-Al_2O_3$**	**Optimal operating temperature and H_2O/CH_4 ratio for downstream gas engine combustion**	**0.67**	**1.5-4.5**	**43**
NiO	Al_2O_3	Carbon formation; adequacy for downstream F-T synthesis	0.77	0.0-1.0	1
Ni	Al_2O_3	Comparison between the performance of a fixed- and fluidized-bed reactor; carbon deposition	0.67	0.56-5.56	42
Ru	**Al_2O_3**	**Optimal operational window; 1D pseudo-homogeneous model validation**	**0.40-2.00**	**2.0-6.0**	**41**
Ni	Not Available	Optimal reactor temperature, H_2O/CH_4 ratio and contact time/space velocity	0.67	1.52-4.69	53
Ni	**Not Available**	**Influence of H_2S presence in a clean model biogas on catalyst activity; catalyst regenerability**	**0.67**	**2.91;3.07**	**55**
Rh	Al_2O_3	1D model validation; minimization steam addition; reforming strategy adequacy for SOFC	0.54	1.11-3.33	54
Ni	Al_2O_3	Assessment of H_2 production in a fluidized-bed reactor followed by WGS reactor	0.67	0.83-5.00	56
Ni*	Not Available	Conversion of CH_4 and CO_2 formed from biomass gasification into synthesis gas; process optimization	0.50-2.00	1.00-3.00	59
NiO*	Al_2O_3	Effect of space velocity; integration of a biogas steam reforming unit in a reactor system for PEFC	0.67	1.80-2.87	60

Studies in bold are referred along the main text. *Commercial catalyst/catalyst carrier.

The effect of sulphur contaminants on the performance of a Ni-based catalyst under biogas steam reforming was studied by Ashrafi et al. [55]. They added to a synthetic biogas mixture different amounts of H_2S (15-145 ppm) and on a temperature range of 700-900 ºC measured the methane conversion. At a given temperature increasing the amount of H_2S in the feedstock decreases the time required to achieve a stable (however much lower) catalyst activity. Low operating temperatures (700 ºC), for a given H_2S partial pressure, induce higher damages in the catalyst activity than higher temperatures (900 ºC). Finally, they showed that the catalyst regeneration can be successfully achieved by increasing the reactor temperature.

Kolbitsch et al. [43] explored the applicability of a Ni-based catalyst supported on $CaO-Al_2O_3$ for steam reforming of a clean model biogas within a fixed bed reactor feed with constant flow rate. Based on experimental H_2 yield and CH4 conversion an operating temperature of 750 ºC was chosen for a H_2O to CH_4 ratio of 2.2. Through variation of the steam to methane ratio the authors observed a negligible kinetic role of CO_2 (for a high H_2O/CH_4 ratio) or a CH_4 reaction partner through methane dry reforming reaction (for a low H_2O/CH_4 ratio). During the experimental investigations the authors observed no catalyst deactivation and considered the catalyst performance adequate to produce reformate to be mixed with raw biogas in gas engines in order to improve its efficiency and decrease NOx emissions.

Regarding numerical efforts on biogas steam reforming, Avraam et al. [41] developed a 1D pseudo-homogeneous mathematical model and applied it to an isothermal Ru-based catalyst bed. To describe the surface chemical kinetics they considered the global reaction mechanism of Xu and Froment [91] composed by methane steam reforming to CO (R5) and CO_2 (R6) reactions and the water-gas shift reaction (R7). The external and internal mass transfer resistances as well as the mentioned adjustment on the kinetic parameters were indistinctly lumped to effectiveness factors obtained through an optimization procedure. At the end of the procedure, a good agreement between experimental and numerical predictions was observed over a wide range of operating conditions.

3.2.3 Autothermal reforming

Overview

Autothermal reforming (ATR) of methane or oxy-steam reforming of methane is the combination of the exothermic methane partial oxidation with the endothermic methane steam reforming reaction. The heat released provided by the exothermic partial and total oxidation reactions of methane will be captured by the endothermic reforming reactions in such a way that the overall reaction scheme can proceed in a thermoneutral ($\Delta H_R = 0$), exothermic ($\Delta H_R < 0$) or endothermic ($\Delta H_R > 0$) regime, according to the ratios $CH_4/H_2O/O_2$ [84]. The stoichiometric autothermal reforming reaction of methane with pure O_2 is expressed by the reaction R12. Depending on the ratio $O_2/0.5CH_4$ (denoted as x) the reaction R12 goes from the highly endothermic steam reforming reaction (x=0) to the mildly exothermic partial oxidation of methane (for x equal to 1). Concerning autothermal reforming operation x is somewhere between 0 and 1.

R12 $$CH_4 + \frac{x}{2}O_2 + (1-x)H_2O \rightarrow CO + (3-x)H_2 \qquad \Delta H_R^{\circ} = 206 - 242x\ kJ/mol$$

Besides the adjustment in the net heat release, controlling the feed ratios ($CH_4/H_2O/O_2$) also allows the regulation of the product H_2/CO ratio [84-85]. In particular, by increasing the O2/CH4 ratio an enhanced methane conversion is expected as well as an improvement of the catalyst stability due to carbon deposition [86-87]. However, a decrease of syngas selectivity is also predictable due to the thermodynamic promotion of methane total oxidation [86].

Ayabe et al [84] defined the following order of catalyst activity for methane autothermal reforming considering 2 wt.% metal loading (Co, Ni, Rh, Pd or Pt) on Al_2O_3 in a temperature range of 600-900 ºC and considering the feed flow rate as 16.7% CH_4, 1.7% O_2, 41.6% H_2O and 40% N_2:

Rh > Pd > Ni > Pt > Co

Concerning the influence of the support and its interaction with the metal catalyst (Ni) on the catalytic activity Ayabe et al. [84] under equal operating conditions also found that similar activities were achieved with 10 wt.% Ni/Al_2O_3 and 10 wt.% Ni/ZrO_2 but the activity shown by equal Ni content on SiO_2 was considerably lower than on Al_2O_3 and ZrO_2. Ni supported on metal oxides such as $CaO\text{-}CeO_2\text{-}ZrO_2$ in solid solutions also revealed a high activity for methane autothermal reforming [85]. For Pt supported catalysts during authothermal reforming of methane it was found that the support has an important role on the catalyst activity and stability. Particularly, Pt catalyst

supported on ZrO_2-Al_2O_3 showed better catalytic performance than Pt supported solely on Al_2O_3 or ZrO_2 [86].

Several modelling studies can be found in the literature concerning autothermal reforming of methane [88-90,94]. In the majority of these studies the chemical scheme is described by the global reactions of methane total oxidation (R9), steam reforming to CO (R5) and CO_2 (R6) and water-gas shift (R7) reactions. For methane total oxidation reaction the proposed kinetic expressions by Trimm and Lam [92] or Ma et al. [93] are generally considered whereas for the remaining reactions the rate expression from Xu and Froment [91] are regarded.

Biogas autothermal reforming

Autothermal reforming of biogas results from the simultaneous co-feeding of CH_4, CO_2, H_2O and O_2 into the reformer in which the CH_4/CO_2 ratio is a characteristic value of a biogas mixture. Therefore, the methane reforming reactions dry, steam and oxidative (partial oxidation) will exist in some extend in the reaction scheme. Because these three reactions contribute to the appearance of syngas in the autothermal reforming of biogas, this process is also known as tri-reforming of methane.

The same set of reactions that can explain the product composition of biogas catalytic partial oxidation can also explain the main reaction pathway in the case of biogas autothermal reforming.

Figure 33, 34, 35 and 36 present thermodynamic equilibrium values for CH_4 conversion and H_2, CO and C(S) selectivities, respectively. Three different values of temperature (600, 850 and 1100 K) were considered as well as a range for λ between 0.0 and 0.4, and for H_2O/CH_4 ratio from 0.0 to 0.8.

Regarding CH_4 conversion, Figure 33 shows for each temperature and for both cases (isothermal and adiabatic) that the H_2O/CH_4 ratio does not play an important role in opposition to λ. For 600 K the adiabatic case allows a higher methane conversion than the isothermal case practically for all range of H_2O/CH_4 ratio and λ. As the temperature increases the isothermal case only achieves better results than the adiabatic case for low λ values.

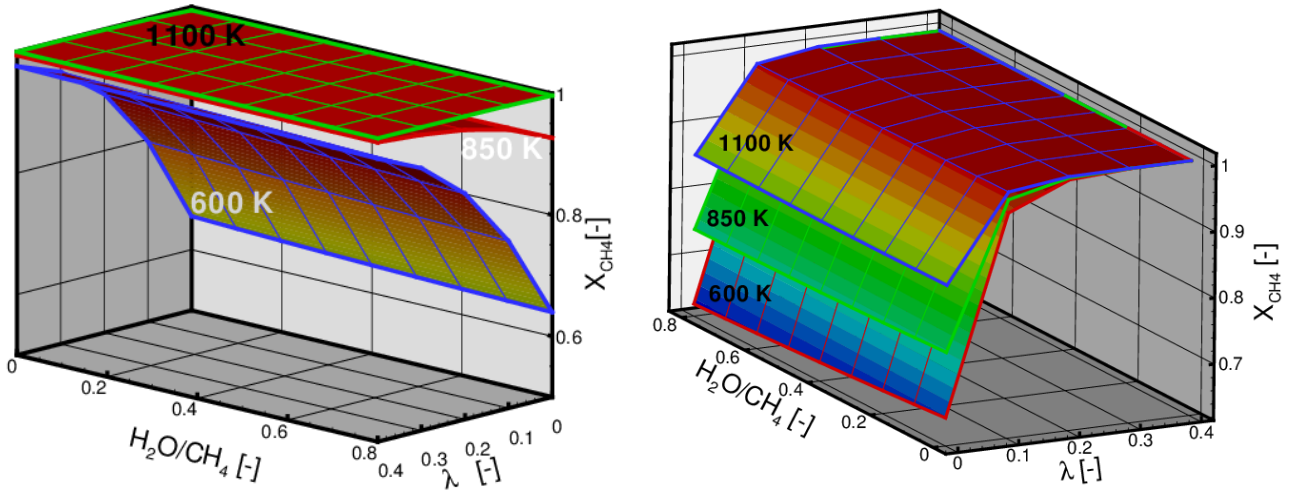

Figure 33. Thermodynamic equilibrium conversion of CH_4 as a function of the H_2O/CH_4 ratio and λ for three temperatures under isobaric (1 atm) and: a) isothermal conditions; b) adiabatic conditions.

Figure 34b shows that the equilibrium selectivity of H_2 at low temperatures (600 K) under adiabatic conditions is higher than the equilibrium H_2 selectivity under isothermal conditions (Figure 34a). For 850 K the isothermal case achieves higher values of H_2 selectivity than the adiabatic case only for low λ values (λ<0.1). However for 1100 K the H_2 selectivity at isothermal conditions is higher in almost all (H_2O/CH_4 ratio x λ) domain than that observed at adiabatic conditions.

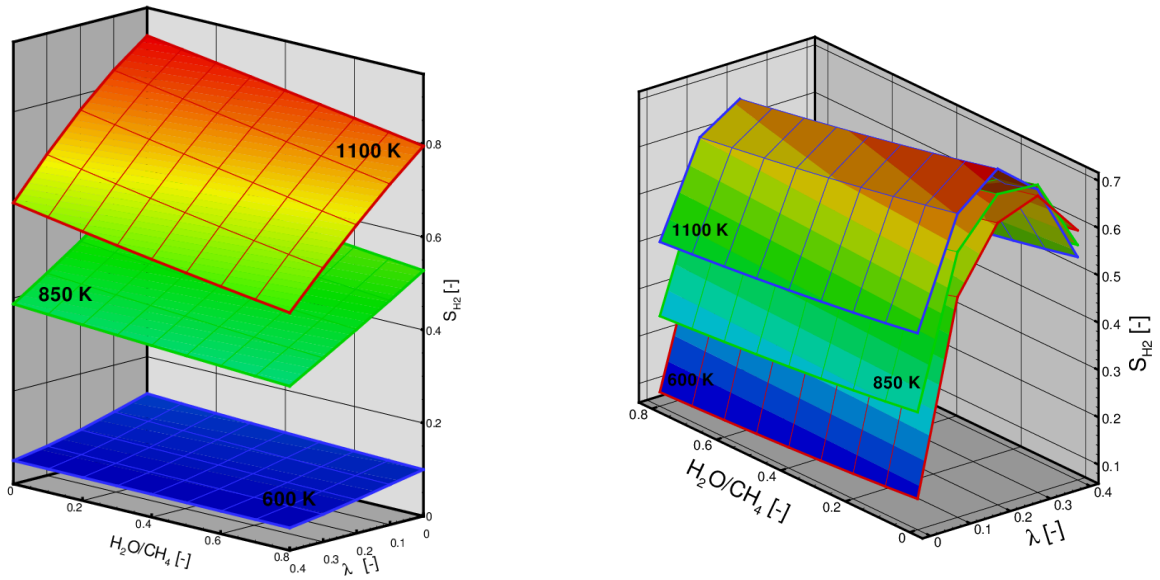

Figure 34. Thermodynamic equilibrium selectivity of H_2 as a function of the H_2O/CH_4 ratio and λ for three temperatures under isobaric (1 atm) and: a) isothermal conditions; b) adiabatic conditions.

Figure 35a shows that for low temperatures (600 and 850 K) under isothermal conditions the equilibrium values of CO selectivity do not depend noticeably on the H_2O/CH_4 ratio and on the λ value. The reactor temperature is the key parameter that determines the CO selectivity value. For high λ values the adiabatic operation returns higher CO selectivities than the isothermal operation for the three temperature values considered.

The selectivity to carbon formation reveals that as the temperature increases its value decreases for both operation modes (see Figure 36a and 36b). For low temperatures (600 K) the C(S) selectivity is generally higher under isothermal conditions than under adiabatic conditions. For high values of λ at 600 K the C(S) selectivity can be as low as 0.05 under adiabatic conditions comparing to 0.65 under isothermal conditions.

The thermodynamic equilibrium analysis for autothermal reforming of biogas under isothermal and adiabatic conditions revealed that the rector performance presents a high sensitivity on temperature and λ being rather insensitive to the H_2O/CH_4 ratio. At low to medium temperatures the adiabatic performance is by far more beneficial than the isothermal performance considering high λ values. This justifies the practical preference to operate autothermal reforming of biogas at adiabatic conditions.

Table 8 summarizes the available experimental studies in the open literature concerning biogas autothermal reforming. The first two works are devoted to methane tri-reforming and they do not refer explicitly to applications for biogas reforming. However their experimental data, concerning catalyst characterization, was performed under feed stream conditions similar to those encountered in studies of clean model biogas.

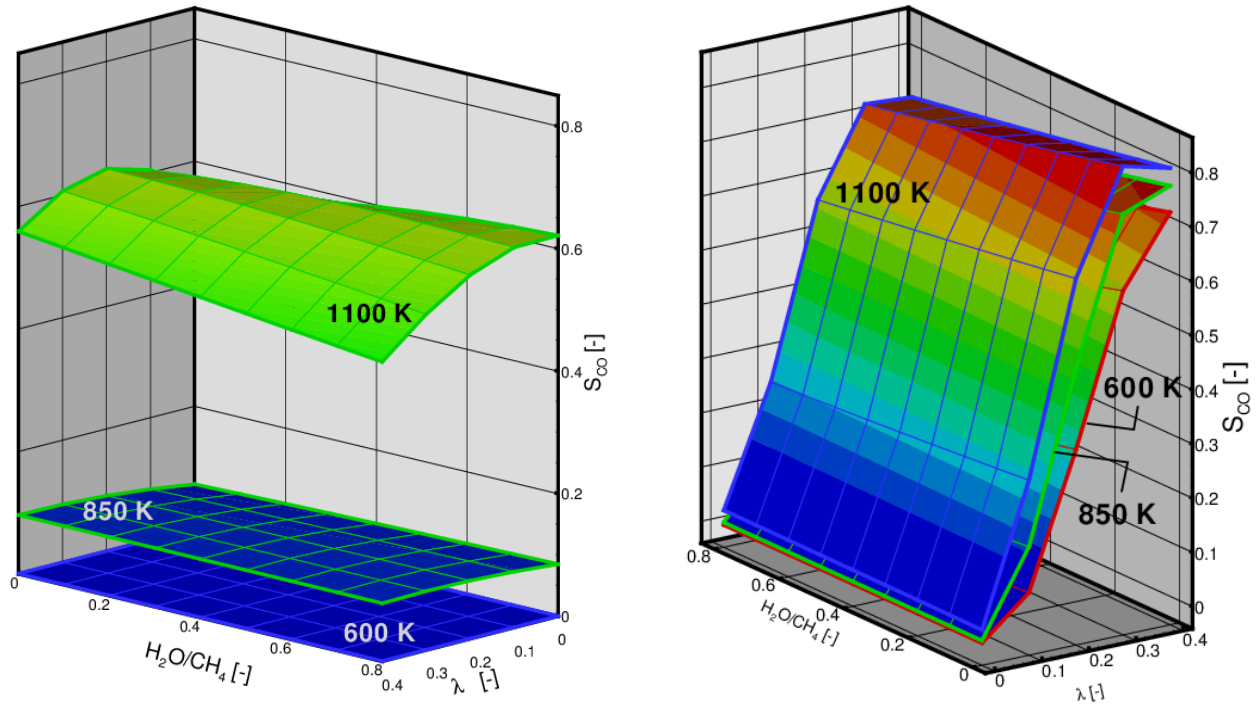

Figure 35. Thermodynamic equilibrium selectivity of CO as a function of the H_2O/CH_4 ratio and λ for three temperatures under isobaric (1 atm) and: a) isothermal conditions; b) adiabatic conditions.

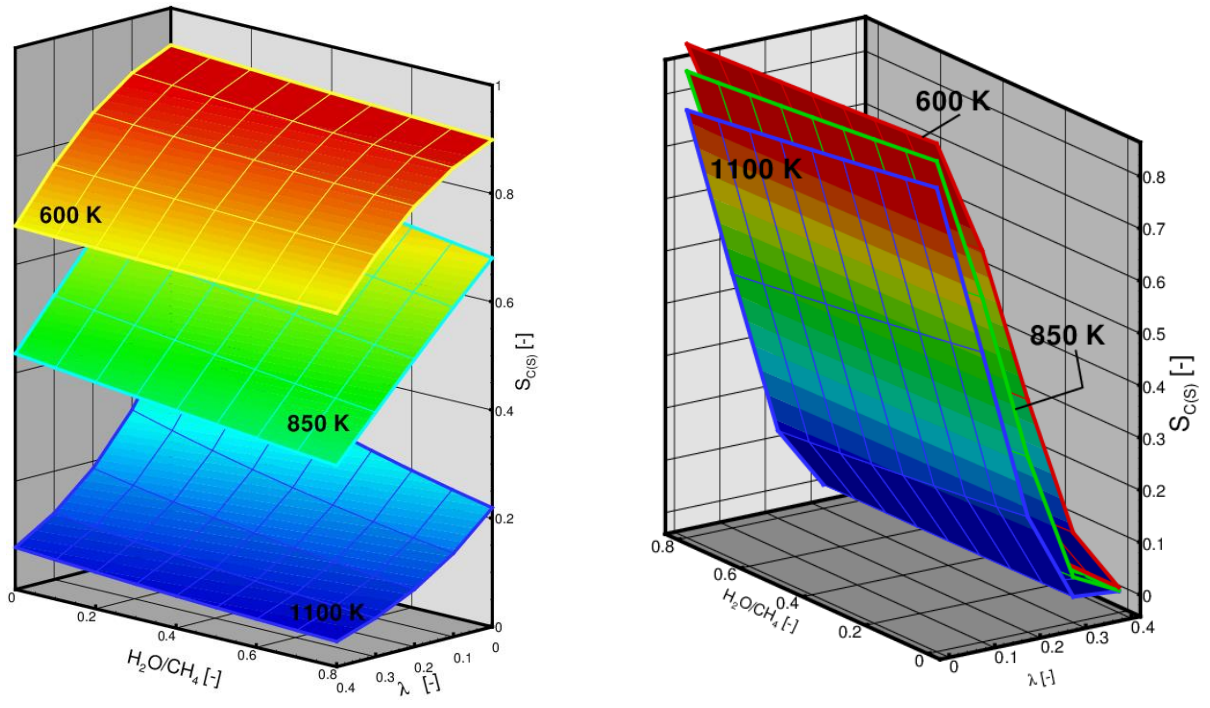

Figure 36. Thermodynamic equilibrium selectivity of C(S) as a function of the H_2O/CH_4 ratio and λ for three temperatures under isobaric (1 atm) and: a) isothermal conditions; b) adiabatic conditions.

The start-up procedure for autothermal reforming of biogas over Ni-based catalyst supported on cordierite honeycomb monolith was investigated by Araki et al. [96]. They found that catalyst

deactivation due to carbon deposition and Ni oxidation during the start-up regime could easily appear if inappropriate initial feed mixture composition and temperature is fed to the reactor. The durability of Ni-based catalyst deposited on cordierite honeycomb substrate was also assessed by Araki et al. [95]. They fed the catalytic reactor with an actual biogas mixture with trace amounts of impurities such as siloxanes, hydrogen sulphide and other organic compounds and with a variable methane concentration (35% - 65%). They found a stable catalytic performance during 250 h operation with a mean H_2O/CH_4 ratio of 1.86 and a mean λ value of 0.25. However, they alerted that a ratio H_2O/CH_4 more than 3.0 with a λ value of 0.25 led to a degradation of the catalytic activity due to the oxidation of Ni to Ni_2O_3.

Regarding applications, the simultaneous reforming of biogas and exhaust gas from a compression ignition engine to on-board produce H_2 rich gaseous streams was discussed by Lau et al [26,98]. The main goal behind this strategy is to improve combustion characteristics and reduce pollutant emissions by re-directing the H_2 rich stream produced to the combustion engine. In particular they investigated with realistic values for exhaust gas compositions the effect of λ and space velocity on thermal profiles along the catalyst monolith axial direction and on the integral product composition [98].

Concerning numerical investigations on the feasibility of biogas autothermal reforming, Xuan et al. [103] developed a two-dimensional pseudo-homogeneous mathematical model with global chemistry (as usual in methane autothermal computational studies). Their study was mainly motivated by the effects of operating conditions (inlet temperature, pressure, CO_2/CH_4, H_2O/CH_4 and λ) on the performance of the biogas autothermal reforming. The application of H_2 and O_2 membranes around the reforming zone was also assessed to enrich the H_2 stream derived and to reduce hot-spot formation, respectively.

Table 8. Literature survey on autothermal of biogas (tri-reforming of methane).

Metal	Support	Motivation	Mix. Conditions			Ref.
			CO_2/CH_4	H_2O/CH_4	λ	
Ni	MgO; MgO-CeZrO; CeO_2; ZrO_2; Al_2O_3; CeZrO	Catalyst performance; CO_2 and CH_4 conversion; carbon formation; kinetic study	0.27-0.81	0.21-0.75	0.05-0.17	101
Ni	MgO; TiO2; $Mg_xTi_{1-x}O$	CH_4 and CO_2 conversion; catalyst activity and stability	0.48	0.54	0.05	102
Ni	**Cordierite**	**Effect of H_2O/CH_4 ratio and λ on catalyst durability; utilization of actual biogas mixture**	**Variable**	**0-4**	**0.25;0.30**	**95**
Ni	**Cordierite**	**Start-up procedure: effect of O_2 and H_2O initial feed temperatures**	**0.67**	**2.0**	**0.25**	**96**
Ni	Cordierite	Effect of feed temperature, λ and H_2O/CH_4 ratio on hydrogen concentration and CH_4 conversion	1.04;0.93	0-3.10	0-0.33	97
Pt-Rh	**$Ce_{0.75}Zr_{0.25}O_2$ – Al_2O_3**	**Effect of λ and SV on integral mixture composition and thermal profiles**	**0.76-1.25**	**0.02-0.16**	**0.08-0.38**	**98**
Rh-Ni; Ni	MgO; (ZrO_2/CeO_2)-Al_2O_3; CeO_2-ZrO_2-Al_2O_3	Catalyst activity and selectivity; optimization experiments; comparison between fixed-bed and microreactors	0.67	1-3	0.13-0.25	99
Ni	SBA-15	Effect of steam addition, Ni content and SV; catalyst activity and stability	0.5	0-0.5	0.15	100

Studies in bold are referred along the main text.

3.3 Summary of biogas catalytic reforming strategies

The literature survey revealed that due to their advantages CPOx and autothermal reforming of biogas are the most appealing catalytic strategies to its conversion into synthesis gas for practical and sustainable applications. The bulk of the work on biogas steam reforming but mainly on biogas catalytic decomposition has been the development of catalysts capable of compete with the performance achieved in CPOx and ATR. Biogas catalytic decomposition and steam reforming also present a serious limitation related to their integration in compact and lightweight applications. This is due to the fact that an external heat supply system should be combined with the catalyst reactor.

Since the FC-District μ-CHP unit does not include neither a heat supply component to the reformer nor a steam generator, catalytic decomposition, steam reforming and autothermal reforming of biogas are not suitable as reforming technologies.
Therefore catalytic partial oxidation of biogas with air is the most suitable reforming strategy to be integrated in the FC-District μ-CHP system. From the thermodynamics standpoint, a proper selection of the air ratio and the inlet feed mixture temperature allow an operation with high selectivity towards synthesis gas and low concerns on catalyst stability namely due to carbon formation and catalyst deactivation.

4. Catalytic partial oxidation of biogas: applicability to the FC-District μ-CHP system

In this section an assessment of the applicability of biogas catalytic partial oxidation as the fuel processing thecnology to produce synthesis gas for the SOFC stack is carried out by computational means. A one-dimensional heterogeneous mathematical model was developed by IST to assist the development of the FC-District CPOx-based reformer. The mathematical model accounts with a multitude of transport phenomena and proper chemical kinetics for biogas reforming with air.
In the next two sections (4.1 and 4.2) the details of mathematical and numerical models are presented followed by the role of gas-phase reactions during biogas CPOx (section 4.3). Validation of the numerical model with experimental data gathered under relevant project conditions is presented in section 4.4. The chapter ends with a parametric study performed to determine optimal operating conditions.

4.1 Mathematical model

4.1.1 Governing equations

Numerical results herein presented were performed with a 1D heterogeneous mathematical model using the so-called single channel approach. Being heterogeneous the model is able to predict thermal and species profiles for gas and solid phases along the axial dimension of the reactor.

Gas phase balance equations

The species mass and energy balance equations of gas phase read as:

Mass balance equation

$$\varepsilon\rho_g\frac{\partial Y_{k,g}}{\partial t}+\varepsilon\rho_g u\frac{\partial Y_{k,g}}{\partial x}-\frac{\partial}{\partial x}\left(\varepsilon\rho_g D_{k,g}\frac{\partial Y_{k,g}}{\partial x}\right)+a_V\rho_g K_{mat,k}\left(Y_{k,g}-Y_{k,w}\right)-\varepsilon\dot{\omega}_{k,g}W_k=0 \quad (7)$$

Energy balance equation

$$\varepsilon\rho_g C_{p,g}\frac{\partial T_g}{\partial t}+\varepsilon\rho_g u C_{p,g}\frac{\partial T_g}{\partial x}-\frac{\partial}{\partial x}\left(\varepsilon K_g\frac{\partial T_g}{\partial x}\right)-\varepsilon\rho_g\sum_{k=1}^{KK_g}D_{k,g}C_{p,k}\frac{\partial Y_{k,g}}{\partial x}\frac{\partial T_g}{\partial x}+a_V h\left(T_g-T_s\right)+\varepsilon\sum_{k=1}^{KKg}\dot{\omega}_{k,g}H_{k,g}=0 \quad (8)$$

Thermal diffusion (Soret effect) is also included on molecular diffusion. The overall mass conservation is assured through the correction velocity formalism since the ordinary molecular diffusion coefficients are computed through the Hirschfelder's law [144]. The fourth term of the energy balance is included to ensure the coherence between mass and energy balances due to the distortion imposed on species profiles by molecular diffusion. Momentum balance was not considered in the model scheme since the pressure drop along the monolith length is typically negligible [71, 149].

Homogeneous gas phase reactions are commonly neglected during CPOx of light hydrocarbons at atmospheric pressure and typical CPOx conditions [145,154,153]. However, homogeneous side reactions start to gain importance on fuel conversion and syngas selectivity for higher hydrocarbons [147,148,155] or even for methane but at higher pressures (> 5 bar) [154,156-157].

Nevertheless the role of homogeneous reactions during biogas CPOx will be discussed in section 4.2.

The reactive flow behaves as an ideal gas mixture and consequently it obeys to the ideal gas equation given by expression (9).

$$\rho_g = \frac{PW_g}{RT_g} \tag{9}$$

Solid phase balance equations

The species mass and energy balance equations of solid phase read as:

Mass balance equation

$$\varepsilon_w \xi \rho_g \frac{dY_{k,w}}{dt} - a_V \rho_g K_{mat,k}\left(Y_{k,g} - Y_{k,w}\right) - \xi \dot{\omega}_{k,w} W_k = 0 \tag{10}$$

Energy balance equation

$$(1-\varepsilon)\rho_s C_{p,s} \frac{\partial T_s}{\partial t} - \frac{\partial}{\partial x}\left(K_{s,ef} \frac{\partial T_s}{\partial x}\right) - a_V h\left(T_g - T_s\right) + \xi \sum_{k=1}^{KK_w} \dot{\omega}_{k,w} H_k + a_V q''_{Rad} = 0 \tag{11}$$

Solid and gas phases are coupled in terms of mass and energy balances through interphase transport of mass and heat accounted for the second term of equation (10) and third term of equation (11), respectively. Species production/depletion rate appearing in both balance equations is given by expression (12) which already includes the importance of internal diffusive limitations along the washcoat layer.

$$\dot{\omega}_{k,w} = \sum_{R=1}^{N_R} \nu_{k,R} \cdot q_R \cdot \eta_R \cdot \rho_{cat.} \tag{12}$$

4.1.2 Chemical kinetics

Surface chemistry

The adopted surface chemistry scheme for catalytic partial oxidation of biogas follows the indirect kinetic mechanism of syngas production [67,150]. Table 9 presents the reaction mechanism and the rate equations for each reaction. Rate expressions for each reaction follow the Langmuir-Hinshelwood type.

Kinetic parameters for Arrhenius and Van't Hoff expressions are listed in Tables 10 and 11, respectively.

Table 9 – Reaction scheme and rate expressions for catalytic partial oxidation of biogas.

Reaction Stoichiometry	Rate expression (q_r)	Reaction ID
$CH_4 + 2O_2 \rightarrow CO_2 + 2H_2O$	$\frac{k_{CH_4,tot.ox.} P_{CH_4}}{1 + k_{ads,H_2O} P_{H_2O}} \sigma_{O_2}$	**R1**
$CH_4 + H_2O \rightleftarrows 3H_2 + CO$	$\frac{k_{CH_4,steam.ref.} P_{CH_4} (1 - \eta_{CH_4,steam.ref.})}{1 + k_{ads,CO} P_{CO} + k_{ads,O_2} P_{O_2}} \sigma_{H_2O}$	**R2**
$CO + H_2O \rightarrow CO_2 + H_2$	$\frac{k_{DWGS} P_{H_2O} (1 - \eta_{DWGS})}{(1 + k_{ads,H_2O} P_{H_2O})^2} \sigma_{CO}$	**R3**
$CO_2 + H_2 \rightarrow CO + H_2O$	$k_{RWGS} P_{CO_2} (1 - \eta_{RWGS}) \sigma_{H_2}$	**R4**
$H_2 + 1/2O_2 \rightarrow H_2O$	$k_{H_2,tot.ox.} P_{H_2} \sigma_{O_2}$	**R5**
$CO + 1/2O_2 \rightarrow CO_2$	$k_{CO,tot.ox.} P_{CO} \sigma_{O_2}$	**R6**

The σ_k term (expression (13)) is included in each rate expression to account for the depletion of the co-reactant species in each reaction.

$$\sigma_k = \frac{P_k}{P_k + 10^{-6}} \quad (13)$$

Table 10 – Kinetic parameters applied on Arrhenius expressions for each rate equation.

Reaction ID	A_{Ri} $[mol.g_{cat.}^{-1}.s^{-1}.a$	$E_{cat.Ri}$ $[kJ.mol^{-1}]$
R1	3.2889×10^4	92
R2	3.2794×10^4	92
R3	1.9536×10^0	25
R4	6.5345×10^1	62
R5	1.3509×10^7	62
R6	6.8284×10^5	76

Table 11 – Kinetic parameters applied on Van't Hoff expressions for each inhibiting species.

Species k	$A_{ads.k}$ $[atm^{-1}]$	$\Delta H_{ads.k}$ $[kJ.mol^{-1}]$
O_2	2.3431×10^{-4}	-73
H_2O	4.3045×10^{1}	-16
CO	1.2926×10^{0}	-37

Surface chemistry was evaluated with surface temperature (T_s) and mixture composition at the external interface between washcoat and the bulk gas flow ($[Y_{k,w}]$).

4.1.3 Transport phenomena

A strong coupling between transport and surface chemistry characterizes the overall performance of a catalytic reactor. Heat and mass external transport coefficients (h and $K_{mat,k}$) appearing in balance equations are evaluated through Nusselt and Sherwood correlations, respectively. Since the honeycomb monolith has square shaped channels, Nusselt correlation given by expression (14) has been widely applied in literature [158].

$$Nu = 2.977 + [8.827(1000\,X^*)^{-0.545}]\mathrm{Exp}(-48.2\,X^*) \tag{14}$$

Applying the Chilton-Colburn analogy, Sherwood number is given by expression (15) where the dimensionless distance on both correlations is evaluated through expression (16).

$$Sh = 2.977 + [8.827(1000\,X^*)^{-0.545}]\mathrm{Exp}(-48.2\,X^*) \tag{15}$$

$$X^* = \frac{x - x_{in}}{d_h Pe} \tag{16}$$

Diffusional limitations along the porous nature of the washcoat layer were considered through isothermal generalized effectiveness factors (expression (17)) computed with the generalized Thiele moduli given by expression (18), where the limiting species is denoted by k.

$$\eta_R = \frac{\tanh(\phi_{k,R})}{\phi_{k,R}} \tag{17}$$

$$\phi_{k,R} = \frac{\delta_{cat.} q_R(C_k^s)\rho_{cat.}}{\sqrt{2\int_{C_k^{eq}}^{C_k^s} D_{ef,k} q_R(C_k)\rho_{cat.} dC}} \tag{18}$$

Random pore model [159] was employed to evaluate effective diffusivities considering a typical bimodal pore structure [146] with both molecular and Knudsen diffusion contributions through the Bosanquet formula. Molecular diffusion coefficients, for each diffusive limiting species, were evaluated using the Fuller-Schettler-Giddings correlation [160].

Radiative heat losses from the glowing entrance of a catalytic monolith are expected in the absence of an inert heat shield located upstream the catalytic monolith. The inlet solid fraction of the catalytic monolith and the inner channel walls contribute to enlarge the radiative heat losses towards inlet manifold surfaces. Both sources of radiative heat losses were properly accounted for in the model scheme.

Radiative heat transfer in solid phase (fifth term of equation (11)), which also accounts for radiative heat losses near the boundaries of the catalytic monolith, was modeled through the Zone method [151] considering the gaseous mixture radiatively non participating due to the weak radiative contribution of combustion gases [152].

In the present study, the radiative enclosure is composed by a cylindrical channel and then surface zones are treated either as disk or ring shaped surfaces characterized by the hydraulic diameter of the channels of the honeycomb monolith. Expressions to compute shape factors between all types of surfaces (disk-disk, disk-ring and ring-ring) were derived based on the analytical solution of two parallel and coaxial disks [161] and exploiting reciprocity and summation laws. The inlet and outlet disk shaped surfaces of the enclosure represent both inlet and outlet manifolds and once the available space upstream and downstream the monolith section is relatively small a behavior different than black body is preferable for these surfaces [162-163]. Moreover, the exchange temperatures for inlet and outlet disks were kept equal to the inlet feed mixture temperature and outlet gas temperature, respectively.

After computing the direct exchange areas ($\overline{S_i S_j}$) between all pairs of surface zones (using shape factor expressions) a simple matrix manipulation [164] was then applied to obtain the total exchange areas ($\overline{S_i S_j}$) which, in a non-participating media, account for both direct radiation between surfaces as well as multiple reflections on surface zones.

Finally, having already computed total exchange areas, the net radiative heat flux for each surface zone, which appears in the energy balance of solid phase, is given by expression (19).

$$q''_{s_i} = \varepsilon_i \sigma T_{s_i}^4 - \frac{1}{A_{s_i}} \sigma \sum_{j=1}^{N_s} \overline{S_j S_i}\, T_{s_j}^4 \qquad (19)$$

4.1.4 Physical model

The catalytic reactor consists in a 600 cpsi honeycomb monolith without front and back shields to prevent heat losses by radiation. Figure 37 shows the computational domain employed for numerical activities. Tables 12 and 13 describe the geometrical properties of the monolith and its thermo-physical properties, respectively.

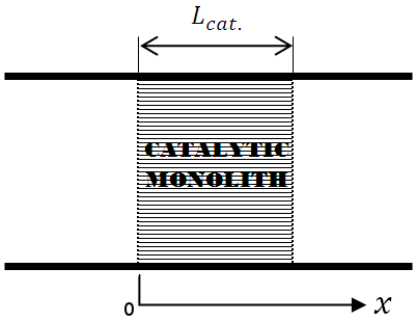

Figure 37. Schematic representation of the computational domains. $L_{cat.} = 2.0$ cm.

Table 12 – Geometrical properties of the honeycomb monolith catalyst after washcoat application.

Monolith diameter $[\mathrm{cm}]$	3.70
Monolith length $[\mathrm{cm}]$	2.00
Cell density $[\mathrm{cpsi}]$	600
Cell shape $[-]$	Square
Bed porosity $[\%]$	70.00
Specific surface area $[\mathrm{cm}^{-1}]$	32.27
Cell hydraulic diameter $[\mathrm{cm}]$	0.087
Washcoat thickness $[\mu\mathrm{m}]$	40.00

Table 13 – Thermo-physical properties of the honeycomb monolith catalyst.

Solid conductivity $[\mathrm{W.m^{-1}.K^{-1}}]$	3.00
Washcoat density $[\mathrm{kg.m^{-1}}]$	1.50
Surface emissivities $[-]$	
Inlet/Outlet manifold surfaces	0.15
Washcoat surfaces	0.45
Blank monolith ends	0.50

4.1.5 Boundary conditions

Danckwerts type of boundary conditions applied at the inlet section for gas phase equations (expressions (20) and (21)) should be always preferable, instead of the Dirichelt boundary conditions, in all kinds of situations (with or without a front heat shield) regarding the adopted dispersion mathematical model [165]. For the energy balance of solid phase a radiative boundary condition is always considered (expression (22)).
At catalyst's exit section zero-Neumann type of boundary condition expressions (23), (24) and (25)) is applied to all differential equations since all gradients become insignificant.

Inlet section

$$u\left(Y_{k,g}-Y_{k,in}\right)-D_{k,g}\frac{\partial Y_{k,g}}{\partial x}=0 \quad (20)$$

$$\rho_g u C_{p,g}\left(T_g-T_{g,in}\right)-k_g\frac{\partial T_g}{\partial x}=0 \quad (21)$$

$$k_s\frac{\partial T_s}{\partial x}-\sigma\varepsilon_s\left(T_s^4-T_{g,in}^4\right)=0 \quad (22)$$

Outlet section

$$\frac{\partial Y_{k,g}}{\partial x}=0 \quad (23)$$

$$\frac{\partial T_g}{\partial x}=0 \quad (24)$$

$$\frac{\partial T_s}{\partial x}=0 \quad (25)$$

4.2 Numerical model

The present mathematical model was implemented in an in-house version of PREMIX code [166] from CHEMKIN family combustion codes. To reduce the boundary value problem to a system of non-linear algebraic equations finite difference approximations are employed. Then on a non-uniform coarse initial mesh the program attempts to solve the problem through a damped Newton's method. An adaptive mesh procedure based on gradient and curvature resolutions between gridpoints is always applied to reach finer meshes after a converged solution on a previous mesh is attained. If the solution lies out of the steady-state domain of convergence a time-stepping procedure is also applied to bring the solution into steady-state domain of convergence of Newton's method.
All thermodynamic and transport data were evaluated using CHEMKIN correlations [167-168] with thermodynamic and transport coefficients given by GRI-Mech 3.0 database [169].

4.3 Importance of gas-phase reactions

The role of homogeneous reactions during biogas CPOx on the overall reactants conversion is analysed with two elementary reaction mechanisms that were incorporated into the numerical model: GRI-Mech 3.0 [169] and the detailed kinetic scheme proposed by Ranzi and co-workers [170].
An inlet feed temperature of 400 ºC, an air ratio of 0.29, a fuel volumetric flow rate equal to 4 NL/min under atmospheric pressure conditions were considered as well as synthetic biogas mixture with a CH_4/CO_2 ratio of 1.5. Figure 38a presents the gas and solid thermal profiles as well as molar fractions of gas phase species with and without the application of homogeneous reactions.

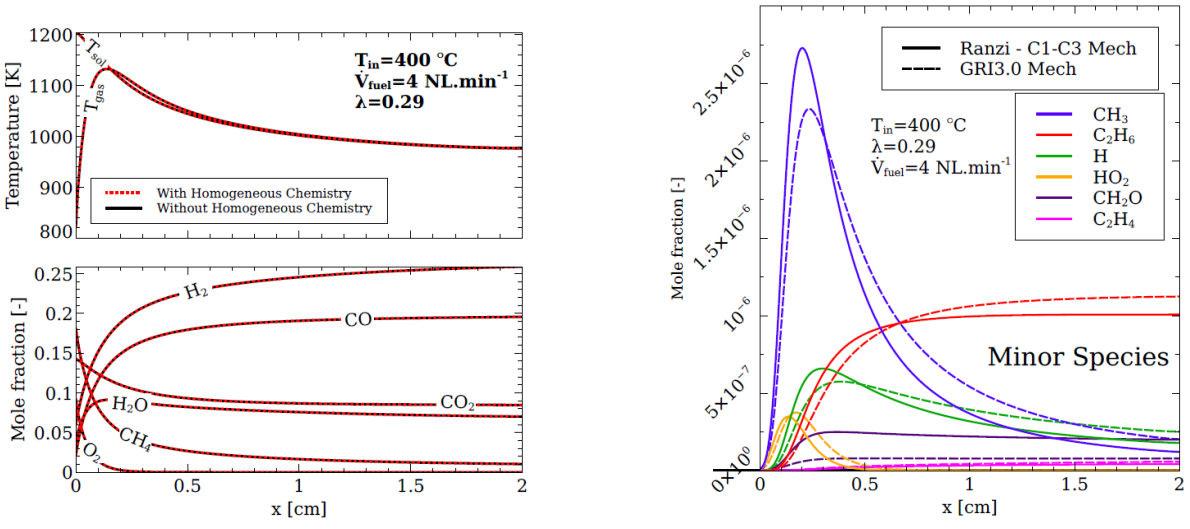

(a) (b)

Figure 38. Importance of homogeneous chemistry: (a) comparison of thermal profiles and product distribution computed with and without gas phase chemistry (GRI3.0-Mech); (b) minor gas phase species.

In particular, results on Figure 38a were evaluated with GRI3.0-Mech but employing the mechanism suggested by Ranzi a practical similar result is observed (not shown). No apparent

difference in temperatures and product distribution between the numerical results with and without homogeneous chemistry is observed. The homogeneous reaction pathway is significantly lower than the kinetic role of the catalyst to convert the reacting feed mixture. Figure 38b shows the minor species of the bulk gas phase computed with both reaction mechanisms.
Figure 39 presents the methane consumption rate by the two chemical routes. It is observed that the homogeneous conversion of methane is about five orders of magnitude lower than the conversion of methane through surface reactions.

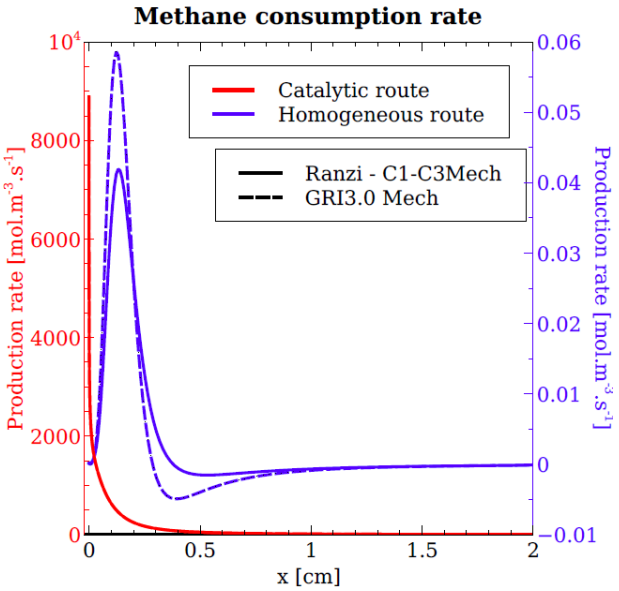

Figure 39. Contribution of gas phase and surface reactions on the conversion of methane.

From this brief analysis one reaches to the conclusion that homogeneous side reactions are insignificant in the overall reaction pathway. For this reason the numerical results that follow were evaluated without considering gas phase reactions for the sake of fast numerical computations.

4.4 Model Validation

The experimental characterization of the FC-District reactor performance under biogas CPOx operation was performed by TUBAF. A clean model biogas with a CH_4/CO_2 ratio of 1.5 was considered as well as an extensive range for air ratios (0.19-0.34), inlet feed temperatures (400-450 ºC) and flow rates (5-14 NL/min). The experimental data required for model validation, namely the integral reactor product distribution was reported in the deliverable D3.1.4.
Figure 19 and 20 present the numerical and experimental results for thermal profiles and product mixture composition at the outlet catalyst section. In particular, Figures 19a and 19b show the system performance to variations in the air ratio value. Following the experimental data, an increase on the value of the air ratio is responsible for a general increase in the temperatures along the catalyst bed, an increase in the molar fraction of total oxidation species (H_2O and H_2) and a decrease of partial oxidation species (H_2 and CO). Such experimental trends are very well predicted by the model, not only in a qualitative way but mainly in a quantitative manner. The trends observed on thermal and species profiles with an increase on the air ratio are generally related to a progressive shift from partial to total methane oxidation.
Figure 20a and 20b presents the reactor response for different fuel flow rates. Regarding the thermal behaviour higher temperatures were experimentally measured and predicted by the model

for higher fuel flow rate values. Also observable as the fuel flow rate increases is the dislocation of the maximum gas temperature towards the outlet reactor section. The product distribution is almost insensitive to variations on the feed flow rate but from the theoretical standpoint a decrease in fuel conversion and syngas selectivity are somewhat expected due to a decrease in the residence time.

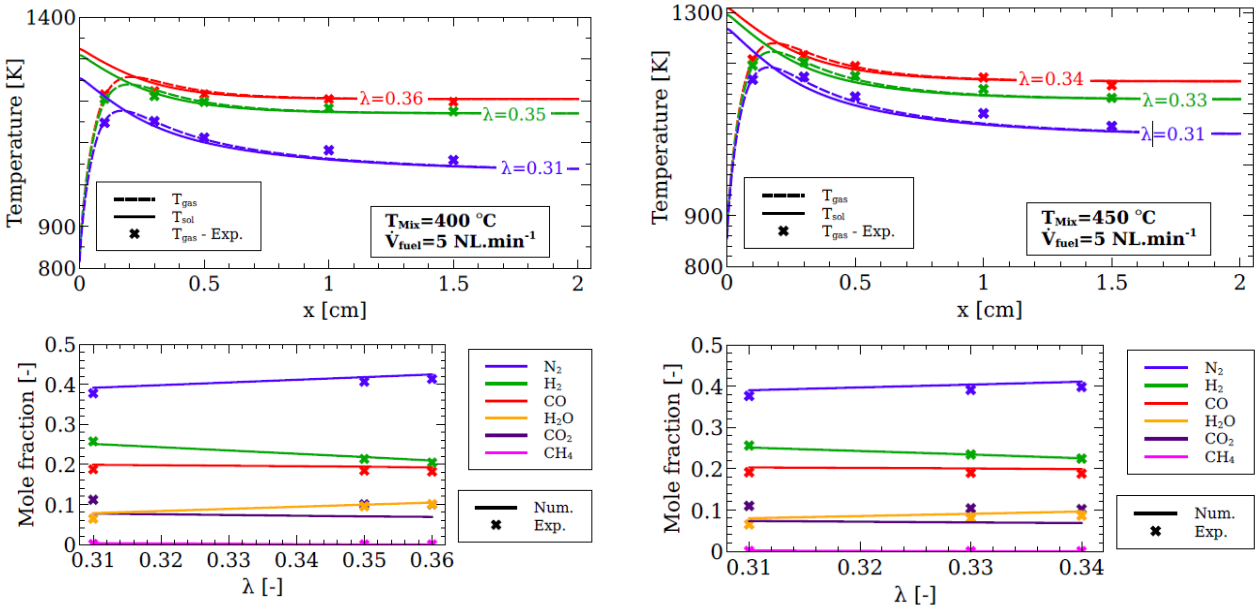

(a) (b)

Figure 19. Numerical and experimental results for temperature and integral product distribution at different air ratio values: (a) $\mathrm{T_{mix}} = 400$ °C and $\dot{\mathrm{V}}_{\mathrm{fuel}} = 5\ \mathrm{NL.\,min^{-1}}$; (b) $\mathrm{T_{mix}} = 450$ °C and $\dot{\mathrm{V}}_{\mathrm{fuel}} = 5\ \mathrm{NL.\,min^{-1}}$.

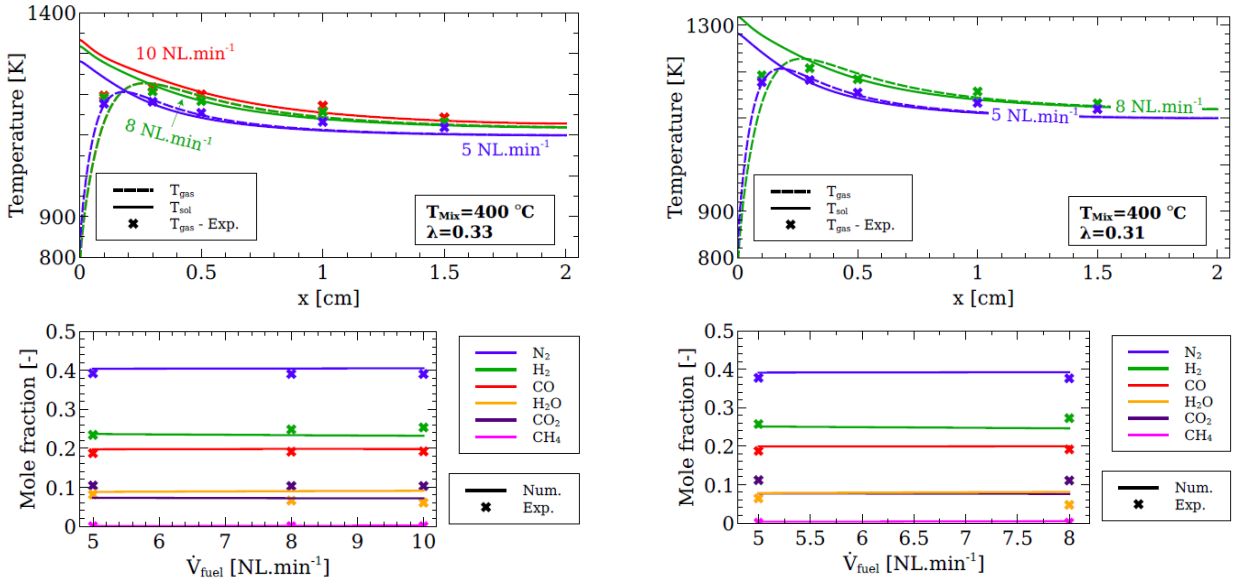

(a) (b)

Figure 20. Numerical and experimental results for temperature and integral product distribution at different fuel flow rates: (a) $T_{mix} = 400$ °C and $\lambda = 0.33$; (b) $T_{mix} = 400$ °C and $\lambda = 0.31$.

A general good agreement between experimental data and numerical results is observed.

4.5 Parametric study

A parametric study was conducted with the numerical model presented to achieve an optimal operating regime for biogas reforming through CPOx with air. It was considered a reformer inlet feed mixture temperature of 400 ºC, a range for λ between 0.23 and 0.35 and a range for the fuel flow rate from 5 to 13 NL/min. A pure CH_4-CO_2 mixture with a CH_4/CO_2 ratio equal to 1.5 was considered.

Figure 21a presents the CH_4 conversion as a function of the air ratio and the fuel flow rate. A slight decrease of CH_4 conversion is detected as the fuel flow rate increases. An evident increasing trend of CH_4 conversion is noticed varying the air ratio value. An almost complete (>99%) consumption of CH_4 is observed at the highest air ratio value (λ=0.35) independently of the fuel flow rate. The computed tendency of the methane conversion with the air ratio follows the thermodynamic equilibrium results. The maximum value of CH4 conversion (99.97%) is registered at λ=0.35 for the lowest flow rate considered (5 NL/min).

Figure 21b presents the integral reforming efficiency computed through expression (1). A small but noteworthy decrease in the reforming efficiency is observed as the fuel flow rate increases. Increasing the air ratio the reforming efficiency increases expressively until a maximum is attained between 0.31 and 0.33 depending on the fuel flow rate. In the whole range of air ratio and fuel flow rate the maximum reforming efficiency (90.11%) is observed at 0.31 and 5 NL/min.

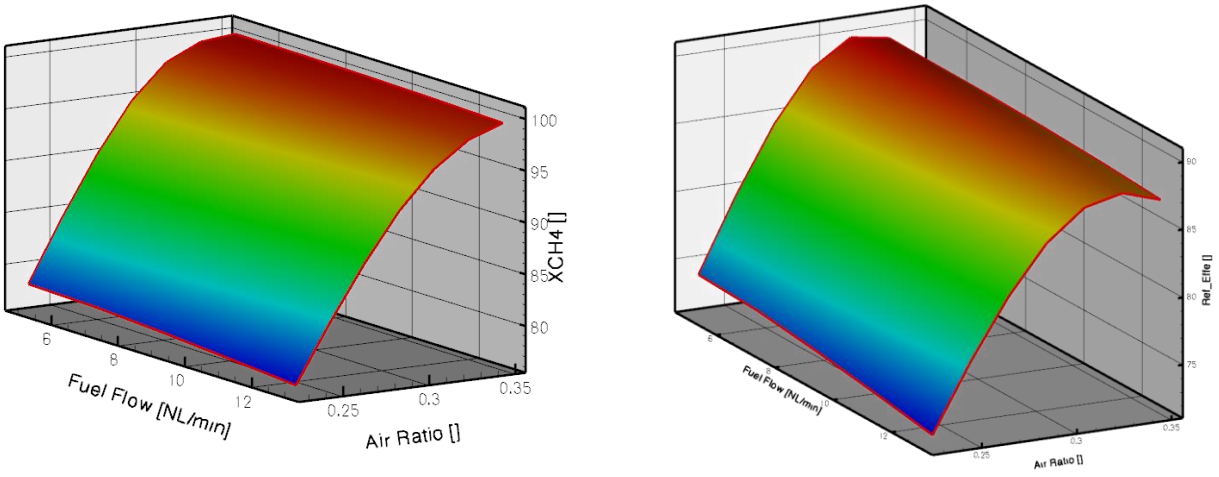

(a) (b)

Figure 21. CH_4 conversion (a) and integral reforming efficiency (b) predicted by the numerical model for an inlet gas temperature of 400 ºC.

The H_2 and CO selectivities are shown in Figures 22a and 22b. Regarding the selectivity of H_2 a decreasing tendency is observed as the air ratio is increased and a slight decrease is noticed for higher fuel flow rates. The maximum value for H_2 selectivity (80.45%) is registered in the minimum value for air ratio (0.23) and fuel flow rate (5 NL/min). The CO selectivity, on the contrary increases as the air ratio is increased and as a smooth maximum between 8-10 NL/min. The maximum value for CO selectivity (74.01%) is remarked at 0.35 and 9 NL/min.

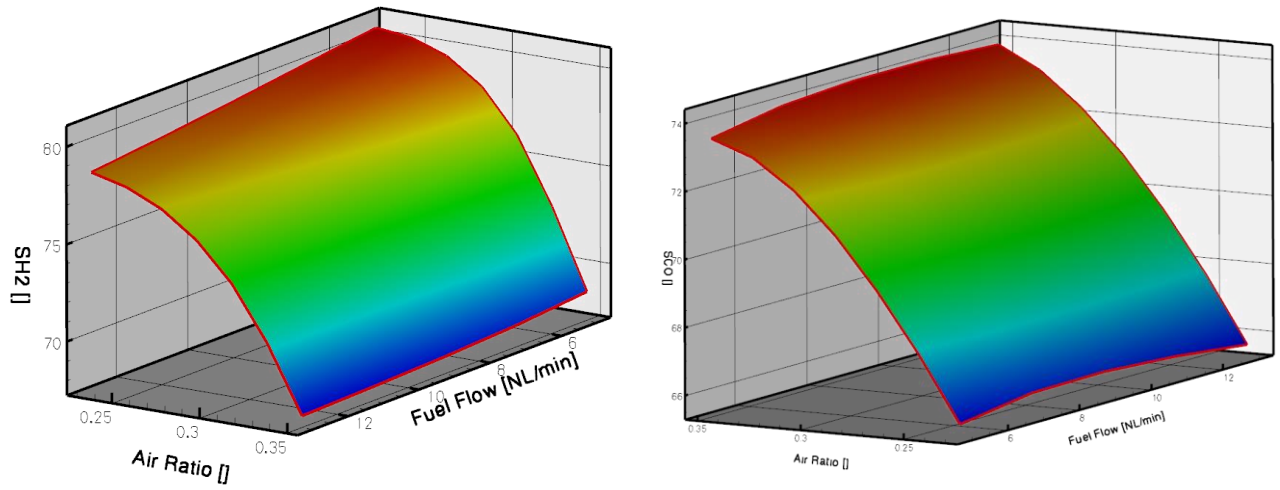

(a) (b)

Figure 22. H_2 (a) and CO (b) selectivity predicted by the numerical model for an inlet gas temperature of 400 ºC.

The temperature distribution and the presence of hot-spots along the catalyst bed is an issue that deserves a special attention. It is widely recognized that high temperatures (say above 1000 ºC) can trigger thermal changes in the catalyst support structure (phase transformations) and a decrease in the metal dispersion. These two effects, commonly known as thermal sintering, ultimately lead to a decrease in the active metal surface area and then to a decrease of the catalyst intrinsic activity.

Figure 23a shows the maximum predicted catalyst surface temperature. Although not shown, the maximum surface temperature in a fresh catalyst sample is located very near the inlet section of the catalyst (see Figures 19, 20). The maximum surface temperature markedly increases with both air ratio and fuel flow rate. The maximum value which was registered in the limit of the air ratio and fuel flow rate ranges was 1404 K. A prolonged exposure of the catalyst to such aggressive thermal environments can lead to its rapid deactivation.

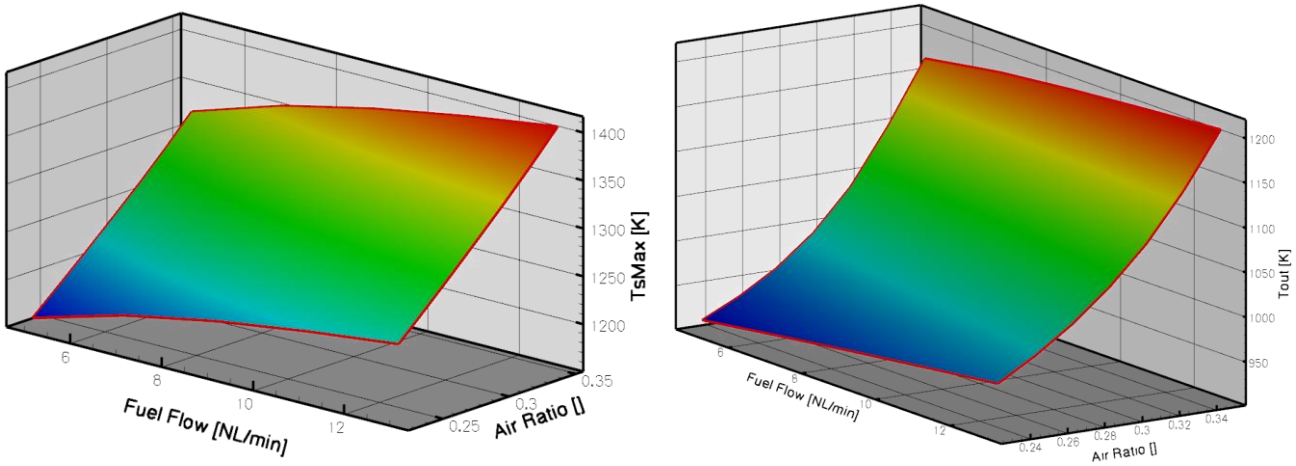

(a) (b)

Figure 23. Maximum catalyst surface temperature (a) and outlet gas temperature (b) predicted by the numerical model for an inlet gas temperature of 400 ºC.

The outlet gas temperature is presented in Figure 23b and shows a similar behaviour with the air ratio and fuel flow rate as the maximum surface temperature.

For a long term catalyst operation without loss of catalyst performance a maximum surface temperature is recommended. Due to the catalyst composition and morphology such temperature limit is herein chosen as 1000 ºC. Figure 24 shows the range of air ratios and fuel flow rates that guarantee a maximum catalyst surface temperature below 1000 ºC (region denoted as “stable operating regime”) and higher temperatures (“deactivation regime”).

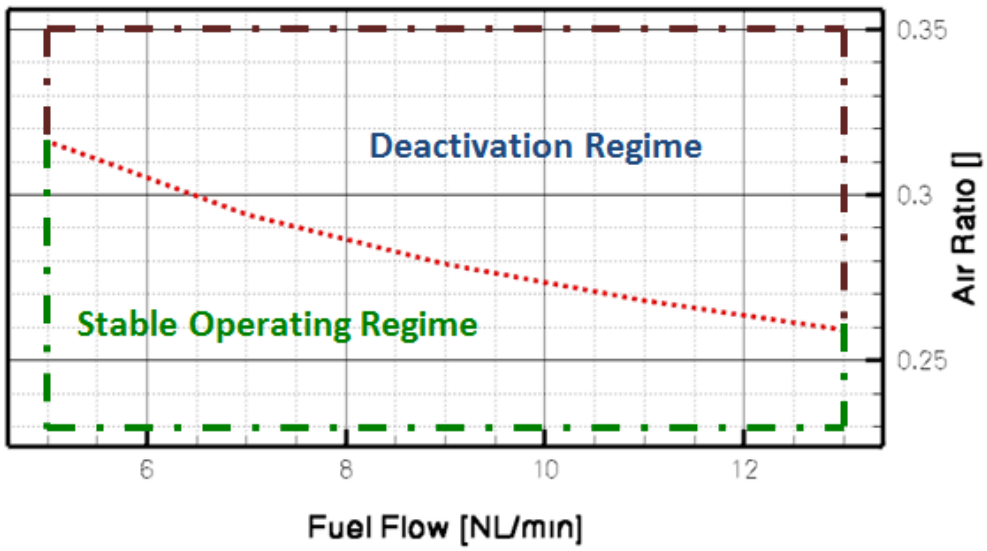

Figure 24. Range of operating conditions that assure a stable operating regime, far from thermal deactivation concerns, for an inlet gas temperature of 400 ºC.

Figure 25 presents the pressure drop in the whole catalyst bed. Since the momentum equation was not incorporated in the model the pressure drop was computed in a post-processing stage with the interstitial velocity and viscosity fields along the whole monolith through the correlation shown in expression (26).

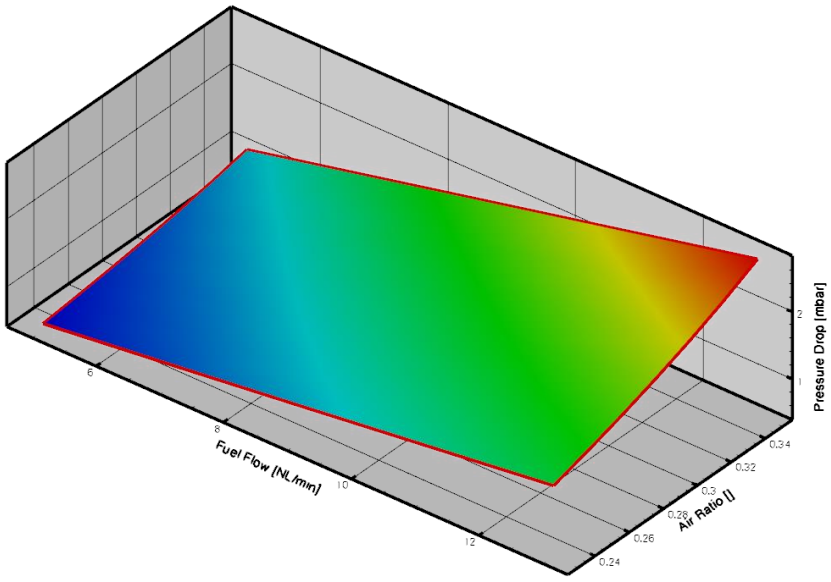

Figure 25. Pressure drop in the catalyst monolith for an inlet gas temperature of 400 ºC.

$$\Delta P = 32.\frac{L_{cat.}}{Re.d_h}\rho.u^2 \quad (26)$$

Figure 25 shows the pressure drop increasing with both the air ratio and the fuel flow rate. The lowest pressure drop value (0.52 mbar) is observed at the lowest values of air ratio (0.23) and fuel flow rate (5 NL/min). A maximum value of 2.72 mbar is registered for the most severe operating condition (0.35 and 13 NL/min).

Disregarding the downstream requirements of the fuel cell stack the most profitable operating condition for synthetic biogas CPOx at atmospheric pressure and $T_{mix} = 400\,℃$ is defined by $\lambda = 0.31$ and $\dot{V}_{fuel} = 5\,NL/min$. These values were chosen within the “stable operating regime” (see Figure 24) as those which return a higher reforming performance.

5. Conclusions

The present document focuses on conventional non-catalytic and catalytic reforming strategies applicable for biogas.

The utilization of biogas in the FC-District μ-CHP unit requires a cleaning procedure of biogas to avoid corrosion of the fuel processing components and catalyst deactivation issues.

Thermal partial oxidation reforming requires higher operation temperatures than catalytic partial oxidation reforming which imply a higher energy cost. Moreover, the high temperature values along the manifolds can lead to kinetically controlled undesirable effects decreasing the overall system efficiency.

Among the four catalytic reforming strategies, the catalytic partial oxidation and autothermal reforming of biogas are the most appealing catalytic strategies to biogas conversion into synthesis gas for practical and sustainable applications. However, due to the high endothermicity of catalytic decomposition and steam reforming of biogas the requirement of external heat supply is mandatory which increases the overall energy demand.

Since the FC-District μ-CHP unit does not include neither a heat supply component to the reformer nor a steam generator, catalytic decomposition, steam reforming and autothermal reforming of biogas are not suitable. Therefore catalytic partial oxidation of biogas with air is the most suitable reforming strategy to be integrated in the FC-District μ-CHP system.

The models embodied in numerical calculations presented in this report combined with the experimental validation allow the proper selection of operating conditions that yield high selectivity towards synthesis gas and low concerns on catalyst stability namely due to carbon formation and catalyst deactivation.

Acknowledgments

The FC-DISTRICT Consortium would like to acknowledge the financial support of the European Commission under the Seventh Framework Program.

References

[1] Nazim Muradov and Franklyn Smith. Thermocatalytic conversion of landfill gas and biogas to alternative transportation fuels. Energy & Fuels. 22:2053-2060. 2008.

[2] Nazim Muradov, Franklyn Smith and Ali T-Raissi. Hydrogen production by catalytic processing of renewable methane-rich gases. International Journal of Hydrogen Energy. 33:2023-2035. 2008.

[3] Franz Fischer and Hans Tropsch. Conversion of methane into hydrogen and carbon monoxide. Brennstoff-Chemie. 3:39–46. 1928.

[4] Shaobin Wang, G. Q. (Max) Lu and Graeme J. Millar. Carbon dioxide reforming of methane to produce synthesis gas over metal-supported catalysts: state of the art. Energy & Fuels. 10:896-904. 1996.

[5] Nazim Z. Muradov. Production of hydrogen from hydrocarbons (chap. 2). Hydrogen fuel: production, transport and storage. Ram B. Gupta (Ed.). 2009, CRC Press.

[6] M. C. J. Bradford and M. A. Vannice. CO_2 reforming of CH_4. Catalysis Reviews. 41:1-42. 1999.

[7] Jianjun Guo, Hui Lou, Hong Zhao, Dingfeng Chai, Xiaoming Zheng. Dry reforming of methane over nickel catalysts supported on magnesium aluminate spinels. Applied Catalysis A: General. 273:75-82.2004.

[8] David L. Trimm. The formation and removal of coke from Nickel catalyst. Catalysis Reviews: Science and Engineering. 16:155-189. 1977.

[9] Mun-Sing Fan, Ahmad Zuhairi Abdullah, and Subhash Bhatia. Catalytic Technology for Carbon Dioxide Reforming of Methane to Synthesis Gas. ChemCatChem. 1:192-208. 2009.

[10] E. Turpeinen, R. Raudaskoski, E. Pongrácz and R. L. Keiski. Thermodynamic analysis of conversion of alternative hydrocarbon-based feedstocks to hydrogen. International Journal of Hydrogen Energy. 33:6635-6643. 2008.

[11] S.H. Chan and W. M. Wang. Effect of natural gas composition on autothermal fuel reforming products. Fuel Processing Technology. 64:221-239. 2000.

[12] Chung K. Law. Combustion physics. Cambridge University Press. 2006.

[13] D.G. Goodwin, An open-source, extensible software suite for CVD process simulation, in Electrochemical Society. 155-162. 2003.

[14] Yun Hang Hu and Eli Ruckenstein. Catalytic conversion of methane to synthesis gas by partial oxidation and CO_2 reforming. Advances in Catalysis. 48:297-345. 2004.

[15] J. H. Edwards and A. M. Maitra. The chemistry of methane reforming with carbon dioxide and its current potential applications. Fuel Processing Technology. 42:269-289. 1995.

[16] C. Crisafulli, S. Scirè, R. Maggiore, S. Minicò and S. Galvagno. CO_2 reforming of methane over Ni-Ru and Ni-Pd bimetallic catalysts. Catalysis Letters. 59:21-26. 1999.

[17] J. R. Rostrup-Nielsen and J. H. Bak Hansen. CO_2-reforming of methane over transition metals. Journal of Catalysis. 144:38-49. 1993.

[18] A. T. Ashcroft, A. K. Cheetham, M. L. H. Green, P. D. F. Vernon. Partial oxidation of methane to synthesis gas using carbon dioxide. Nature. 352:225-226. 1991.

[19] J. H. Bitter and K. Seshan and J. A. Lercher. Deactivation and coke accumulation during CO_2/CH_4 reforming over Pt catalysts. Journal of Catalysis. 183:336-343. 1999.

[20] Jianguo Zhang, Hui Wang and Ajay K. Dalai. Development of stable bimetallic catalysts for carbon dioxide reforming of methane. Journal of Catalysis. 249:300-310. 2007.

[21] Keiichi Tomishige, Yang-guang Chen and Kaoru Fujimoto. Studies on carbon deposition in CO_2 reforming of CH_4 over Nickel-Magnesia solid solution catalysts. Journal of Catalysis. 181:91-103.1999.

[22] Bernd Steinhauer, Mohan Reddy Kasireddy, Jörg Radnik and Andreas Martin. Development of Ni-Pd bimetallic catalysts for the utilization of carbon dioxide and methane by dry reforming. Applied Catalysis A: General. 366:333-341. 2009.

[23] J. Juan-Juan, M. C. Román-Martinéz and M. J. Illán-Gómez. Effect of potassium content in the activity of K-promoted Ni/Al_2O_3 catalysts for the dry reforming of methane. Applied Catalysis A: General. 301:9-15. 2006.

[24] Chuan Shi, Anjie Zhang, Xiaosong Li, Shaohua Zhang, Aimin Zhu, Yufei Ma, Chaktong Au. Ni-modified Mo_2C catalysts for dry reforming. Applied Catalysis A: General. 431-432:164-170. 2012.

[25] McKenzie P. Kohn, Marco J. Castaldi, Robert J. Farrauto. Auto-thermal and dry reforming of landfill gas over a $Rh/\gamma Al_2O_3$ monolith catalyst. Applied Catalysis B: Environmental. 94:125-133. 2010.

[26] C. S. Lau, A. Tsolakis and M. L. Wyszynski. Biogas upgrade to syngas (H_2-CO) via dry and oxidative reforming. International Journal of Hydrogen Energy. 36:397-404. 2011.

[27] Federico Barrai, Tracy Jackson, Noah Whitmore, Marco J. Castaldi. The role of carbon deposition on precious metal catalyst activity during dry reforming of biogas. Catalysis Today. 129:391-396. 2007.

[28] Petar Djinovíc, Ilja Gasan Osojnik Črnivec, Jurka Batista, Janez Levec and Albin Pintar. Catalytic syngas production from greenhouse gasses: performance comparison of $Ru-Al_2O_3$ and $Rh-CeO_2$ catalysts. Chemical Engineering and Processing. 50:1054-1062. 2011.

[29] O. A. Bereketidou and M. A. Goula. Biogas reforming for syngas production over nickel supported on ceria-alumina catalysts. Catalysis Today. 195:93-100. 2012.

[30] Junke Xu, Wei Zhou, Zhaojing Li, Jihui Wang, Jianxin Ma. Biogas reforming for hydrogen production over a Ni-Co bimetallic catalyst: effect of operating conditions. International Journal of Hydrogen Energy. 35:13013-13020. 2010.

[31] Junke Xu, Wei Zhou, Zhaojing Li, Jihui Wang, Jianxin Ma. Biogas reforming for hydrogen production over nickel and cobalt bimetallic catalysts. International Journal of Hydrogen Energy. 34:6646-6654. 2009.

[32] Alessandra F. Lucrédio and José M. Assaf and Elisabete M. Assaf. Reforming of a model biogas on Ni and Rh-Ni catalysts: effect of adding La. Fuel Processing Technology. 102:124-131. 2012.

[33] M. Benito, S. García, P. Ferreira-Aparicio, L. García Serrano and L. Daza. Development of biogas reforming Ni-La-Al catalysts for fuel cell. Journal of Power Sources. 169:177-183. 2007.

[34] Xenophon E. Verykios. Catalytic dry reforming of natural gas for the production of chemicals and hydrogen. International Journal of Hydrogen Energy. 28:1045-1063. 2003.

[35] A. Serrano-Lotina, L. Rodríguez, G. Muñoz and L. Daza. Biogas reforming on La-promoted NiMgAl catalysts derived from hydrotalcite-like percursors. Journal of Power Sources. 196:4404-4410. 2011.

[36] A. Serrano-Lotina, L. Rodríguez, G. Muñoz, A. J. Martin, M. A. Folgado and L. Daza. Biogas reforming over La-NiMgAl catalysts derived from hydrotalcite-like structure: influence of calcination temperature. Catalysis Communications. 12:961-967. 2011.

[37] Mun-Sing Fan, Ahmad Zuhairi Adbullah and Subhash Bhatia. Utilization of greenhouse gases through carbon dioxide reforming of methane over $Ni-Co/MgO-ZrO_2$: preparation, characterizationand activity studies. Applied Catalysis B: Environmental. 100:365-377. 2010.

[38] S. Damyanova, B. Pawelec, K. Arishtirova and J. L. G. Fierro. Biogas reforming over bimetallic PdNi catalysts supported on phosphorus-modified alumina. International Journal of Hydrogen Energy. 36:10635-10647. 2011.

[39] J. L Pinilla, S. de Llobet, I. Suelves, R. Utrilla, M. J. Lázaro and R. Moliner. Catalytic decomposition of methane and methane/CO_2 mixtures to produce synthesis gas and nanostructured carbonaceous material. Fuel. 90:2245-2253. 2011.

[40] S. de Llobet, J. L Pinilla, M. J. Lázaro, R. Moliner and I. Suelves. Catalytic decomposition of biogas to produce H_2-rich fuel gas and carbon nanofibers. Parametric study and characterization. International Journal of Hydrogen Energy. 37:7067-7076. 2012.

[41] D. G. Avraam, T. I. Halkides, D. K. Linguras, O. A. Bereketidou and M. A. Goula. An experimental and theoretical approach for the biogas steam reforming reaction. International Journal of Hydrogen Energy. 35:9818-9827. 2010.

[42] A. Effendi, Z.-G. Zhang, K. Hellgardt, K. Honda, T. Yoshida. Steam reforming of a clean model biogas over Ni/Al_2O_3 in fluidized- and fixed-bed reactors. Catalysis Today. 77:181-189. 2002.

[43] Philipp Kolbitsch, Christoph Pfeifer and Hermann Hofbauer. Catalytic steam reforming of model biogas. Fuel. 87:701-706. 2008.

[44] O. Deutschmann, H. Knözinger, K. Kochloefl and T. Turek. Heterogeneous Catalysis and Solid Catalysts, 1. Fundamentals. Ullmann's Encyclopedia of Industrial Chemistry. 2011.

[45] Jens Sehested. Four challenges for nickel steam-reforming catalysts. Catalysis Today. 111:103-110. 2006.

[46] John N. Armor. The multiple roles for catalysis in the production of H_2. Applied Catalysis A: General. 171:159-176. 1999.

[47] Tatsuro Horiuchi, Kaori Sakuma, Takehisa Fukui, Yukio Kubo, Toshihiko Osaki and Toshiaki Mori. Suppression of carbon deposition in the CO2-reforming of CH4 by adding basic metal oxided to a Ni/Al2O3 catalyst. Applied Catalysis A: General. 144:111-120. 1996.

[48] Shaobin Wang and G. Q. (Max) Lu. Role of CeO_2 in Ni/CeO_2-Al_2O_3 catalysts for carbon dioxide reforming of methane. Applied Catalysis B: Environmental. 19:267-277. 1998.

[49] H. Y. Wang and E. Ruckenstein. Carbon dioxide reforming of methane to synthesis gas over supported rhodium catalysts: the effect of the support. Applied Catalysis A: General. 204:143-152. 2000.

[50] M. Tessié du Motay and M. Marechal. Industrial Preparation of Hydrogen (in French). Bull Mensuel de la Société Chimique de Paris. 9:334-334. 1868.

[51] L. Mond and C. Langer. Chem. Zentralbl. II, 32. 1980.

[52] J. R. Rostrup-Nielsen. Sulfur-passivated nickel catalysts for carbon-free steam reforming od methane. Journal of Catalysis. 85:31-43. 1984.

[53] Mojdeh Ashrafi, Tobias Pröll, Christoph Pfeifer and Hermann Hofbauer. Experimental study of model biogas catalytic steam reforming: 1. Thermodynamic optimization. Energy & Fuels. 22:4182-4189. 2008.

[54] Danielle M. Murphy, Amy E. Richards, Andrew Colclasure, Wade A. Rosensteel and Neal P. Sullivan. Biogas fuel reforming for solid oxide fuel cells. Journal of Renewable and Sustainable Energy. 4:023106. 2012.

[55] Mojdeh Ashrafi, Christoph Pfeifer, Tobias Pröll and Hermann Hofbauer. Experimental study of model biogas catalytic steam reforming: 2. Impact of sulfur on the deactivation and regeneration of Ni-based catalysts. Energy & Fuels. 22:4190-4195. 2008.

[56] A. Effendi, K. Hellgardt, Z.-G. Zhang and T. Yoshida. Optimising H_2 production from model biogas via combined steam reforming and CO shift reactions. Fuel. 84:869-874. 2005.

[57] Vasant R. Choudhary and Amarjeet M. Rajput. Simultaneous carbon dioxide and steam reforming of methane to syngas over NiO-CaO catalyst. Industrial & Engineering Chemistry Research. 35:3934-3939. 1996.

[58] V. R. Choudhary, B. S. Uphade and A. S. Mamman. Simultaneous steam and CO_2 reforming to syngas over NiO/MgO/SA-5205 in presence and absence of oxygen. Applied Catalysis A: General. 168:33-46.1998.

[59] Shyamsundar Ayalur, Chattanathan, Sushil Adhikari and Steven Taylor. Conversion of carbon dioxide and methane in biomass synthesis gas for liquid fuels production. International Journal of Hydrogen Energy. 37:18031-18039. 2012.

[60] Zhan-Guo Zhang, Guangwen Xu, Xin Chen, Kazunori Honda and Tadashi Yoshida. Process development of hydrogenous gas for PEFC from biogas. Fuel Processing Technology. 85:1213-1229. 2004.

[61] M. Khoshtinat Nikoo and N. A. S. Amin. Thermodynamic analysis of carbon dioxide reforming of methane in view of solid carbon formation. Fuel Processing Technology. 92:678-691. 2011

[62] Şeyma Özkara-Aydınoğlu. Thermodynamic equilibrium analysis of combined carbon dioxide reforming with steam reforming of methane to synthesis gas. International Journal of Hydrogen Energy. 35:12821-12828. 2010.

[63] Thermodynamic and experimental study of combined dry and steam reforming of methane in Ru/ZrO2-La2O3 catalyst at low temperature. International Journal of Hydrogen Energy. 36:15212-15220. 2011.

[64] H. Liander. The utilization of natural gases for the ammonia process. Transactions of the Faraday Society. 25:462-472.1929.

[65] C. Padovani and P. Franchetti. Giorn. Chem. Ind. Applicatta Catal. 15:429.1933.

[66] M. Pettre, C. H. Eichner and M. Perrin. Catalytic partial oxidation of methane to carbon monoxide and hydrogen. Transactions of the Faraday Society. 43:335-340.1946.

[67] Andrew P. E. York, Tiancun Xiao and Malcolm L. H. Green. Brief overview of the partial oxidation of methane to synthesis gas. Topics in Catalysis. 22:345-358.2003.

[68] D. A. Hickman and L. D. Schmidt. Synthesis gas formation by direct oxidation of methane over Pt monoliths. Journal of Catalysis. 138:267-282. 1992.

[69] D. A. Hickman, E. A. Haupfear and L. D. Schmidt. Synthesis gas formation by direct oxidation of methane over Rh monoliths. Catalysis Letters.17:223-227. 1993.

[70] R. Horn, K. A. Williams, N. J. Degenstein, A.Bitsch-Larsen, D. Dalle Nogare, S. A. Tupy and L. D. Schmidt. Methane catalytic partial oxidation on autothermal Rh and Pt foam catalysts: oxidation and reforming zones, transport effects, and approach to thermodynamic equilibrium. Journal of Catalysis. 249:380-393. 2007.

[71] G. Groppi, A. Beretta and E. Tronconi. Monolithic catalysis for gas-phase syntheses of chemicals (chap. 8). Structured Catalysis and Reactors. Andrzej Cybulski and Jacob A. Moulijn (Eds.). CRC Press. 2006.

[72] Shi Ding, Yinhong Cheng and Yi Cheng. Experimental study and modeling analysis of catalytic partial oxidation of methane with addition of CO_2 and H_2O using a Rh-coated foam monolith reactor. Industrial & Engineering Chemistry Research. 50:856-865. 2011.

[73] Adesoji A. Adesina. The role of CO_2 in hydrocarbon reforming catalysis: friend or foe?. Current Opinion in Chemical Engineering. 1:272-280. 2012.

[74] Wei-Hsiang Lai, Ming-Pin Lai and Rong-Fang Horng. Study on hydrogen-rich syngas production by dry autothermal reforming from biomass derived gas. International Journal of Hydrogen Energy. 37:9619-9629. 2012.

[75] Nor Aishah Saidina Amin and Tung Chun Yaw. Thermodynamic equilibrium analysis of combined carbon dioxide reforming with partial oxidation of methane to syngas. International Journal of Hydrogen Energy. 32:1789-1798. 2007.

[76] Olaf Deutschmann, Renate Schwiedernoch, Luba I. Maier and Daniel Chatterjee. Natural gas conversion in monolithic catalysts: interaction of chemical reactions and transport phenomena. Studies in Surface Science and Catalysis. 136:251-258. 2001

[77] Benjamin T. Schädel, Matthias Duisberg and Olaf Deutschmann. Steam reforming of methane, ethane, propane, buthane, and natural gas over a rhodium-based catalyst. Catalysus Today. 142:42-51. 2009.

[78] Yvan J. O. Asencios, Cristiane B. Rodella and Elisabete M. Assaf. Oxidative reforming of model biogas over NiO-Y_2O_3-ZrO_2 catalysts. Applied Catalysis B: Environmental. 132-132:1-12. 2013

[79] E. Ruckenstein and H. Y. Wang. Combined catalytic partial oxidation and CO_2 reforming of methane over supported cobalt catalysts. Catalysis Letters. 73:99-105. 2001.

[80] Eli Ruckenstein and Yun Hang Hu. Combination of CO_2 reforming and partial oxidation of methane over NiO/MgO solid solution catalysts. Industrial & Engineering Chemistry Research. 37:1744-1747. 1998

[81] Yvan J. O. Asencios, Jorge D. A. Bellido and Elisabete M. Assaf. Synthesis of NiO-MgO-ZrO_2 catalysts and their performance in reforming of model biogas. Applied Catalysis A: General. 397:138-144. 2011.

[82] A. T. Ashcroft, A. K. Cheetham, J. S. Foord, M. L. H. Green, C. P. Grey, A. J. Murrel and P. D. F. Vernon. Selective oxidation of methane to synthesis gas using transition metal catalysts. Nature. 344:319-321. 1990.

[83] G. Pepermans, J. Driesen, D. Haeseldonckx, R. Belmans and W. D'haeseleer. Distributed generation: definition, benefits and issues. Energy Policy. 33:787-798. 2005

[84] S. Ayabe, H. Omoto, T. Utaka, R. Kikuchi, K. Sasaki, Y. Teraoka and K. Eguchi. Catalytic autothermal reforming of methane and propane over supported metal catalysts. Applied Catalysis A: General. 241:261-269. 2003

[85] Tatsuya Takeguchi, Shin-Nosuke Furukawa, Masashi Inoue and Koichi Eguchi. Autothermal reforming of methane over Ni catalysts supported over CaO-CeO_2-ZrO_2 solid solution. Applied Catalysis A: General. 240:223-233. 2003

[86] Mariana M. V. M. Souza and Martin Schmal. Autothermal reforming of methane over Pt/ZrO2/Al2O3 catalysts. Applied Catalysis A: General. 281:19-24. 2005

[87] Stefan Rabe, Thanh-Binh Truong and Frédéric Vogel. Catalytic autothermal reforming of methane: performance of a kW scale reformer using pure oxygen as oxidant. Applied Catalysis A: General. 318:54-62. 2007

[88] D. L. Hoang and S. H. Chan. Modeling of a catalytic autothermal methane reformer for fuel cell applications. Applied Catalysis A: General. 268:207-216. 2004.

[89] V. L. Barrio, G. Schaub, M. Rohde, S. Rabe, F. Vogel, J. F. Cambra, P. L. Arias and M. B. Güemez. Reactor modeling to simulate catalytic partial oxidation and steam reforming of methane. Comparison of temperature profiles and strategies for hot spot minimization. International Journal of Hydrogen Energy. 32:1421-1428. 2007.

[90] M. H. Halabi, M. H. J. M. de Croon, J. van der Schaaf, P. D. Cobden and J. C. Schouten. Modeling and analysis of autothermal reforming of methane to hydrogen in a fixed bed reformer. Chemical Engineering Journal. 137:568-578. 2008.

[91] Jianguo Xu and Gilbert F. Froment. Methane steam reforming, methanation and water-gas shift: I. intrinsic kinetics. AIChE Journal. 35:88-96. 1989.

[92] David L. Trimm and Chi-Wai Lam. The combustion of methane on platinum-alumina fibre catalysts – I: kinetics and mechanism. Chemical Engineering Science. 35:1405-1413. 1980.

[93] L. Ma, D. L. Trimm and C. Jiang. The design and testing of an autothermal reactor for the conversion of light hydrocarbons to hydrogen I. The kinetics of the catalytic oxidation of light hydrocarbons. Applied Catalysis A: General. 138:275-283. 1996.

[94] T. P. Tiemersma, C. S. Patil, M. van Sint Annaland and J. A. M. Kuipers. Modelling of packed bed membrane reactors for autothermal production of ultrapure hydrogen. Chemical Engineering Science. 61:1602-1616. 2006.

[95] Sadao Araki, Naoe Hino, Takuma Mori and Susumu Hikazudani. Durability of a Ni based monolithic catalyst in the autothermal reforming of biogas. International Journal of Hydrogen Energy. 34:4727-4734. 2009.

[96] Sadao Araki, Naoe Hino, Takuma Mori and Susumu Hikazudani. Start-up procedures in autothermaçl reforming of biogas over Ni based catalytic monolith. Catalysis Communications. 10:1300-1304. 2009

[97] Sadao Araki, Naoe Hino, Takuma Mori and Susumu Hikazudani. Autothermal reforming of biogas over a monolithic catalyst. Journal of Natural Gas Chemistry. 19:477-481. 2010.

[98] C. S. Lau, D. Allen, A. Tsolakis, S. E. Golunski and M. L. Wyszynski. Biogas upgrade to syngas through thermochemical recovery using exhaust gas reforming. Biomass and Bioenergy. 40:86-95. 2012.

[99] U. Izquierdo, V. L. Barrio, J. Requies, J. F. Cambra, M. B. Güemex and P. L. Arias. Tri-reforming: a new biogas process for synthesis gas and hydrogen production. International Journal of Hydrogen Energy. In press. 2012.

[100] Daoan Sun, Xiujin Li, Shengfu Ji and Lingyan Cao. Effects of O_2 and H_2O on the tri-reforming of the simulated biogas over Ni-based SBA-15 catalysts. Journal of Natural Gas Chemistry. 19:369-374. 2010.

[101] Chunshan Song and Wei Pan. Tri-reforming of methane: a novel concept for catalytic production of industrially useful synthesis gas with desired H_2/CO ratios. Catalysis Today. 98:463-484. 2005.

[102] Hongtao Jiang, Huiquan Li, Hongbin Xu and Yi Zhang. Preparation of $Ni/Mg_xTi_{1-x}O$ catalysts and investigation on their stability in tri-reforming of methane. Fuel Processing Technology. 88:988-995. 2007.

[103] Jin Xuan, Michael K. H. Leung, Dennis Y. C. Leung and Meng Ni. Integrating chemical kinetics with CFD modeling for autothermal reforming of biogas. International Journal of Hydrogen Energy. 34:9076-9086. 2009.

[104] A. Effendi, K. Hellgardt, Z.-G. Zhang and T. Yoshida. Characterisation of carbon deposits on Ni/SiO2 in the reforming of CH_4-CO_2 using fixed- and fluidized-bed reactors. Catalysis Communications. 4:203-207. 2003.

[105] Xin Chen, Kazunori Honda and Zhan-Guo Zhang. CO_2-CH_4 reforming over $NiO/\gamma.Al_2O_3$ in fized-bed/fluidized-bed switching mode. Catalysis Today. 93-95:87-93. 2004.

[106] T. Wurzel, S. Malcus and L. Mleczko. Reaction engineering investigations of CO_2 reforming in a fluidized-bed reactor. Chemical Engineering Science. 55:3955-3966. 2000.

[107] Pio Forzatti and Luca Lietti. Catalyst deactivation. Catalysis Today. 52:165-181. 1999.

[108] J. A. Moulijn, A. E. van Diepen and F. Kapteijn. Catalyst deactivation: is it predictable? What to do?. Applied Catalysis A: General. 212:3-16. 2001.

[109] Calvin H. Bartholomew. Mechanisms of catalyst deactivation. Applied Catalysis A: General. 212:17-60. 2001.

[110] S. S. Bharadwaj and L. D. Schmidt. Catalytic partial oxidation of natural gas to syngas. Fuel Processing Technology. 42:109-127. 1995.

[111] Ke Liu, Greeg D. Deluga, Anders Bitsch-Larsen, Lanny D. Schmidt and Lingzhi Zhang. Catalytic partial oxidation and autothermal reforming (chap. 3). Hydrogen and Syngas production and purification technologies. Ke Liu, Chunshan Song and Velu Subramani (Eds.). Wiley. 2010.

[112] Kiyoharu Nakagawa, Naoki Ikenaga, Yonghong Teng, Tetsuhiko Kobayashi and Toshimitsu Suzuki. Partial oxidation of methane to synthesis gas over iridium-nickel bimetallic catalysts. Applied Catalysis A: General. 180:183-193. 1999.

[113] S. Tang, J. Lin and K. L. Tan. Partial oxidation of methane to synthesis gas over α-Al_2O_3-supported bimetallic Pt-Co catalysts. Catalysis Letters. 59:129-135. 1999.

[114] Changlin Yu, Weizheng Weng, Qing Shu, Xiangjie Meng, Bin Zhang, Xirong Chen and Xiaochun Zhou. Additive effects of alkaline-earth metals and nickel on the performance of Co/γ-Al_2O_3 in methane catalytic partial oxidation. Journal of Natural Gas Chemistry. 20:135-139. 2011.

[115] Qing Miao, Guoxing Xiong, Shishan Sheng, Wei Cui, Ling Xu and Xiexian Guo. Partial oxidation of methane to syngas over nickel-based catalysts modified by alkali metal oxide and rare earth metal oxide. Applied Catalysis A: General. 154:17-27. 1997.

[116] Yuhong Zhang, Guoxing Xiong, Shishan Sheng and Weishen Yang. Deactivation studies over NiO/γ-Al_2O_3 catalysts for partial oxidation of methane to syngas. Catalysis Today. 63:517-522. 2000.

[117] John B. Claridge, Malcolm L. H. Green, Shik Chi Tsang, Andrew P. E. York, Alexander T. Ashcroft and Peter D. Battle. A study of carbon deposition on catalysts during the partial oxidation of methane to synthesis gas. Catalysis Letters. 22:299-305. 1993.

[118] Toshihiko Osaki and Toshiaki. Role of potassium in carbon-free CO2 reforming of methane on K-promoted Ni/Al2O3 catalysts. Journal of Catalysis. 204:89-97. 2001.

[119] Behzad Nematollahi, Mehran Rezaei and Majid Khajenoori. Combined dry reforming and partial oxidation of methane to synthesis gas on noble metal catalysts. International Journal of Hydrogen Energy. 36:2969-2978. 2011.

[120] Behzad Nematollahi, Mehran Rezaei, Ebrahim Nemati Lay and Majid Khajenoori. Thermodynamic analysis of combined reforming process using Gibbs energy minimization method: in view of solid carbon. Journal of Natural Gas Chemistry. 21:694-702. 2012.

[121] Dhammike Dissanayake, Michael P. Rosynek, Karl C. C. Kharas and Jack H. Lunsford. Partial oxidation of methane to carbon monoxide and hydrogen over a Ni/Al_2O_3 catalyst. Journal of Catalysis. 132:117-127. 1991.

[122] Wei Chu, Qiangu Yan, Shenglin Liu and Guoxing Xiong. Improvements of ceria promoted nickel catalysts for natural gas oxidation to syngas. Studies in Surface Science and Catalysis. 130:3573-3578. 2000.

[123] D. A. Hickman and L. D. Schmidt. Production of syngas by direct catalytic oxidation of methane. Science. 259:343-346. 1993.

[124] D. A. Hickman and L. D. Schmidt. Steps in CH4 oxidation on Pt and Rh surfaces: high-temperature reactor simulations. AIChE Journal. 39:1164-1177. 1993.

[125] Michel G. Poirier, Josée Trudel and Daniel Guay. Partial oxidation of methane over ruthenium catalysts. Catalysis Letters. 21:99-111. 1993.

[126] S. C. Tsang, J. B. Claridge and M. L. H. Green. Recent advances in the conversion of methane to synthesis gas. Catalysis Today. 23:3-15. 1995.

[127] E. Ruckenstein and H. Y. Wang. Effect of support on partial oxidation of methane to synthesis gas over supported rhodium catalysts. Journal of catalysis. 187:151-159. 1999.

[128] A. Guerrero-Ruiz, P. Ferreira-Aparicio, M. B. Bachiller-Baeza and I. Rodríguez-Ramos. Isotopic tracing experiments in syngas production from methane on Ru/Al_2O_3 and Ru/SiO_2. Catalysis Today. 46:99-105. 1998.

[129] Lanny D. Schmidt and Marylin Huff. Partial oxidation of CH_4 and C_2H_6 over noble metalcoated monoliths. Catalysis Today. 21:443-454. 1994.

[130] W. J. M. Vermeiren, E. Blomsma and P. A. Jacobs. Catalytic and thermodynamic approach of the oxyreforming reaction of methane. Catalysis Today. 13:427-436. 1992.

[131] P. M. Hermans. Ph.D. thesis. Technical University of Delft. The Netherlands. 2004.

[132] Kara M.M. Karavayev, A.P. Zasorin, N.F. Kleshchev, Catalytic oxidation of ammonia, Khimia, Moscow, 1983.

[133] S. Albertazzi, P. Arpentinier, F. Basile, P. Del Gallo, G. Fornasari, D. Gary and A. Vaccari. Deactivation of a Pt/γ-Al_2O_3 catalyst in the partial oxidation of methane to synthesis gas. Applied Catalysis A: General. 247:1-7. 2003.

[134] K. D. Campbell, H. Zhang and J. H. Lunsford. Methane activation by the lanthanide oxides. The Journal of Physical Chemistry. 92:750-753. 1988.

[135] Adolfo Parmaliana and Francesco Arena. Working mechanism of oxide catalysts in the partial oxidation of methane to formaldehyde. I. Catalytic behavior of SiO2, MoO_3/SiO_2, V_2O_5/SiO_2, TiO_2, and V_2O_5/TiO_2 systems. Journal of Catalysis. 167:57-65. 1997.

[136] A. G. Steghuis. Ph.D. thesis. University of Twente. The Netherlands. 1998.

[137] A. G. Steghuis, J. G. van Ommen and J. A. Lercher. On the reaction mechanism for methane partial oxidation over yttria/zirconia. Catalysis Today. 46:91-97. 1998.

[138] J. Zhu. Ph.D. thesis. University of Twente. The Netherlands. 2005.

[139] D. D. Nogare. Ph.D. thesis. University of Padova. Italy. 2008.

[140] H. de Smet. Ph.D. thesis. Technical University of Eindhoven. The Netherlands. 2000.

[141] Richard H. Jones, Alexander T. Ashcroft, David Waller, Anthony K. Cheetham and John M. Thomas. Catalytic conversion of methane to synthesis gas over europium iridate, Eu2Ir2O7: an in situ study by X-ray diffraction and mass spectrometry. Catalysis Letters. 8:169-174. 1991.

[142] P. D. F. Vernon, M. L. H. Green, A. K. Cheetham and A. T. Ashcroft. Partial oxidation of methane to synthesis gas, and carbon dioxide as an oxidising agent for methane conversion. Catalysis Today. 13:417-426. 1992.

[143] Patrick D. F. Vernon, Malcolm L. H. Green, Anthony K. Cheetham and Alexander T. Ashcroft. Partial oxidation of methane to synthesis gas. Catalysis Letters. 6:181-186. 1990.

[144] Tierry Poinsot, Denis Veynante. Theoretical and numerical combustion. R. T. Edwards. Philadelphia, USA. 2005.

[145] Renate Schwiedernoch, Steffen Tischer, Chrys Correa and Olaf Deutschmann. Experimental and numerical study on the transient behavior of partial oxidation of methane in a catalytic monolith. Chemical Engineering Science. 58:633-642. 2003.

[146] Alessandro Donazzi, Alessandra Beretta, Gianpiero Groppi and Pio Forzatti. Catalytic partial oxidation of methane over a 4% Rh/α-Al_2O_3 catalyst: part I: kinetic study in annular reactor. Journal of Catalysis. 255:241-258. 2008.

[147] M. Hartmann, L. Maier, H. D. Minh and O. Deutschmann. Catalytic partial oxidation of iso-octane over rhodium catalysts: an experimental, modeling, and simulation study. Combustion and Flame. 157:1771-1782. 2010.

[148] L. Maier, M. Hartmann, S. Tischer and O. Deutschmann. Interaction of heterogeneous and homogeneous kinetics with mass and heat transfer in catalytic reforming of logistic fuels. Combustion and Flame. 158:796-808. 2011.

[149] Alessandra Beretta, Gianpiero Groppi, Matteo Lualdi, Ivan Tavazzi and Pio Forzatti. Experimental and modeling analysis of methane partial oxidation: transient and steady-state behavior of Rh-coated honeycomb monoliths. Industrial & Engineering Chemistry Research. 48:3825-3836. 2009.

[150] Tengfei Liu, Cynthia Snyder and Götz Veser. Catalytic partial oxidation of methane: is a distinction between direct and indirect pathways meaningful?. Industrial & Engineering Chemistry Research. 46:9045-9052. 2007.

[151] M. F. Modest. Radiative heat transfer. McGraw-Hill. New York. 1993.

[152] Sandip Mazumder and Michael Grimm. Numerical investigation of radiation effects in monolithic catalytic combustion reactors. International Journal of Chemical Reactor Engineering. 9. 2011.

[153] Alessandra Beretta, Alessandro Donazzi, Dario Livio, Matteo Maestri, Gianpiero Groppi, Enrico Tronconi and Pio Forzatti. Optimal design of a CH4 CPO-reformer with honeycomb catalyst: combined effect of catalyst load and channel size on the surface temperature profile. Catalysis Today. 171:79-83. 2011.

[154] G. Veser and J. Frauhammer. Modelling steady state and ignition during catalytic methane oxidation on a monolith reactor. Chemical Engineering Science. 55:2271-2286. 2000.

[155] Alessandro Donazzi, Dario Livio, Matteo Maestri, Alessandra Beretta, Gianpiero Groppi, Enrico Tronconi and Pio Forzatti. Synergy of homogeneous and heterogeneous chemistry probed by in situ spatially resolved measurements of temperature and composition. Angewandte Chemie International Edition. 50:3943-3946. 2011.

[156] J. C. Slaa, R. J. Berger and G. B. Marin. Partial oxidation of methane to synthesis gas over Rh/α-Al2O3 at high temperatures. Catalysis Letters. 43:63-70. 1997.

[157] Olaf Deutschmann and Lanny D. Schmidt. Modeling the partial oxidation of methane in a short-contact-time reactor. AIChE Journal. 44:2465-2477. 1998.

[158] R. Shah and A. London. Laminar flow forced convection in ducts. Academic Press. New York. 1978.

[159] N. Wakao and J. M. Smith. Diffusion in catalyst pellets. Chemical Engineering Science. 17:825-834. 1962.

[160] Edward N. Fuller, Paul D. Schettler, J. Calvin Giddings. New method for prediction of binary gas-phase diffusion coefficients. Industrial & Engineering Chemistry. 58:18-27- 1966.

[161] R. Siegel, J. R. Howell, Thermal Radiation Heat Transfer, Hemisphere Publishing Corporation, 1992.

[162] S. Karagiannidis, Catalytic microreactors for portable power generation, Springer, Berlin, 2011.

[163] Symeon Karagiannidis and John Mantzaras. Numerical investigation on the start-up of methane-fueled catalytic microreactors. Combustion and Flame. 157:1400-1413. 2010.

[164] James J. Noble. The Zone method: explicit matrix relations for total exchange areas. International Journal of Heat and Mass Transfer. 18:261-269. 1975.

[165] R. E. Hayes and S. T. Kolaczkowski. Introduction to catalytic combustion. Gordon and Breach Science. Amsterdam. 1997.

[166] R. J. Kee, J. F. Grcar, M. D. Smooke and J. A. Miller. Premix: a Fortran program for modeling steady laminar one-dimensional premixed flames. Technical Report SAND85-8240. Sandia National Laboratories. 1985.

[167] R. J. Kee, F. M. Rubley, E. Meeks. CHEMKIN-II: a Fortran chemical kinetic package for the analysis of gas-phase chemical kinetics. Technical Report SAND89-8009. Sandia National Laboratories. 1989.

[168] R. J. Kee, G. Dixon-Lewis, J. Warnatz, M. E. Coltrin, J. A. Miller. A Fortran computer code package for the evaluation of gas-phase multi-component transport properties. Technical Report SAND86-8246. Sandia National Laboratories. 1986.

[169] G. P. Smith, D. M. Golden, M. Frenklach, N. W. Moriarty, B. Eiteneer, M. Goldenberg, C. T. Bowman, R. K. Hanson, S. Song, W. C. Gardiner, Jr., V. V. Lissianski, Z. Qin, GRI-Mech 3.0, http://www.me.berkeley.edu/gri mech/.

[170] E. Ranzi, A. Sogaro, P. Gaffuri, G. Pennati, C. K. Westbrook and W. J. Pitz. A new comprehensive reaction mechanism for combustion of hydrocarbon fuels. Combustion and Flame. 99:201-211. 1994.

[171] M. Balat and H. Balat. Biogas as a renewable energy source – a review. Energy Sources, Part A. 31:1280-1293. 2009.

[172] Peter Weiland. Biogas production: current state and perspectives. Applied Microbiology and Biotechnology. 85:849-860. 2010.

[173] Christina Papadopoulou, Haris Matralis and Xenophon Verykios. Utilization of biogas as a renewable carbon source: dry reforming of methane (chap. 3). Catalysis for Alternative Energy Generation. László Guczi and András Erdohelyi (Eds.). Springer. 2012.

[174] Lise Appels, Jan Baeyens, Jan Degrève and Raf Dewil. Principles and potential of the anaerobic digestan of waste-activated sludge. Progress in Energy and Combustion Science. 34:755-781. 2008.

[175] P. Holtappels and U. Stimming. Solid oxide fuel cells (SOFC). Hanbook of Fuel Cells: Fudamentals, Technology and Applications. W. Vielstich, A. Lamm, H. A. Gasteiger (Eds.). Wiley & Sons. 2003.

[176] James Larminie and Andrew Dicks. Fuel Cell Systems Explained. Second Edition. Wiley. 2003.

[177] Vittorio Verda and Michele Calí Quaglia. Solid oxide fuel cell systems for distributed power generation and cogeneration. International Journal of Hydrogen Energy. 33:2087-2096. 2008.

[178] Tim Lieuwen, Vince McDonell, Eric Petersen, Domenic Santavicca. Fuel flexibility influences on premixed combustor blowout, flashback, auto-ignition, and stability. ASME Paper. 2006-GT-90770. 2006.

[179] R. J. Gorte and J. M. Vohs. Novel SOFC anodes for the direct electrochemical oxidation of hydrocarbons. Journal of Catalysis. 216:477-486. 2003.

[180] Robert J. Kee, Huayang Zhu and David G. Goodwin. Solid-oxide fuel cells with hydrocarbon fuels. Proceedings of the Combustion Institute. 30:2379-2404. 2005.

[181] Robert J. Kee, Huayang Zhu, A. Mary Sukeshini and S. Jackson. Solid oxide fuel cells: operating principles, current challenges, and the role of syngas. Combustion Science and Technology. 180:1207-1244. 2008.

[182] Siamak Farhad, Yeong Yoo and Feridun Hamdullahpur. Effects of fuel processing methods on industrial scale biogas-fuelled solid oxide fuel cell system for operating in wastewater treatment plants. Journal of Power Sources. 195:1446-14453. 2010.

[183] B. Lindström, J. A. J. Karlsson, P. Ekdunge, L. De Verdier, B. Häggendal, J. Dawody, M. Nilsson and L. J. Pettersson. Diesel fuel reformer for automotive fuel cell applications. International Journal of Hydrogen Energy. 34:3367-3381. 2009.

[184] Heather L. MacLean and Lester B. Lave. Evaluating automobile fuel/propulsion system technologies. Progress in Energy and Combustion Science. 29:1-69. 2003.

[185] Avinash Kumar Agarwal. Biofuels (alcohols and biodiesel) applications as fuels for internal combustion engines. Progress in Energy and Combustion Science. 33:233-271. 2007.

[186] Siamak Farhad and Feridun Hamdullahpur. Developing fuel map to predict the effect of fuel composition on the maximum efficiency of solid oxide fuel cells. Journal of Power Sources. 193:632-638. 2009.

[187] Finn Joensen and Jens R. Rostrup-Nielsen. Coversion of hydrocarbons and alcohols for fuel cells. Journal of Power Sources. 105:195-201. 2002.

[188] D. Mogensen, J.-D. Grunwaldt, P. V. Hendriksen, K. Dam-Johansen and J. U. Nielsen. Internal steam reforming in solid oxide fuel cells: status opportunities of kinetic studies and their impact on modelling. Journal of Power Sources. 196:25-38. 2011.

[189] Massimiliano Lo Faro, Alessandro Stassi, Vincenzo Antonucci, Vincenza Modafferi, Patrizia Frontera, Pierluigi Antonucci and Antonino S. Aricò. Direct utilization of methanol in solid oxide fuel cells: na electrochemical and catalytic study. Enternational Journal of Hydrogen Energy. 36:9977-9986. 2011.

[190] G. Vourliotakis, G. Skevis, M. A. Founti, Z. Al-Hamamre and D. Trimis. Detailed kinetic modelling of the T-POX reforming process using a reactor network approach. International Journal of Hydrogen Energy. 33:2816-2825. 2008.

[191] Z. Al-Hamamre, S. Voss and D. Trimis. Hydrogen production by thermal partial oxidation of hydrocarbon fuels in porous media based reformer. International Journal of Hydrogen Energy. 34:827-832. 2009.

[192] G. Vourliotakis, G. Skevis and M. A. Founti. Assessment of the reactor network approach for integrated modelling of an SOFC system. International Journal of Hydrogen Energy. 36:6112-6122. 2011.

[193] S. Voss, D. Trimis, O. Posdziech and J. Valldorf. Preliminary operational results of a SOFC-based mCHP system within the framework of the EU project FlameSOFC. Proceeding of the Third European Fuel Cell Technology and Applications Coference. EFC2009. Rome. 2009.

[194] Sangho Yoon, Sangho Lee and Joongmyeon Bae. Development of a self-sustaining kW_e-class integrated diesel fuel processing system for solid oxide fuel cells. International Journal of Hydrogen Energy. 36:10302-10310. 2011.

[195] Yaofan Yi, Ashok D. Rao, Jacob Brouwer and G. Scott Samuelsen. Fuel flexibility study of an integrated 25kW SOFC reformer system. Journal of Power Sources. 144:67-76. 2005.

[196] Ch. Keramiotis, G. Vourliotakis, G. Skevis, M. A. Founti, C. Esarte, N. E. Sánchez, A. Millera, R. Bilbao and M. U. Alzueta. Experimental and computational study of methane mixtures pyrolysis in a flow reactor under atmospheric pressure. Energy. 43:103-110. 2012.

[197] A. Gazi, G. Vourliotakis, G. Skevis and M. A. Founti. A modelling study of allene and propyne combustion in flames. Fifth European Combustion Meeting ECM2011. Cardiff. 2011.

[198] A. Gazi, G. Vourliotakis, G. Skevis and M. A. Founti. Assessment of appropriate chemical markers for heat release rate correlation in laminar premixed flames. Fifth European Combustion Meeting ECM2011. Cardiff. 2011.

[199] G. Vourliotakis, G. Skevis and M. A. Founti. A detailed kinetic modeling study of benzene oxidation and combustion in premixed flames and ideal reactors. Energy & Fuels. 25:1950-1963. 2011.

[200] G. Vourliotakis, G. Skevis and M. A. Founti. Detailed kinetic modelling of non-catalytic ethanol reforming for SOFC applications. International Journal of Hydrogen Energy. 34:7626-7637. 2009.

[201] N. A. Slavinskaya and P. Frank. A modelling study of aromatic soot precursors formation in laminar methane and ethane flames. Combustion and Flame. 156:1705-1722. 2009.

[202] D. Giannopoulos, D. I. Kolaitis, A. Togkalidou, G. Skevis and M. A. Founti. Quantification of emissions from the co-incineration of cutting oil emulsions in cement plants – Part I: NOx, CO and VOC. Fuel. 86:1144-1152. 2007.

[203] Chemkin collection. Release 4.1. San Diego, CA: Reaction Design, Inc.. 2006.

[204] Pino Sabia, Mara de Joannon, Antonio Picarelli, Alfonso Chinnici and Raffaele Ragucci. Modeling negative temperature coeficiente region in methane oxidation. Fuel. 91:238-245. 2012

[205] N. Lamoureux and C.-E. Paillard. Natural gas ignition delay times behind reflected shock waves: application to modelling and safety. Shock Waves. 13:57-68. 2003.

[206] Michael Frenklach. Reaction mechanism of soot formation in flames. Physical Chemistry Chemical Physics. 4:2028-2037. 2002.

[207] J. Meusinger, E. Riensche and U. Stimming. Reforming of natural gas in solid oxide fuel cell systems. Journal of Power Sources. 71:315-320. 1998.

[208] M. Pilar Ruiz, Roberto Guzmán de Villoria, Ángela Millera, María U. Alzueta and Rafael Bilbao. Influence of different operation conditions on soot formation from C_2H_2 pyrolysis. Industrial & Engineering Chemistry Research. 46:7550-7560. 2007.

[209] Claudia Esarte, María Peg, María P. Ruiz, Ángela Millera, Rafael Bilbao and María U. Alzueta. Pyrolysis of etanol: gas and soot products formed. Industrial & Engineering Chemistry Research. 50:4412-4419. 2011.

[210] C. Esarte, A. Callejas, A. Millera, R. Bilbao, M. U. Alzueta. Influence of the concentration of etanol and the interaction of compounds in the pyrolysis of acetylene and etanol mixtures. Fuel. 90:844-849. 2011.

[211] Claudia Esarte, Ángela Millera, Rafael Bilbao and María U. Alzueta. Gas and soot products formed in the pyrolysis of acetylene-ethanol blends under flow reactor conditions. Fuel Processing Technology. 90:496-503. 2009.

[212] R. P. Lindstedt and G. Skevis. Chemistry of acetylene flames. Combustion Science and Technology. 125:73-137. 1997.

[213] R. P. Lindstedt and G. Skevis. Molecular growth and oxygenated species formation in laminar ethylene flames. Proceedings of the Combustion Institute. 28:1801-1807. 2000.

[214] Rafael Bilbao, Angela Millera, Maria U. Alzueta and Lina Prada. Evaluating of the use of different hydrocarbon fuels for gas reburning. Fuel. 76:1401-1407. 1997.

[215] Maria U. Alzueta, Peter Glarborg and Kim Dam-Johansen. Low temperature interactions between hydrocarbons and nitric oxide: an experimental study. Combustion and Flame. 109:25-36. 1997.

[216] M. Abián, A. Millera, R. Bilbao and M. U. Alzueta. Experimental study on the effect of different CO_2 concentrations on soot and gas products from ethylene thermal decomposition. Fuel. 91:307-312. 2012.

[217] Jin Xuan, Michael K. H. Leung, Dennis Y. C. Leung and Meng Ni. A review of biomass-derived fuel processors for fuel cell systems. Renewable and Sustainable Energy Reviews. 13:1301-1313. 2009.

[218] Vicente Bermúdez, José M. Lujan, Benjamín Pla and Waldemar G. Linares. Effects of low pressure exhaust gas recirculation on regulated and unregulated gaseous emissions during NEDC in a light-duty diesel engine. Energy. 36:5655-5665. 2011.

[219] Robert H. Natelson, Rodney O. Johnson, Matthew S. Kurman, Nicholas P. Cernansky and David L. Miller. Comparison of reactivity in a flow reactor under a single cylinder engine. Experimental Thermal and Fluid Science. 34:928-932. 2010.

[220] D. X. Du, R. L. Axelbaum and C. K. Law. The influence of carbon dioxide and oxygen as additives on soot formation in diffusion flames. Symposium (International) on Combustion. 23:1501-1507. 1991.

[221] Fengshan Liu, Hongsheng Guo, Gregory J. Smallwood and Ömer L. Gülder. The chemical effects of carbon dioxide as an additive in an ethylene diffusion flame: implications for soot and NO_x formation. Combustion and Flame. 125:778-787. 2001.

[222] J. M. Moe. Design of water-gas shift reaction. Chemical Engineering Progress. 58:33-39. 1962.

[223] Yongtaek Choi and Harvey G. Stenger. Water gas shift reaction kinetics and reactor modeling for fuel cell grade hydrogen. Journal of Power Sources. 124:432-439. 2003.

[224] D. L. Baulch, C. T. Bowman, C. J. Cobos, R. A. Cox, T. Just, J. A. Kerr, et al. Evaluating kinetic data for combustion modeling: supplement II. Journal of Physical and Chemical Reference Data. 34:757-1359. 2005.

Appendix I: Biogas/landfill gas production

1. Biogas - Methanogenic fermentation process description

Methane fermentation is a versatile fermentation biotechnology which is able to convert all classes of polymeric materials into methane and carbon dioxide under anaerobic conditions. This process is obtained as a result of consecutive biochemical breakdown of polymers into methane and carbon dioxide in an environment in which harmoniously coexist a variety of microorganisms such as fermentative bacteria (acidogenics), hydrogen producers, acetate producers (acetogenics) and methane-producing (methanogenics), producing the final products in reduced state. Anaerobic microorganisms play an important role in establishing a stable environment in various stages of methane fermentation.

Methane fermentation offers effective ways to reduce pollution through processes that are more efficient than conventional aerobic processes. Although anaerobic digestion is practiced for several decades, only recently the interest in this area focused on the capitalization of fuel gas obtained from industrial and agricultural waste.

Methane fermentation is the result of a series of metabolic interactions between different groups of microorganisms. A description of the microorganisms involved in methane fermentation, based on an analysis of bacteria isolated from the activated sludge digesters and manure from several types of animals, is illustrated in Figure I-1. The first group of organisms secretes enzymes to hydrolyze polymeric materials such as glucose and amino acid monomers, which are further converted into volatile fatty acids, H_2 and acetic acid (Figure I-1, stage 1). In the second stage, hydrogen-producing acetogenic bacteria convert volatile fatty acids produced (ex. propionic and butyric acid) in H_2, CO_2 and acetic acid. Finally, the third group, methanogenic bacteria convert the H_2, CO_2 and acetates in CH_4 and CO_2.

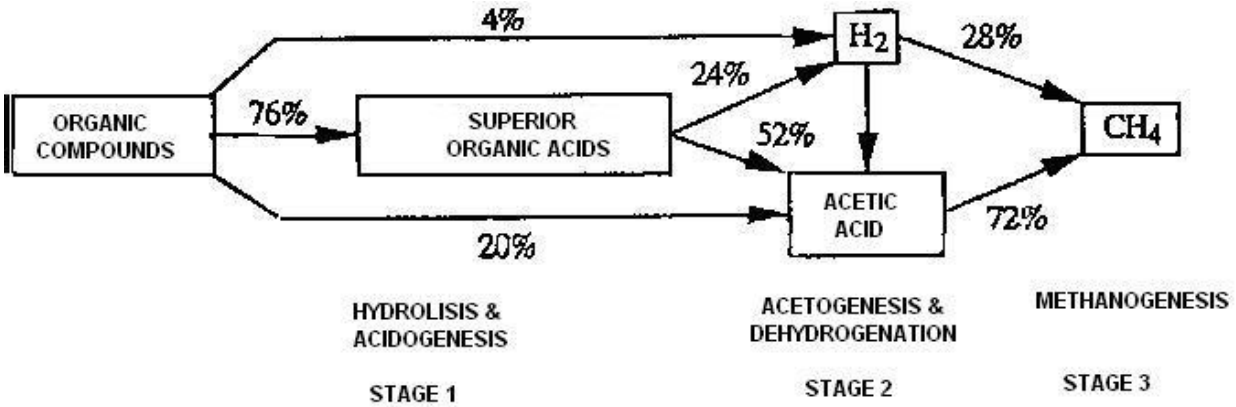

Figure I-1. Mechanisms involved in the methanogenic fermentation.

1.1 Hydrolysis and acidogenesis

Polymeric materials such as lipids, proteins and carbohydrates are hydrolysed primarily by extracellular hydrolases excreted by microorganisms present in stage 1 (Figure I-1). Hydrolytic enzymes (lipases, proteases, cellulases and amylases, etc.) hydrolyze the polymers to

correspondent smaller molecules, primary monomer units, which are then consumed by microorganisms. In the methanogenic fermentation of wastewater with high concentration of organic polymers, the hydrolytic activity relevant to each polymer has a great significance, since polymer hydrolysis may become a limiting step in producing a simple bacterial substrate to be used in the next stages of decomposition.

Lipases convert lipids to long-chain fatty acids. It has been reported a population density of 10^4 - 10^5 lypolitic bacteria per ml of fluid in the digester. It seems that micrococci and clostridia are responsible for the most part, for the production of extracellular lipase. Long-chain fatty acids produced are further reduced by p-oxidation to produce acetyl CoA.

Proteins are generally hydrolysed into aminoacids by proteases secreted by Bacteroides, Butyrivibrio, Clostridium, Fusobacterium, Selenomonas and Streptococcus. Aminoacids produced are then broken down into fatty acids such as acetate, propionate and butyrate and ammonia as shown in the case of Clostridium, Peptococcus, Selonomonas, Campylobacter, and Bacteroides.

Polysaccharides such as cellulose, starch and peptides are hydrolysed by cellulases, amylases and peptilases. Most of microbial cellulases are composed of three species: (a) endo-(3-I, 4-glucanase, (b) exo-p-l, 4-glucanases, (c) or p-glucosidase cellobiose. The three enzymes act synergistically on cellulose to effective hydrolization of its crystalline structure to produce glucose. Microbial hydrolysis of raw starch into glucose requires amylolytic activity, which consists in five species of amylase: (a) a-amylases which cleaves α ± 1-4 internal linkages (b) p-amylases which cleaves the α ± 1-4 external links (c) amyloglucosidases which exocleaves the α ± 1-4 and α ± 1-6 links (d) decomposing enzymes that act on the α ± 1-6 links (e) maltases acting on maltoses releasing glucose. Peptides are decomposed by peptinases, including peptinesterases and depolymerases. Xylans are decomposed with α^2 endo-xylanases and α^2 xylosidases to produce xylose.

Hexoses and pentoses are generally converted into C2 and C3 intermediates and reduced electron carriers (ex. NADH) through common procedures. Most anaerobic bacteria support a hexose metabolism by the Emden-Meyerhof-Parnas (EMP) pathways that produce pyruvate with NADH as a facilitator. Pyruvate and NADH thus generated are converted into the endo-products of fermentation such as lactate, propionate, acetate and ethanol by other enzymatic activities which vary greatly from one microbial species to another.

Thus, in hydrolysis and acidogenesis (Figure I-1, stage 1), sugars, amino acids and fatty acids produced by microbial decomposition of biopolymers are sequentially metabolized by fermentation of endo-products such as lactates, propionates, acetates and ethanol by other enzymatic activities ranging greatly from a microbial species to another. In hydrolysis and acidogenesis (Figure I-1, stage 1), sugars, amino acids and fatty acids produced by microbial decomposition of biopolymers are metabolized by successive groups of bacteria and are fermented primary to acetate, propionate, butyrate, lactate, ethanol, carbon dioxide and hydrogen.

1.2 Acetogenesis and dehydrogenation

Although part of the acetate (20%) and hydrogen are produced directly by acidogenic fermentation of sugars and amino acids they are both derived products resulting from dehydrogenation and acetogenesis of very volatile fatty acids.

Mandatory H_2-consuming acetogene bacteria are capable of producing hydrogen and acetate from higher fatty acids. Only in Syntrophobacter wolinii, a decomposer of propionate, a butyrate decomposer could be isolated due to technical difficulties involved in isolating pure strains because hydrogen produced strongly inhibits the growth of these strains. Using combined techniques

incorporating both cultures of consumers of H_2 and methanogenic and sulfate reducing bacteria has facilitated the elucidation of biochemical decomposition of fatty acids.

Production of hydrogen by acetogene bacteria is generally energy unfavorable due to the high needs for free energy. However, a combination with H_2-consuming bacteria has provided favorable conditions for decomposition of fatty acids to acetate and CH_4 or H_2S.

As an addition to the decomposition of long chain fatty acids, ethanol and lactate were also converted to acetate and hydrogen by an acetogenic bacteria respectively Clostridium formicoaceticum.

Effect of hydrogen partial pressure on the free energy associated with the conversion of ethanol, propionate, acetate and H_2/CO_2 during the methanogenic fermentation is shown in Figure I-2. A very small partial pressure of H_2 (10^{-5} atm) seems to be a significant factor in the degradation of propionate to methane.

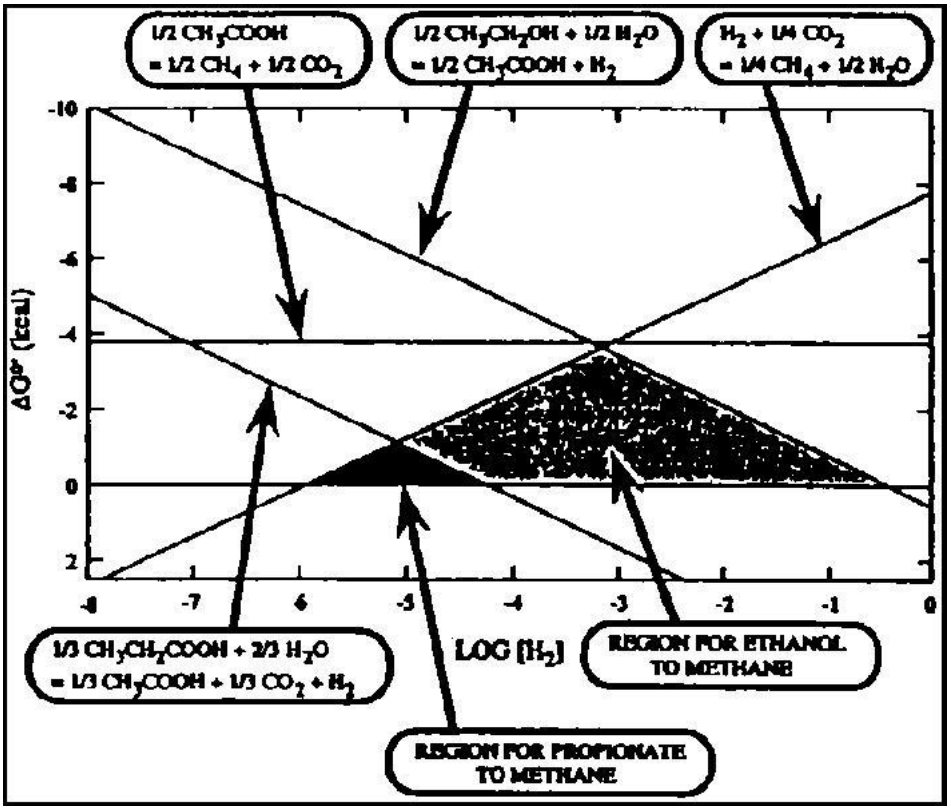

Figure I-2. Effect of hydrogen partial pressure on the free energy associated with the conversion of ethanol, propionate, acetate and H_2/CO_2 during the methanogenic fermentation.

1.3 Methanogenesis

Methanogenic bacteria are physiologicaly related as methane producers by anaerobic digestion. Although acetate and H_2/CO_2 are the main substrates in nature, these are converted to CH_4 and formate, methanol, methylamines, and CO.

Reactions proposed to be involved in the catabolism of fatty acids by Syntrophomonas Wolfei are:

- Acids with even number of carbon atoms

$CH_3CH_2CH_2COO^- + 2\ H_2O \leftrightarrow 2\ CH_3COO^- + 2H_2 + H^+$

$CH_3CH_2CH_2CH_2CH_2COO^- + 4\ H_2O \leftrightarrow 3\ CH_3COO^- + 4H_2 + 2H^+$

$CH_3CH_2CH_2CH_2CH_2CH_2CH_2COO^- + 6\ H_2O \leftrightarrow 4\ CH_3COO^- + 6H_2 + 3H^+$

- Acids with odd number of carbon atoms

$CH_3CH_2CH_2CH_2COO^- + 1\ H_2O \leftrightarrow CH_3CH_2COO^- + CH_3COO^- + 2\ H_2 + H^+$

$CH_3CH_2CH_2CH_2CH_2CH_2COO^- + 4\ H_2O \leftrightarrow CH_3CH_2COO^- + 2\ CH_3COO^- + 4\ H_2 + 2H^+$

- Branched-chain acids

$$CH_3CH(CH_3)CH_2CH_2CH_2COO^- + 2\ H_2O \leftrightarrow CH_3CH(CH_3)CH_2COO^- + CH_3COO^- + 2H_2 + H^+$$

Table I-1. Exchanges of free energy from reactions involving anaerobic oxidation in pure cultures or mixed cultures with H_2 users bacteria or Desulfovibrio species.

Chemical reaction	α" G^0 (kJ / reaction)
1. Proton reducers acetogenic bacteria (producers of H_2)	
A. $CH_3CH_2CH_2COO^- + 2H_2O \leftrightarrow 2\ CH_3COO^- + 2H_2 + H^+$	+ 48.1
B. $CH_3CH_2COO^- + 3H_2O \leftrightarrow CH_3COO^- + HCO_3^- + H^+ + 3H_2$	+ 76.1
2. Methanogenic bacteria that use H_2 and Desulfovibrio species	
C. $4H_2 + HCO_3^- + H^+ \leftrightarrow CH_4 + 3\ H_2O$	- 135.6
D. $4H_2 + SO_4^{2-} + H^+ \leftrightarrow HS^- + 4\ H_2O$	- 151.9
3. Combinated culture 1. + 2.	
A + C $2\ CH_3CH_2CH_2COO^- + HCO_3^- + H_2O \leftrightarrow 4\ CH_3COO^- + H^+ + CH_4$	- 39.4
A + D $2\ CH_3CH_2CH_2COO^- + SO_4^{2-} \leftrightarrow 4\ CH_3COO^- + H^+ + HS^-$	- 55.7
B + C $4\ CH_3CH_2COO^- + 12H_2 \leftrightarrow 4\ CH_3COO^- + HCO_3^- + H^+ + 3\ CH_4$	- 102.4
B + D $4\ CH_3CH_2COO^- + 3\ SO_4^{2} \leftrightarrow 4\ CH_3COO^- + 4\ HCO_3^- + H^+ + 3\ HS^-$	- 151.5

Table I-2. Energy producers reactions of methanogenic bacteria.

No	Chemical reaction	- G^0 (kJ/mol substrate)
1.	$CO_2 + 4\ H_2 \rightarrow CH_4 + 2H_2O$	-130.7
	$HCO_3^- + 4\ H_2 + H^+ \rightarrow CH_4 + 3\ H_2O$	-135.5
2.	$CH_3COO^- + H^+ \rightarrow H_4 + CO_2$	-37.0
	$CH_3COO^- + H_2O \rightarrow CH_4 + HCO_3^-$	-32.3
3.	$HCOO^- + H^+ \rightarrow 0.25\ CH_4 + 0.75\ CO_2 + 0.5\ H_2O$	-36.1
4.	$CO + 0.5\ H_2O \rightarrow 0.25\ CH_4 + 0.75\ CO_2$	-52.7
5.	$CO + 0.5\ H_2O \rightarrow 0.25\ CH_4 + 0.75\ CO_2$	-79.9
6.	$CH_3OH \rightarrow 0.75\ CH_4 + 0.25\ CO_2 + 0.5\ H_2O$	-57.4
7.	$CH_3NH_3^+ + 0.5\ H_2O \rightarrow 0.75\ CH_4 + 0.25\ CO_2 + NH_4^+$	-112.2
8.	$(CH_3)_2NH_2^+ + H_2O \rightarrow 1.5\ CH_4 + 0.5\ CO_2 + NH_4^+$	-105.0
9.	$(CH_3)_3NH + 1.5H_2O \rightarrow 2.25\ CH_4 + 0.75\ CO_2 + NH_4^+$	-170.8

Since methanogenic bacteria are mandatory anaerobic and require a minimum redox potential of -300 mV to growth, isolation and cultivation is quite cumbersome due to difficulties encountered in their handling conditions without O_2.
Metanogenic bacteria can be divided into two groups:
- H_2/CO_2 consumers;
- acetate consumers.
Although some H_2/CO_2 consuming bacteria are able to utilize formate, acetate is consumed only by a limited number of strains, ex. Methanosarcina and Methanothrix (Methanosaeta) that are unable to use formate. Because in the nature it is produced a large amount of acetate, and Methanosarcina Methanothrix play an important role in finalizing the anaerobic digestion and accumulation of H_2, which inhibits acetogenic and methanogenic organisms. H_2 consuming methanogenic bacteria are also important in maintaining low levels of atmospheric H_2.
H_2/CO_2 consuming methanogenic bacteria reduce CO_2 as an electron acceptor by mechanisms types such as: formate, methynil and methyl, in association with less usual coenzymes to ultimately produce CH_4.
Acetoclasic general reaction can be expressed this way:

$$CH_3COOH \rightarrow CH_4 + CO_2$$

As a small part of CO_2 is also formed from carbon derived from methyl group, it is assumed that the reducing potential producted by group CH_3-, could reduce CO_2 to CH_4.

2. Landfill gas

Landfill gas is produced by the microbial decomposition of organic substances in humid media. Like other fermentation gases, landfill gas is vapour-saturated and consists predominantly of methane and carbon dioxide. In addition, landfill gas contains a variety of trace compounds. The decomposition processes run over several stages and can be divided into an aerobic phase and an anaerobic phase.

In the first stage, immediately after the disposal of the waste, the biologically easily available organic materials, such as simple carbohydrates (glucose) and certain proteins are decomposed in an aerobic way, as long as oxygen is present in the landfill body. As main products, carbon dioxide, which is set free into the gaseous phase, water and mineral components are formed.
The significant decomposition processes carry out themselves under anaerobic conditions, as soon as the oxygen is consumed by the aerobic processes in the landfill body. The complete anaerobic decomposition of organic wastes takes place under disproportionation reactions. Typically, for the time dependent progress of complex biochemical degradation processes taking place in the landfill body, characteristic phases are recognised, in which differently built up gases are emitted. In Figure I-3 are shown the concentrations of the main gas components over a period of several decades and the four most important phases of the landfill gas development.

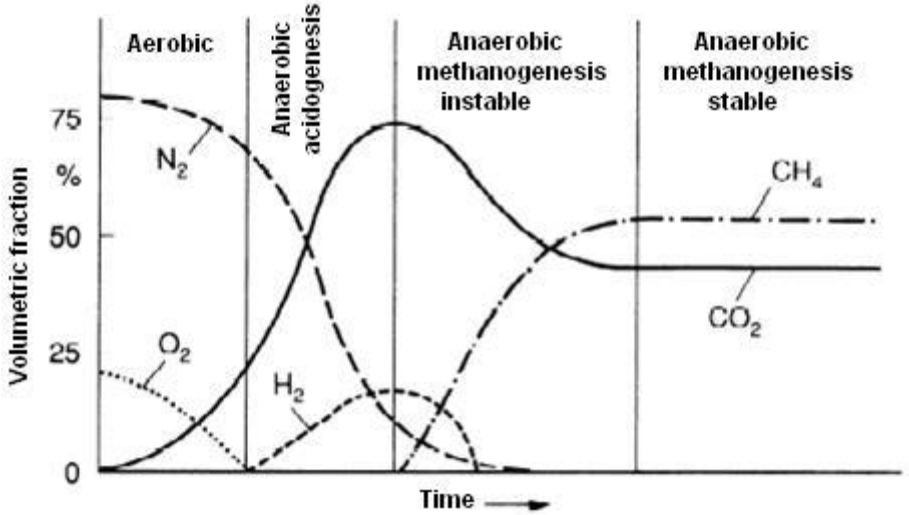

Figure I-3. Evolution of landfill gas composition over time.

If waste is freshly disposed in the landfill body, the decomposition reactions taking place in the first phase under anaerobic conditions are the decomposition of the organic fractions (carbohydrates, fats and proteins) to simple sugars, fatty acids and amino acids. In phase I, the oxygen available in the pore area is rapidly used by the aerobe micro-organisms; therefore only easily decomposable materials are degraded. The phase I persists between one week and several months. The further decomposition processes are anaerobically executed. Facultative anaerobic bacteria decompose the complex waste components in phase II to fatty acids, alcohols, carbon dioxide, hydrogen and water. The N_2-concentration in the landfill body sinks and CO_2-concentrations of up to 80% are reached. Phase II is also called “acid fermentation” because of the strong rise of fat and carbonic acids. In phase III (duration: 3 months to 3 years), the methanogenic bacteria begin to reduce the fatty acids to methane and carbon dioxide, while the hydrogen content drops. About 1-3 years after bringing the waste materials into the landfill body, the phase IV will achieve the so-called stable methane fermentation, which leads to a constant ratio of the CH_4 to CO_2 production (1.3-1.4) and which remains constant over a long period of up to 40 years. Oxygen and nitrogen appear in landfill gas only as trace components. A long-term phase follows phase IV up, which is characterised by a rise of the CH_4/CO_2 ratio (1.5-4). Methane contents of up to 80% can be achieved here. After the long-term phase the air penetration air phase follows up, in which due to the leaving landfill gas production, the gas pressure in the landfill body decreases and thus, air from outside can penetrate into the landfill body. This leads to an oxidation of methane, whereby the atmospheric oxygen is used. A rise in the CH_4/CO_2 ratio is caused by the dropping of the CH_4 content. The more air penetrates into the landfill body the more methane is oxidised to CO_2; the

CH_4/CO_2 ratio decreases down to a value of <1. In this phase no more gas is emitted into the atmosphere. With progressive aging of the landfill body, the CH_4 production finally succumbs. Within remaining regions of the landfill body, where still another anaerobic environment prevails, CH_4 is completely converted into CO_2, so that the CO_2-concentration increases in relation to the normal ground air composition. Remaining organic material is converted now by aerobic decomposition to CO_2. No more CO_2 is formed by the terminated decomposition of the organic material; penetrating air reduces the CO_2 content to some percents, while the oxygen concentration rises to 18-20%.

In the landfill body gases are formed by microbial degradation activity, which is mainly composed of CH_4 and CO_2. In the stable methane phase a concentration relationship of 6:4 to 6:5 between CH_4 and CO_2 is reached. These values change for covered landfills and very little for large depths in the landfill body. The landfill gas composition of an entire landfill, changes if in individual landfill sections specific situations occur. Depending on how the landfill gas is collected (type of collection system) and taken out of the landfill body, a mixed landfill gas arises, which is diluted with air. Nitrogen and oxygen must be considered therefore, as main components in the landfill gas mixtures. If the nitrogen concentration is larger than 18%, leakages in the suction system are probably present or the suction performance of the degassing plant is too high.

Apart from the main components, landfill gas consists of a multiplicity of organic and inorganic trace compounds. These trace component represent a complex mixture of more than hundred single materials, which can constitute up to 15 Vol.-% of the landfill gas. Here it is to be considered, that substantial fluctuations of the composition and the material concentrations can occur from landfill site to landfill site, as well as within a landfill body. The following substance classes have been detected in landfill gas: a) aldehydes & ketones, b) esters & alcohols, c) ethers, d) inorganic & organic-nitrogen compounds, e) alkanes & cycloalkanes, f) alkenes & cycloalkenes, g) terpenes, h) aromatics, i) veavy-volatile organics (PAH, PCB), j) organometallics, k) halogenated compounds including CFC's, l) hydrogen sulphide & sulphur-organic compounds, m) silicon-organic compounds (volatile siloxanes and silanes).

The main components of the identified trace materials are alkanes, terpenes, aromatic compounds, halogenated hydrocarbons, hydrogen sulphide and siloxanes. The mentioned trace compounds are on the one hand, intermediate catabolic products of the microbial degradation of the biomass and on the other hand, they can occur in the landfill body through the storing of waste or through the biochemical conversion of such stored materials. From natural processes of transformation results from example, esters, aldehydes and alcohols (decomposition of carbohydrates), while sulphur-organic compounds are formed by the decomposition of amino acids.

Sulphate-reducing bacteria are responsible for the production of hydrogen sulphide. Terpenes can develop either by the decomposition of biomass or by being brought into the landfill by a multiplicity of products, which contain terpenes as scent components or fruit essences. Terpenes can be converted by dehydrogenation into substituted benzene, which are found later in the landfill gas. Aromatic compounds (BTX) count likewise to the anthropogenic trace components, which are used as solvents in various technical products (for example cleaning gasoline). Also halogenated hydrocarbons are frequently used as solvents, for instance during the dry-cleaning or the treatment of textiles.

Landfill gas is in comparison to biogas, heavily loaded with pollutants. The broad spectrum of the landfill gas components requires relatively complex gas processing methods.

Appendix II: Elemental and compositional analysis of biogas/landfill gas

Tables II-1 to II-14 of section 1 of this appendix show the landfill gas composition of some of municipal landfill sites in Germany, Italy, Spain and Finland [1-2]. The analyses confirm the general statements about the landfill gas composition mentioned before. Beside alkanes and terpenes, BTX and siloxanes are present in substantial concentrations. The contents of chlorinated compounds and CFC's in the landfill gas are clearly lower. The use of these compounds was strongly limited in the past years or completely forbidden, so that in the course of the time, the storage of halogenated compounds was constantly reduced and for this reason their fraction in the landfill gas drops down. The landfill gas at all sites contains variable concentrations of siloxanes.

1. Composition of some of municipal landfill sites in Germany, Italy, Spain and Finland

Table II-1. Sewage gas composition from a plant in Germany [1].

		Sewage Gas		
[vol.-%]	Composition (Dry)	From	Until	Average
	Methane CH_4	59.5	73.8	65.0
	Carbon Dioxide CO_2	39.5	25.9	34.0
	Nitrogen N_2	1.0	-	1.0
	Oxygen O_2	0.01	0.3	0.1
Trace	Hydrogen Sulfide H_2S	100	1.000	500
Compounds	Ammonia NH_3	0.1	10	0.1
[mg/m^3]	Alkane	0.1	6	0.1
	C_{2+}-KW [vol.-%]			
Characteristic	Heat of Combustion [kWh/m^3]	6.6	8.2	7.2
Technical	Calorific Value [kWh/m^3]	6.1	7.4	6.5
Combustion	Rel. Density d(Air=1)	0.97	0.81	0.90
Data	Wobbe Index [kWh/m^3]	6.7	9.1	7.6

Table II-2. Average Raw Sewage Gas Composition at the Sewage Treatment Plant Wuppertal Kohlfurth – Germany [1].

Compound	Formula	Unit	Value
Major Components			
Methane	CH_4	Vol.-%	62-66
Carbon Dioxide	CO_2	Vol.-%	33-37

Minor Components			
Nitrogen	N_2	Vol.-%	<0,2
Oxygen	O_2	ppm	<500
BTX			
Benzene	C_6H_6	ppb	30-50
Toluene	C_7H_8	ppm	2-25
Xylene*	C_8H_{10}	ppb	100-250
Trimethylbenzene**	C_9H_{12}	ppb	100-200
Sulphur			
Hydrogen Sulphide	H_2S	ppm	7-35
Carbonyl Sulphide	COS	ppb	<100
Methanethiol (methyl mercaptan)	CH_3SH	ppb	<100
Carbon disulphide	CS_2	ppb	<50
Chlorine			
Chlorobenzene	C_6H_5Cl	ppb	<20
Siloxane ***			
L2-Hexamethyldisiloxane	$C_6H_{18}OSi_2$	ppb	<40
L3-Octamethyltrisiloxane	$C_8H_{24}O_2Si_3$	ppb	<350
L4-Decamethyltetrasiloxane	$C_{10}H_{30}O_3Si_4$	ppb	<180
D3-Hexamethylcyclotrisiloxane	$C_6H_{18}O_3Si_3$	ppb	<100
D4-Octamethylcyclotetrasiloxane	$C_8H_{24}O_4Si_4$	ppb	<500
D5-Decamethylcyclopentasiloxane	$C_{10}H_{30}O_5Si_5$	ppb	<1000

* representative for o-/p-/m-Xylene or Ethylbenzene

** representative for 1,3,5 – Trimethylbenzene and 1,2,4 – Trimethylbenzene

*** indirect Calibration with off – line data from the company C.A.U. Dreieich

Table II-3. Landfill Gas Analyses of two German Landfill Sites [1].

Description	Unit	Landfill 1	Landfill2
Gases			
Methane	Vol.-%	54±1	53±1
Oxygen	Vol.-%	0.89±0.05	0.78±0.05
Carbon Dioxide	Vol.-%	35±1	24±1
Nitogen	Vol.-%	11.0±0.5	23±0.5
Hydrogen	Vol.-%	<1	<1
H_2S and Sulphur-Organic Compounds			
Hydrogen Sulphide	µg/Nm^3	230000	45000
Methanethiol	µg/Nm^3	560	88
Ethanethiol	µg/Nm^3	130	78

Dimethyl Sulphide	µg/Nm^3	4000	32
Σ Methylthiophene	µg/Nm^3	170	230
	Alkanes		
n-Butane	µg/Nm^3	11000	6300
n-Pentane	µg/Nm^3	14000	4500
2-Methylhexane	µg/Nm^3	4600	1200
n-Heptane	µg/Nm^3	9000	2600
Σ Alkane C8	µg/Nm^3	8000	5600
Σ Alkane C9	µg/Nm^3	17000	11000
Σ Alkane C10	µg/Nm^3	42000	36000
Σ Alkane C11	µg/Nm^3	16000	13000
	Alkenes		
Σ Alkane C5	µg/Nm^3	2400	2200
Σ Alkane C6	µg/Nm^3	950	950
Σ Alkane C7	µg/Nm^3	490	330
Σ Alkane C8	µg/Nm^3	580	290
	Cycloalkanes		
Σ Dimethylcyclopentane	µg/Nm^3	3000	980
Σ Dimethylcyclohexane	µg/Nm^3	5000	2000
Σ Ethymethylcyclopentane	µg/Nm^3	1600	850
Σ Trimethylcyclopentane	µg/Nm^3	490	250
Σ Trimethylcyclohexane	µg/Nm^3	6100	4300
Σ Ethylmethylcyclohexane	µg/Nm^3	5000	3500
Σ Cycloalkane C10	µg/Nm^3	11000	8200
	Alcohols		
2-Propanol	µg/Nm^3	740	67
2-Methyl-2-Propanol	µg/Nm^3	7000	3700
	Fluorochlorohydrocarbons		
1,1-difluoroethane	µg/Nm^3	130	<5
1,1,1,2-Tetrafluoroethane	µg/Nm^3	650	7
Chlorodifluoromethane	µg/Nm^3	640	550
1-Chloro-1.1-Difluoroethane	µg/Nm^3	800	47
Dichlorofluoromethane	µg/Nm^3	920	180
1,1 Dichloro-1-Fluoroethane	µg/Nm^3	920	5
	Chlorinated Componds		
Vinyl Chloride	µg/Nm^3	96	170
Cis-1,2-Dichloroethene	µg/Nm^3	210	460
1,2-Dichloroethane	µg/Nm^3	26	<5

Trichloroethene	µg/Nm^3	240	120
Tetrachloroethene	µg/Nm^3	140	82
Chlorobenzene	µg/Nm^3	220	340
1,4-Dichlorobenzene	µg/Nm^3	93	340
Ketones			
2-Propanone	µg/Nm^3	8300	<10
2-Butanone	µg/Nm^3	5100	<10
4-Methyl-2-Pentanone	µg/Nm^3	3300	<10
Aromatics			
Benzene	µg/Nm^3	3400	2500
Toluene	µg/Nm^3	21000	8800
Ethylbenzene	µg/Nm^3	22000	16000
m-/p-Xylene	µg/Nm^3	34000	26000
O-Xylene	µg/Nm^3	11000	6500
p-Isopropyltoluene	µg/Nm^3	25000	26000
Naphthalene	µg/Nm^3	80	130
Terpene			
α Pinene	µg/Nm^3	79000	65000
Limonene	µg/Nm^3	25000	21000
Ester	µg/Nm^3	<10	<10
Ethers			
Dimethyl Ether	µg/Nm^3	1800	89
Methyl-tert-Butyl-Ether	µg/Nm^3	280	57
Tetrahydrofurane	µg/Nm^3	5300	990
Silanes and Siloxanes			
Trimethylsilanol	µg/Nm^3	1200	9000
Hexamethylsiloxane	µg/Nm^3	5000	6700
Octamethyltrisiloxane	µg/Nm^3	230	200
Hexamethycyclotrisiloxane	µg/Nm^3	840	150
Octamethylcyclotetrasiloxane	µg/Nm^3	15000	3100
Decamethylcyclopentasiloxane	µg/Nm^3	3000	380
Decamethyltetrasiloxane	µg/Nm^3	<5	<5
Dodecamethylpentasiloxane	µg/Nm^3	<5	<5
Tetramethylsinane	µg/Nm^3	10	260

Table II-4. Characterisation of Sewage Gas at the Site Terni – Italy [1].

Description	Unit	08/03/07 15:30	09/03/07 9:00	12/03/07 16:30

	Alkanes/Alkenes			
Propane (*)	mg/m^3	<0.01	4.3	<0.01
2-methyl-1-propene (*)	mg/m^3	2.3	9.2	1.5
2-methyl-2-butene (*)	mg/m^3	<0.01	5.3	<0.01
Cis-1,2-dimethyl cyclopropane (*)	mg/m^3	1.5	5.8	0.7
2-methyl-1-butene (*)	mg/m^3	2.3	6.1	1.1
Hexane (**)	mg/m^3	<0.01	1.5	<0.01
Heptane (**)	mg/m^3	<0.01	0.5	<0.01
Octane(**)	mg/m^3	<0.01	1.8	<0.01
	Aromatics			
Benzene	mg/m^3	3.5	17.7	0.9
Toluene	mg/m^3	3.4	16.4	5.7
p+m-Xylene	mg/m^3	<0.01	2.6	<0.01
	Halogenated Compounds			
1,2-Dichloroethene	mg/m^3	<0.01	2.2	<0.01
Chloroform	mg/m^3	<0.01	0.8	<0.01
Tetrachloroethylene	mg/m^3	0.06	2.8	<0.01
Chlorobenzene	mg/m^3	<0.01	0.8	<0.01
	Siloxane			
Hexamethylcyclotrisiloxane	mg/m^3	<0.05	<0.05	<0.05
Octamethylcyclotetrasiloxane	mg/m^3	<0.05	<0.05	<0.05
Decamethylcyclopentasiloxane	mg/m^3	<0.05	<0.05	<0.05
	Total Amounts			
Inorganic Chlorine	mg/m^3	0.28	0.35	0.22
Organic Chlorine	mg/m^3	<0.1	<0.1	<0.1
Total Chlorine	mg/m^3	0.28	0.35	0.22
Inorganic Florine	mg/m^3	0.11	0.15	<0.1
Organic Fluorine	mg/m^3	<0.1	<0.1	<0.1
Total Fluorine	mg/m^3	0.11	0.15	<0.2
Sulphate	mg/m^3	9.6	10.1	8.4
Hydrogen Sulphide	mg/m^3	135.5	79.6	88.7
Total Halogenated-Organic Compounds	mg/m^3	0.06	4.4	<0.05
Total Aromatic Compouns	mg/m^3	13.9	73.2	9.9
Total Siloxanes	mg/m^3	<0.15	<0.15	<0.15

Table II-5. Further Gas Analyses of the Sewage Gas Site Terni - Italy [1].

Description	Unit	Terni (Italy)13/06/07	Terni (Italy)16/07/07

Methane	Vol.-%	73.9	49.1
Oxygen	Vol.-%	0.4	4.1
Carbon Dioxide	Vol.-%	25.1	29.7
Nitrogen	Vol.-%	0.6	16.9
	Minor componentes		
Hydrogen Sulphide	mg/m^3	3.300	<1
Methanethiol	mg/m^3	0.3	n.a.
Ethanethiol	mg/m^3	<0.1	n.a.
Dimethyl Sulphide	mg/m^3	<0.1	n.a.
F12	mg/m^3	<0.1	<0.1
F11	mg/m^3	<0.1	<0.1
F113	mg/m^3	<0.1	<0.1
Vinychloride (VC)	mg/m^3	<0.1	<0.1
Methylchloride	mg/m^3	<0.1	<0.1
Dichloroethane	mg/m^3	<0.1	<0.1
Dichloromethane	mg/m^3	<0.1	<0.1
Trichloromethane (Chloroform)	mg/m^3	<0.1	<0.1
Tetrachloromethane	mg/m^3	<0.1	<0.1
1,1,1-Trichloroethane	mg/m^3	<0.1	<0.1
Trichloroethene	mg/m^3	<0.1	<0.1
Tetrachloroethene	mg/m^3	<0.1	<0.1
Benzene	mg/m^3	<0.1	<0.1
Toluene	mg/m^3	0.2	2.0
Ethylbenzene	mg/m^3	<0.1	<0.1
m,p-Xylene	mg/m^3	<0.1	<0.1
o-Xylene	mg/m^3	<0.1	<0.1
Cumene (i-Propylbenzene)	mg/m^3	<0.1	<0.1
n-Propylbenzene	mg/m^3	<0.1	<0.1
Mesitylene	mg/m^3	<0.1	<0.1
Trimethylbenzene	mg/m^3	<0.1	<0.1
Ethyltoluene	mg/m^3	<0.1	<0.1
i-Propyltoluene	mg/m^3	<0.1	<0.1
Pinene	mg/m^3	<0.1	<0.1
Limonene	mg/m^3	<0.1	<0.1
Tetramethysilane (TMS)	mg/m^3	<0.1	<0.1
Trimethysilanol (MOH)	mg/m^3	<0.1	<0.1
Hexamethyldisiloxane (L2)	mg/m^3	<0.1	<0.1
Hexamethylcyclotrisiloxane (D3)	mg/m^3	<0.1	<0.1

Octamethytrisiloxane (L3)	mg/m^3	<0.1	<0.1
Octamethylcyclotetrasiloxane (D4)	mg/m^3	0.2	1.0
Decamethylterasiloxane (L4)	mg/m^3	<0.1	<0.1
Decamethylclclopentasiloxane(D5)	mg/m^3	0.4	1.8
Total org. Si-Comp.	mg/m^3	0.6	2.8
Total Si	mg/m^3	0.2	1.1

Table II-6. Initial Gas Analyses of the Landfill Site Murcia Before and After Dehumidification (10/01/07) – Spain [1].

Description	Unit	Before	After
	Gases		
Methane	Vol.-%	43.0	42.1
Oxygen	Vol.-%	5.9	5.6
Carbon Dioxide	Vol.-%	30.3	30.1
Carbon Monoxide	ppmV	65	76
Ammonia (*)	mg/m^3	4.4	17
	H_2S		
Hydrogen Sulphide (*)	mg/m^3	92	98
	Alkanes		
n-Butane	mg/m^3	9.1	8.3
n-Pentane	mg/m^3	1.8	2.0
2-Methylbutane	mg/m^3	2.9	2.9
Hexane	mg/m^3	0.9	0.9
n-Heptane	mg/m^3	1.8	1.6
Decane	mg/m^3	32.7	29.7
Undecane	mg/m^3	4.2	2.8
	Ketones		
Acetone	mg/m^3	10.9	8.1
2-Butanone	mg/m^3	15.3	9.8
	Cycloalkane		
Methylcyclohexane	mg/m^3	1.5	n.a.
	Aromatics		
Benzene	mg/m^3	1.4	1.9
Toluene	mg/m^3	63.7	62.1
Ethylbenzene	mg/m^3	19.1	18.7
m-/p-Xylene	mg/m^3	46.7	45.8
o-Xylene	mg/m^3	7.4	7.2

Propylbenzene	mg/m^3	4.0	3.5
1-Ethyl-2-methylbenzene	mg/m^3	12.5	11.8
1-Ethyl-3-methylbenzene	mg/m^3	3.6	3.4
1,2,3-Trimethylbenzene	mg/m^3	16.9	15.3
Terpenes			
α- Pinene	mg/m^3	46.5	45.7
β- Pinene	mg/m^3	24.7	23.6
Limonene	mg/m^3	106.0	91.6
p- Isopropyltoluene (cumene)	mg/m^3	331.2	317.7
Silanes and Siloxanes			
Trimethylsilanol (*)	mg/m^3	5.1	4.0
Hexamethyldisiloxane (*)	mg/m^3	0.4	0.22
Octamethylcyclotetrasiloxane (*)	mg/m^3	<0.05	<0.05
Hexamethylcyclotrisiloxane	mg/m^3	<0.05	<0.05
Octamethylcyclotetrasiloxane	mg/m^3	2.2	1.4
Decamethylcyclopentasiloxane (*)	mg/m^3	2.2	1.7
Decamethyltetrasiloxane (*)	mg/m^3	<0.05	<0.05
Dodecamethylcyclohexasiloxane (*)	mg/m^3	0.1	<0.05
Total			
Σ Hydrocarbons C5-C10	mg/m^3	64.9	45.3
Σ Hydrocarbons >C10	mg/m^3	4.2	2.8
Σ BTX	mg/m^3	138.3	135.6
Σ Other Aromatic HC	mg/m^3	36.9	33.9
Σ Terpenes	mg/m^3	508.4	478.6
Σ Inorganic Chlorine (*)	$mgCl/m^3$	<0.8	<0.8
Σ Organic Chlorine	$mgCl/m^3$	<1	<1
Σ Total Chlorine (**)	$mgCl/m^3$	<1.8	<1.8
Σ Inorganic Fluorine (*)	mgF/m^3	<0.8	<0.8
Σ Organic Fluorine	mgF/m^3	<1	<1
Σ Total Fluorine	mgF/m^3	<1.8	<1.8
Σ Total Mercaptans (*) (**)	ppmV	<1	<1
Σ Sulphate (*)	mg/m^3	<0.8	<0.8
Σ Sulphur ($S_{H2S} + S_{CH3SH} + S_{sulphate}$)	mgS/m^3	87	92
Σ Residual Oils	mg/m^3	514	308
Σ Silicon – Organic Compounds (Calculated as Siloxane) (**)	mg/m^3	10.1	7.8
Σ Silicon – Organic Compounds (Calculated as Si) (**)	$mgSi/m^3$	3.4	2.7

Σ Other families	mg/m^3	27.7	19.3

(*) It is worth mentioning that the analytical results of the measured parameters by absorption of the second impingers in all cases have been lower than the first ones. Thus, allowing the validation of the sampling of the corresponding probes.
(**) Taking as zero, the values below the quantification limit for the compounds no detected of the family

Table II-7. Further Landfill Gas Analysis of the Murcia Site (12/07/07) [1].

Description	Unit	Murcia (Spain)
Gases		
Methane	Vol.-%	44.8
Oxygen	Vol.-%	3.5
Carbon Dioxide	Vol.-%	32.1
Nitrogen	Vol.-%	19.4
H_2S		
Hydrogen Sulphide	mg/m^3	250
Halogenated Hydrocarbons		
F12	mg/m^3	3.6
F11	mg/m^3	0.4
F113	mg/m^3	<0.1
Vinylchloride (VC)	mg/m^3	0.9
Methlchloride	mg/m^3	<0.1
1,1-Dichloroethane	mg/m^3	<0.1
1,2-Dichloroethane	mg/m^3	<0.1
1,1-Dichloroethane	mg/m^3	<0.1
Cis-1,2- Dichloroethane	mg/m^3	1.0
Trans-1,2- Dichloroethane	mg/m^3	<0.1
Dichloromethane	mg/m^3	<0.1
Trichloromethane (Chloroform)	mg/m^3	0.1
Tetrachloroethane	mg/m^3	<0.1
1,1,1-Trichloroethane	mg/m^3	3.1
Trichloroethane	mg/m^3	6.2
Total Chlorine	mg/m^3	11.7
Total Fluorine	mg/m^3	1.2
Aromatics, BTX		
Benzene	mg/m^3	2.6
Toluene	mg/m^3	58.5
Ethylbenzene	mg/m^3	16.7
m,p-Xylene	mg/m^3	31.8

o-Xylene	mg/m^3	6.0
Cumene (i-Propylbenzene)	mg/m^3	0.3
n-Propylbenzene	mg/m^3	0.5
Mesitylene	mg/m^3	2.1
1,2,4 – Trimethylbenzene	mg/m^3	2.5
1,2,3 – Trimethylbenzene	mg/m^3	2.0
3,4-Ethyltoluene	mg/m^3	1.9
2-Ethyltoluene	mg/m^3	0.9
i-Propyltoluene	mg/m^3	129.4
Pinene	mg/m^3	38.2
Limonene	mg/m^3	45.0
Silanes and Siloxanes		
Tetramethylsilane (TMS)	mg/m^3	<0.1
Trimethylsilanol (MOH)	mg/m^3	5.8
Hexamethyldisiloxane (L2)	mg/m^3	0.5
Hexamethylcyclotrisiloxane (D3)	mg/m^3	0.1
Octamethyltrisiloxane (L3)	mg/m^3	<0.1
Octamethylcyclotetrasiloxane (D4)	mg/m^3	2.3
Decamethyltetrasiloxane (L4)	mg/m^3	<0.1
Decamethylcyclopentasiloxane (D5)	mg/m^3	1.8
Total org. SI-Comp	mg/m^3	10.5
Total Si	mg/m^3	3.6

Table II-8. Analysis of the concentration of the minor components at Landfill site 1 before and after purification – Germany.

Minor Compound / Class	Raw Gas [mg/m3]
H_2S	53
Halogenated Hydrocarbons	
F12	2.1
F113	<0.1
Vinylchloride (VC)	0.9
Methlchloride	<0.1
1,1-Dichloroethane	<0.1
1,1-Dichloroethane	<0.1
Cis-1,2- Dichloroethane	0.8
Trans-1,2- Dichloroethane	<0.1
Dichloromethane	0.1

Trichloromethane (Chloroform)	<0.1
Tetrachloroethane	<0.1
1,1,1-Trichloroethane	<0.1
Trichloroethane	0.2
Tetrachloroethene	0.1
Aromatics, BTX	
Benzene	3.1
Toluene	10.0
Ethylbenzene	12.9
m,p-Xylene	19.2
o-Xylene	5.1
Cumene (i-Propylbenzene)	3.6
n-Propylbenzene	1.7
Mesitylene	2.6
1,2,4 – Trimethylbenzene	5.2
1,2,3 – Trimethylbenzene	2.1
3,4-Ethyltoluene	4.7
2-Ethyltoluene	2.5
i-Propyltoluene	17.4
Pinene	36.9
Limonene	17.0
Silicon Compounds	
Tetramethylsilane (TMS)	3.8
Trimethylsilanol (MOH)	8.2
Hexamethyldisiloxane (L2)	8.3
Hexamethylcyclotrisiloxane (D3)	0.4
Octamethyltrisiloxane (L3)	0.3
Octamethylcyclotetrasiloxane (D4)	3.7
Decamethyltetrasiloxane (L4)	<0.1
Decamethylcyclopentasiloxane (D5)	1.9

Table II-9. Measured masses with CI-MS and concentrations of the most relevant minor components present in LFG (landfill gas) – Germany [1].

Compound Group	Compound	Mass	Conc. [µg/m3]	Conc. [ppmv]
Sulphur	H_2S	34	230000	161.97
	Methanthiol	48	560	0.28

	Ethanthiol	62	4000	1.54
Alkane	n-butane	58	11000	4.54
Cyclic Alkane	Cyclohexane	84	8200	2.34
Alcohol	Tert-Butyl-Alcohol	59	7000	2.27
Ketone	Acetone	58	8300	3.43
	Butanone	72	5100	1.70
BTEX	Benzene	78	3400	1.04
	Toluen	92	21000	5.47
	m+p Xylene	106	34000	7.69
	Trimethylbenzene	120	3800	0.76
	Isopropylbenzene (Cumen)	119	5600	
Terpene	Limonene	68	25000	4.40
	Beta-Pinene	93	4700	0.83
	Alpha-Pinene	93	79000	13.92
Chlorinated Compounds	Trichloroethene	130	240	0.04
	Tetrachloroethene	164	140	0.02
	Chlorobenzene	112	220	0.05
Silicon-organic Compounds	Trimethysilanol	90	12000	3.19
	Hexamethyldisiloxane (L2)	162	5000	0.74
	Decamethyltetrasiloxane (L4)	296		
	Hexamethylcyclotrisiloxane (D3)	208	840	
	Octamethylcyclotetrasiloxane (D4)	282	15000	1.21
	Decamethylcyclopentasiloxane (D5)	354	3000	0.19

Table II-10. Site 1. Landfill Gas Matrix, average results of two campaigns – Finland [2].

		From landfill	After drying
CH_4	vol-%	52	50
CO_2	vol-%	41	41
H_2O	vol-%	3.3	0.9
NH_4	ppm	3.5	<1
		Organic silicon, mg/m^3:	
L2*		-	-
L3		0.3	0.3
L4		2.6	2.3
D3		2.1	1.7
D4		2.6	3.0
D5		1.8	1.8

TMS**	1.8	1
	Sulphur compounds mg/m^3:	
H2S	820	710
DMS	2.8	2.8
butanethiol	1.5	1.5
ethylthiol	2.8	2.8
thiourea	0.3	0.3
	VOC (main components), mg/m^3:	
Ethylbenzene	21	19
Nonane	14	13
α-pinene	50.5	13
Σ – xylenes	11	18
limonene	126	119
etanol	31	28
toluene	19	18
octane	0.1	0.1
Σ halogens **, mg/m^3	2-7	2-7
main: trichlorofluoromethane		
1,2 - dichloroethene		

* quantification inscure due to high hydrogen sulphide content
** quantified as toluene eqv.

Table II-11. Site 1. Site 2. Landfill Gas Matrix – Finland [2].

	From landfill	To microturbine, actived carbon filtrated, 17 weeks in use	To microturbine, active carbon filtrated, new filter media
CH_4 vol-%	36.5	36.2	37
CO_2 vol-%	32.7	32.4	
H_2O vol-%	0.51	0.47	0.06
O_2 vol-%	1	1	1
		Organic silicon, mg/m^3:	
L2	0.2	0.2	0.01
L3	0.05	0.08	<0.01
L4	1.3	2.1	<0.01
D3	2.3	0.9	<0.01
D4	0.9	1	<0.01
D5	1.3	1.4	<0.01
TMS**	0.7	0.6	n.d

	Sulphur compounds mg/m^3:		
H_2S	67	21	<5
DMS	0.8	0.8	<0.01
ethylthiol	4.1	3.9	<0.01
	VOC (main components), mg/m^3:		
Ethylbenzene	25	28	<0.01
Nonane	9.4	9.9	<0.01
α-pinene	6.2	14	<0.01
Σ – xylenes	33	40	<0.01
limonene	2.4	3.4	<0.01
toluene	4.9	7.2	<0.01
Σ halogens **, mg/m^3 main: trichlorofluoromethane tetrachloroethene	0.7	0.25	n.d.

* quantified as toluene eqv.

Table II-12. Site 3. Landfill Gas Matrix – Finland [2].

	From landfill	To microturbine, actived carbon filtrated, 17 weeks in use	To microturbine, actived carbon filtrated, new filter media	To fuel cell Purafil ® new
CH_4 vol-%	44.6	44.2	43.8	44.0
CO_2 vol-%	30	30	30	30
H_2O vol-%	0.12	0.09	0.06	0.27
	Organic silicon, mg/m^3:			
L2	0.2	<0.02	<0.02	<0.02
L3	<0.1	<0.05	<0.02	<0.02
L4	<0.1	<0.05	<0.05	<0.05
D3	0.9	<0.02	<0.02	<0.02
D4	0.2	<0.02	<0.02	<0.02
D5	0.1	<0.02	<0.02	<0.02
	Sulphur compounds mg/m^3:			
H_2S	25.2	<5	<5	<5
DMS	0.4	nd	nd	nd

Ethylthiol	3.6	-	-	-
		VOC (main components), mg/m^3:		
Ethylbenzene	4.4	0.04		
Nonane	8.7			
α-pinene	3.1			
Σ – xylenes	6.1	0.132		
Limonene	0.6			
Σ halogens*, mg/m^3	0.52	0.25	0.1	0.1
main: chloroethane				

* quantified as toluene eqv.

Table II-13. Site 4. WWTP Biogas Matrix, average of two compaigns – Finland [2].

CH_4	vol-%	65
CO_2	vol-%	33.5
H_2O	vol-%	2
O_2	vol-%	-
	Organic silicon, mg/m^3:	
L2		0.03
L3		0.03
L4		0.12
D3		0.15
D4		1.6
D5		27
TMS		0.03
	Sulfur compounds mg/m^3:	
H_2S		<14
DMS		0.1
Dipentyl disulphide *		0.1
	VOC (main components), mg/m^3:	
Ethylbenzene		28
Nonane		3.1
α-pinene		14
Σ – xylenes		1.3
Limonene		5.23
Toluene		4.6
Σ halogens *, mg/m^3		0.09
main: chloroethane		

* quantified as toluene eqv.

Table II-14. Site 4. WWTP Biogas Matrix, average of one week monitoring – Finland [2].

CH_4	vol-%	65
CO_2	vol-%	29
H_2O	vol-%	0.5
O_2	vol-%	-
	Organic silicon, mg/m^3:	
L2		0.04
L3		<0.01
L4		1.29
D3		0.03
D4		0.1
D5		0.9
TMS*		0.6
	Sulphur compounds mg/m^3:	
H_2S		30
DMS		0.1
Dipentyl disulphide *		0.3
	VOC (main components), mg/m^3:	
Ethylbenzene		1.7
Nonane		1.1
α-pinene		1.3
Σ – xylenes		1.4
Limonene		62
Toluene		8
Σ halogens *, mg/m^3		0.7
main: tetrachloroethene, dichloromethane		

* quantified as toluene eqv.

References

[1] Urban, W.; Lohmann, H.; Gómez Salazar, J.I., Collection of biogas data – Biogas Integrated Concept – a European Program for Sustainability, Fraunhofer Institut UMSICHT, 2008.

[2] Decamethylcyclopentasiloxane, MSDS – Material safety data sheet - http://www.clearcoproducts.com/pdf/msds/cosmetic/MSDS-Cyclo-2245.pdf - Clearco Products Inc.

Appendix III: Identification of trace species that can potentially act as poison for CPOx catalysts

Biogas/landfill gas is a mixture composed principally from methane (40– 70%) and carbon dioxide, along with other contaminants (see also Appendix II): hydrogen sulfide (H_2S), carbonil sulfide (COS), carbon disulfide (CS_2), hydrochloric acid (HCl), hydrofluoric acid (HF), ammonia (NH_3), water (H_2O), nitrogen (N_2), oxygen (O_2), hydrogen (H_2), carbon monoxide (CO), hydrocarbons (C_nH_{2n+2}), halogenated hydrocarbons ($C_nH_{2n+1}X$), siloxanes (hexamethylcyclotrisiloxane (D3), decamethyl-cyclopentasiloxane (D5), octamethylcyclotetrasiloxane (D4), hexamethyldisiloxane (L2), octamethyltrisiloxane (L3)), tars, heavy metals: arsenic (As), lead (Pb), zinc (Zn), cadmium (Cd), mercury (Hg), particulates, etc.

As a result of effects on reforming catalyst(s) and anodic materials of the SOFC, the contaminants can be classified into three classes (as shown in Table III-1):

- C1 – compounds directly demaging;
- C2 – compounds not directly demaging (activated by temperature, surface of catalyst);
- C3 – compounds not directly demaging (inertization, passivation)

Table III-1. Contaminants for reforming catalyst(s) and anodic materials of the SOFC [1].

Name	Formula	Phys. state	Contamin at class
Hydrogen sulfide	H_2S	G	C1
Carbonil sulfide	COS	G	C1
Carbon disulfide	CS_2	L	C1
Hydrogen chloride	HCl	G	C1
Hydrogen fluoride	HF	G	C1
Ammonia	NH_3	G	C1, C2
Hydrogen phosphide	PH_3	G	C1, C2
Metals (Hg, Pb, Se, As, Cd, Sb)	-	L, S	C3
Decamethylcyclopentasiloxane – D5	$C_{10}H_{30}O_5Si$	L	C3
Hexamethyldisiloxane – L2	$C_6H_{18}OSi_2$	L	C3
Octamethylcyclotetrasiloxane – D4	$C_8H_{24}O_4Si_4$	L	C3
Nitrous oxide	N_2O	G	C3
Nitric oxide	NO	G	C3
Dinitrogen trioxide	N_2O_3	L	C3
Dinitrogen tetroxide	N_2O_4	G	C3
Dinitrogen pentoxide	N_2O_5	S	C3
Sulfur dioxide	SO_2	G	C2
Sulfur trioxide	SO_3	G	C2
Chlorodifluoromethane	CH_2Cl_2	G	C2
Chloroform	$CHCl_3$	L	C2

Dichlorofluoromethane	$CHCl_2F$	G	C2
Chlorofluoromethane	CH_2ClF	G	C2
Dichloromethane	CH_2Cl_2	L	C2
Chlorotrifluoromethane	$CClF_3$	G	C2
Carbon tetrachloride	CCl_4	L	C2
Trichlorofluoromethane	CCl_3F	G	C2
Dichlorodifluoromethane	CCl_2F_2	G	C2
1,2-Dichlorotetrafluoroethane	$C_2Cl_2F_4$	G	C2
1,1,1-Trichloroethane	$C_2H_3Cl_3$	L	C2
1,2-Dichloroethene	$C_2H_2Cl_2$	L	C2
1,2-Dichloroethane	$C_2H_4Cl_2$	L	C2
1,1-Dichloroethane	$C_2H_4Cl_2$	L	C2
1,1,2-Trichloroethane	$C_2H_3Cl_3$	L	C2
1,1,1,2-Tetrachloroethane	$C_2H_2Cl_4$	L	C2
1,1,2-Trichloro-1,2,2-Trifluoroethane	$C_2Cl_3F_3$	L	C2
Trichlorethene	C_2HCl_3	L	C2
Tetrachlorethene	C_2Cl_4	L	C2
Vinyl chloride	C_2H_3Cl	L	C2
2,2-Dichloropropane	$C_3H_6Cl_2$	L	C2
1,3-Dichloropropane	$C_3H_6Cl_2$	L	C2
Chlorobenzene	C_6H_5Cl	L	C2
1,2-Dichlorobenzene	$C_6H_4Cl_2$	L	C2
1,4-Dichlorobenzene	$C_6H_4Cl_2$	L	C2
Benzene	C_6H_6	L	C1, C3
Toluene	$C_6H_5(CH_3)$	L	C1, C3
ethyl Benzene	$C_6H_4(C_2H_5)$	L	C1, C3
o,m,p - Xylene	$C_6H_4(CH_3)_2$	L	C1, C3
iso-propyl Benzene	$C_6H_5(i\text{-}C_3H_7)$	L	C1, C3
1,3,5 trimethyl Benzene	$C_6H_3(CH_3)_3$	L	C1, C3
p-methyl iso-propyl Benzene	$C_6H_4(i\text{-}C_3H_7)(CH_3)$	L	C1, C3
1,2,4,5 tetramethyl Benzene	$C_6H_2(CH_3)_4$	L	C1, C3

LEGENDA: G – gas, L – liquid, S – solid, C1, C2, C3 – contaminant class

References

[1] Chisega-Negrilă, C-G., Contaminant detection and gas analysis: Definition of measurement and sampling conditions and selected methodologies, MCFC CONTEX, Bucharest, 2010.

Appendix IV: Standards that can be used for sampling and measurement of biogas contaminants

Here are listed some standards that can be used for the sampling and measurement of sulfur compounds, ammonia, carbon monoxide, carbon dioxide, oxygen, hydrogen fluoride (HF), hydrogen chloride (HCl), water, heavy metals, hydrocarbons, halogenated hydrocarbons, volatile organic compounds (VOC's) and particulates. At ISO (International Standardization Organization) there are not specific standards for sampling and analysis of biogas contaminants.

1. Generalities

- SR ISO 4226:2008 – Air quality – General aspects – Units of measurement;
- ISO 4225:1994 - Air quality -- General aspects – Vocabulary;
- SR ISO 7504:2004 – Gas analysis. Vocabulary;
- ISO 19702:2006 - Toxicity testing of fire effluents -- Guidance for analysis of gases and vapours in fire effluents using FTIR gas analysis;
- ISO 8573-6:2003 - Compressed air -- Part 6: Test methods for gaseous contaminant content.

2. Sulfur compounds

- ISO 4219:1979 - Air quality -- Determination of gaseous sulfur compounds in ambient air -- Sampling equipment;
- STAS 10814-76 – Air purity. Determination of hydrogen sulfide;
- ISO 6326-1:2007 - Natural gas -- Determination of sulfur compounds -- Part 1: General introduction;
- ISO 6975:1997 - Natural gas -- Extended analysis -- Gas-chromatographic method.

3. Ammonia

- STAS 10812-76 – Air purity. Determination of ammonia.

4. CO, CO_2, O_2

- ISO 12039:2001 - Stationary source emissions -- Determination of carbon monoxide, carbon dioxide and oxygen -- Performance characteristics and calibration of automated measuring systems;
- SR ISO 10396:2008 - Stationary source emissions – Sampling for the automated determination of gas emission concentrations for permanently – installed monitoring systems;
- ISO 6974-6:2002 - Natural gas -- Determination of composition with defined uncertainty by gas chromatography -- Part 6: Determination of hydrogen, helium, oxygen, nitrogen, carbon dioxide and C1 to C8 hydrocarbons using three capillary columns.

5. HF

- ISO 15713:2006 - Stationary source emissions -- Sampling and determination of gaseous fluoride content.

6. HCl

- SR EN 1911-1:2002 – Stationary source emissions – Manual method of determination of hydrogen chloride – Part 1: Sampling of gases;
- SR EN 1911-2:2002 – Stationary source emissions – Manual method of determination of hydrogen chloride – Part 2: Gaseous compounds absorption;
- SR EN 1911-3:2002 – Stationary source emissions – Manual method of determination of hydrogen chloride – Part 3: Absorption solutions analysis and calculation;
- ISO 21438-2:2009 - Workplace atmospheres -- Determination of inorganic acids by ion chromatography -- Part 2: Volatile acids, except hydrofluoric acid (hydrochloric acid, hydrobromic acid and nitric acid).

7. Water

- ISO 6327:1981 - Gas analysis -- Determination of the water dew point of natural gas -- Cooled surface condensation hygrometers;
- ISO 8573-9:2004 - Compressed air -- Part 9: Test methods for liquid water content.

8. Hydrocarbons

- ISO 6974-6:2002 - Natural gas -- Determination of composition with defined uncertainty by gas chromatography -- Part 6: Determination of hydrogen, helium, oxygen, nitrogen, carbon dioxide and C1 to C8 hydrocarbons using three capillary columns;
- ISO 6974-1:2000 - Natural gas -- Determination of composition with defined uncertainty by gas chromatography -- Part 1: Guidelines for tailored analysis;
- ISO/TS 14167:2003 - Gas analysis -- General quality assurance aspects in the use of calibration gas mixtures – Guidelines;
- ISO/TR 24094:2006 - Analysis of natural gas -- Validation methods for gaseous reference materials;
- ISO 6975:1997 - Natural gas -- Extended analysis -- Gas-chromatographic method;
- ISO 23874:2006 - Natural gas -- Gas chromatographic requirements for hydrocarbon dewpoint calculation;
- ISO 1995:1981 - Aromatic hydrocarbons – Sampling;
- ISO 2209:1973 - Liquid halogenated hydrocarbons for industrial use – Sampling;
- ISO 11338-1:2003 - Stationary source emissions -- Determination of gas and particle-phase polycyclic aromatic hydrocarbons -- Part 1: Sampling;
- ISO 11338-2:2003 - Stationary source emissions -- Determination of gas and particle-phase polycyclic aromatic hydrocarbons -- Part 2: Sample preparation, clean-up and determination;
- SR EN 13649:2002 - Stationary source emissions – Determination of the mass concentration of individual gaseous organic compounds – Activated carbon and solvent desorption method;

- ISO 14965:2000 - Air quality -- Determination of total non-methane organic compounds -- Cryogenic preconcentration and direct flame ionization detection method.
- ISO 10301:1997 - Water quality - Determination of highly volatile halogenated hydrocarbons -- Gas-chromatographic methods

- ISO 15009:2002 - Soil quality - Gas chromatographic determination of the content of volatile aromatic hydrocarbons, naphthalene and volatile halogenated hydrocarbons -- Purge-and-trap method with thermal desorption

- ISO 22155:2005 - Soil quality - Gas chromatographic quantitative determination of volatile aromatic and halogenated hydrocarbons and selected ethers -- Static headspace method

- ISO 16017-2:2003 - Indoor, ambient and workplace air -- Sampling and analysis of volatile organic compounds by sorbent tube/thermal desorption/capillary gas chromatography -- Part 2: Diffusive sampling

9. VOC's

- ISO 16017-1:2000 - Indoor, ambient and workplace air -- Sampling and analysis of volatile organic compounds by sorbent tube/thermal desorption/capillary gas chromatography -- Part 1: Pumped sampling;
- ISO 16017-2:2003 - Indoor, ambient and workplace air -- Sampling and analysis of volatile organic compounds by sorbent tube/thermal desorption/capillary gas chromatography -- Part 2: Diffusive sampling;
- ISO 16000-6:2004 - Indoor air -- Part 6: Determination of volatile organic compounds in indoor and test chamber air by active sampling on Tenax TA sorbent, thermal desorption and gas chromatography using MS/FID;
- ISO 16200-1:2001 - Workplace air quality -- Sampling and analysis of volatile organic compounds by solvent desorption/gas chromatography -- Part 1: Pumped sampling method;
- ISO 16200-2:2000 - Workplace air quality -- Sampling and analysis of volatile organic compounds by solvent desorption/gas chromatography -- Part 2: Diffusive sampling method.

10. Siloxane sampling and measurement

According to [1,3-9] there are no standard methods for analyzing siloxanes in gas matrix, but based on the literature search, several methods are available. Collection of siloxane samples is not yet standardized. In some works [1,3,10] there are described a sum of sampling methods, but none of them are generally accepted. Samples can be collected in steel canisters, glass collection containers, Tedlar bags, or concentrated in a liquid or solid absorbent. In the following Table IV-1 is provided a summary of the compatibility of different sampling techniques.

Table IV-1. Sampling techniques of gaseous siloxane [1,2,10].

Method	Advantages	Disadvantages	Material	Recovery	Compatibility with other impurities in the gas	Obs.
Can absorb Gas sample taken into canister or gas bag	Simple, fast	Poor representation if the consistency of the gas varies. Less suitable for heavy siloxanes	Metal canister	Quite good	Compatible	6 liter metal Summa canister analyzed by GC/MS after being pressurized for 24 h [4] Heaviest molecules (D5, D6) can absorb onto the walls of the canister [1].
			Tedlar bag	Good		Most common used accros Europe. Heaviest molecules (D5, D6) can absorb onto the walls of the bag [1].
			Aluminium coated bag	Adsorption effect		Less suitable for sampling than Tedlar bags [1]
Collection onto adsorbent	Relative simple sample Possibility of longer sampling time, in which case a more representative sample is obtained	Poor representation if the consistency of the gas varies	XAD-2, XAD-4, polyurethane foam	Imperfect adsorption	Varies	Desorbtion using carbon disulfide, methylene chloride, methylisobutylcetone (MIBK) [2]
			Activated charcoal	Depends on the quality of activated carbon		
			Tenax	Good	Varies	
Impinger	Longer sampling time is suitable for varying gas concentration	Requires an ice bath in the field. More demanding sample train	Methanol, acetone, n-hexane, dodecane, etc.	Usually good, D3 more difficult	Limited suitability (depends on the compound)	Midget impingers – 6 ml methanol in each – flowrate 112 ml/min, 3 h – identification by GC/MS - determines L2, L3, D4, D5 and D6 - Air Toxics (Folsom, California) [10] Impingers – 20 ml methanol – flowrate 1 l/min, 20 min – identification by GC/MS – ESS Laboratories (Cranston, Rhode Island) [10]

Siloxane samples are generally analyzed using: GC/FID (FID – flame ionization detector), GC/MS (MS – mass spectroscopy), GC/AED (AED – atomic emission spectroscopy) and the quantification of siloxane (mg/m^3) is done as toluene equivalents (because siloxane reference certified materials are not readily available), which often underestimates the true concentration.

References

[1] Arnold, M., Reduction and monitoring of biogas trace compounds. Espoo 2009. VTT Tiedotteita - RESEARCH NOTES 2496, ISBN 978-951-38-7314-1, ISSN 1455-0865.

[2] MICROPHILOX Project Web site - http://www.microphilox.com/reference_02b.htm.

[3] Grümping, R., Mikolajczak, D. & Hirner, A., 1998, Determination of trimethylsilanol in the environment by LT-GC/ICP-OES and GC-MS. Fresenius' journal of analytical chemistry., Vol. 361. pp.133–139.

[4] Huppmann, R., Lohoff, H., Schröder, H., 1996, Cyclic siloxanes in the biological waste water treatment process—determination, quantification and possibilities of elimination, Fr. J. Anal.Chem., Vol. 354, pp. 66–71.

[5] Tuazon, E., Aschmann, S., Atkinson, R., 2000, Atmospheric degradation of volatile methyl-silicon compounds. Environmental Science & Technology, Vol. 34, pp. 1970–1976.

[6] Schweigkofler, M. & Niessner, R., 1999, Determination of Siloxanes and VOC in Landfill Gas and Sewage Gas by Canister Sampling and GC-MS/AES Analysis. Env. Sci. Technol., Vol. 33, pp. 3680–3685.

[7] Stoddart, J., Zhu, M., Staines, J., Rothery, E., Lewicki, R., 1999, Experience with halogenated hydrocarbons removal from landfill gas. In: Proceedings Sardinia 1999 7th International Waste Management and Landfill Symposium, Vol. II. pp. 489–498.

[8] Varaprath, S., Stutts, D., Kozerski, G. 2006, A Primer on the Analytical Aspects of Silicones at Trace Levels-Challenges and Artifacts – A Review. Silicon Chemistry, Vol. 3, Nr.1–2 / September 2006.

[9] Hagmann, M., Heimbrand, E., Hentschel, P., 1999, Determination of siloxanes in biogas from landfills and sewage treatment plants In: Proceedings Sardinia 99, 7th Int. Waste Management and Landfill Symposium, Cagliari, Italy, 4–8 October 1999.

[10] Wheless, E., Pierce, J., 2004, Siloxanes in Landfill and Digester Gas Update. Presentation at SWANA's 27th Annual Landfill Gas Symposium, March 2004, San Antonio, Texas.

Appendix V: Biogas/landfill gas clean-up for use in solid oxide fuel cells

1. Biogas produced in landfills (landfill gas)

To make the landfill gas (dirtiest quality biogas) usable by SOFC, OVM-ICCPET proposed the following flux [1]:

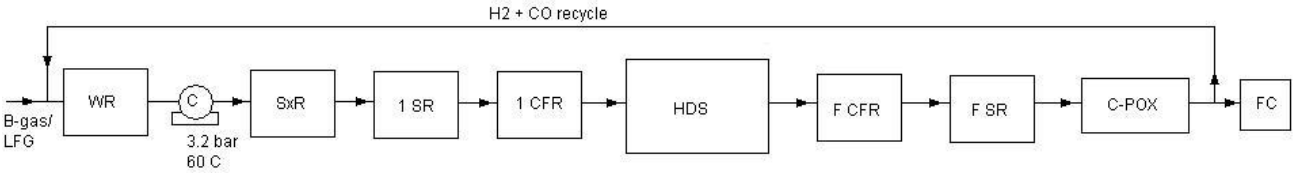

Legenda:

B-gas – biogas; LFG – landfill gas; WR – water removal unit; C – compressor; SxR – siloxanes removal unit; 1 SR – first stage bulk hydrogen sulphide removal unit; 1 CFR – first stage bulk chlorinated and fluorinaded compounds removal unit; HDS – hydrodesulphurisation unit; F CFR – fine chlorinated and fluorinaded compounds removal unit; F SR – fine hydrogen sulphide removal unit; C-POX – catalitic partial oxidation reformer unit; FC – fuel cell (SOFC)

Figure V-1. Proposed flux for biogas/landfill gas clean-up.

Description of the proposed flux:

Biogas/Landfill gas (LFG) enters the system at near atmospheric pressure from the digester/landfill and is mixed with a hydrogen-rich recycle stream. The biogas/LFG is then compressed to 3.2 bar and cooled to 60 °C. The cooled stream flows to the bulk sulfur removal where the hydrogen sulfide concentration is lowered to an acceptable level. The gas leaving the bulk sulfur removal stage can be indirectly heated by burning a small amount of the gas leaving the bulk sulfur removal unit in a fired heater. After that the gas enters to bulk halogenated compounds unit. The gas then flows to the hydrogenation unit. In the hydrogenation unit, trace organic sulfur compounds are converted to H_2S and halogenated hydrocarbons are converted to the corresponding halogenated acids (HCl, HF, etc.). Oxygen is also consumed in this unit by combustion with hydrogen. The hydrotreated stream then flows through the halides and trace sulfur removal solids.

As previously mentioned, the clean fuel flows to CPOx reformer where the fuel is converted to hydrogen and CO and a part of this stream is recycled. Heat for the partial oxidation reaction is provided by burning a small amount of the gas leaving the bulk sulfur removal unit. The recycle stream leaving the reformer is then cooled and mixed with the raw biogas/landfill gas at the inlet of the compressor to provide hydrogen needed for the hydrogenation reactions.

Bulk Sulfur Removal - The sulphur removal material that can be used in this stage is supported iron oxide (SulfaTreat - a mixture of ferric oxide and tri-ferric oxide supported on an inert inorganic substrate). The advantages of SulfaTreat are its low cost, its low operating temperature 60 °C, and its ability to reduce the hydrogen sulfide level to an acceptable level. In addition, it is non-hazardous and can be used on site as fill material, road base, or as a soil amendment, eliminating disposal costs. Two beds can be used in a lead/lag configuration. When the second bed breaks through at 5,000 ppbv H_2S, it is placed as a leading bed, while a fresh bed is placed in the lagging

position. Switching can be done by appropriate use of valves. A saturated sulfur loading of 10.5% can be used.

Trace Sulfur Removal - The bulk sulfur removal stage is followed by a trace sulfur removal stage. This consists of a hydrogenation unit which hydrogenates the organic sulfur compounds to form H_2S by reaction with hydrogen. The hydrogen required is provided by a recycle stream (clean biogas/landfill gas). The H_2S produced is removed by a zinc oxide sorbent which removes the H_2S according to the following reaction:

$$ZnO + H_2S \rightarrow ZnS + H2O \qquad (V\text{-}1)$$

This reaction can lower the concentration of H_2S to below 50 ppb. Low H_2S concentration is favored by low water content and by lower temperatures.

The zinc oxide is located in the lower portion of a cylindrical reaction vessel which is shared with the chloride guard (Figure V-2).

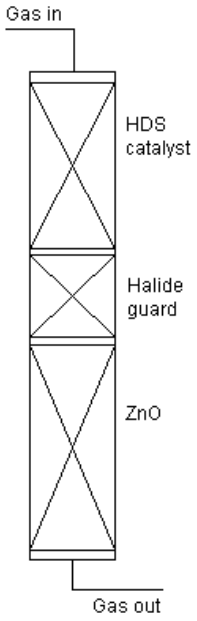

Figure V-2. The compact trace biogas/LFG clean-up column.

Halogenated Hydrocarbon Removal - In the first stage two adsorbtion vessels filled with activated carbon can be used in a lead/lag configuration. Halides are removed by first converting to corresponding halogenated acids (HCl, HF, etc.) at high temperature and then removing the halogenated acids by reaction with potassium carbonate or calcium oxide promoted activated alumina at high temperature.

$$2HX + K_2CO_3 \leftrightarrow 2\,KX + CO_2 + H_2O \qquad (V\text{-}2)$$

In addition to reaction with potassium carbonate, HX can be also removed by chemisorption on the alumina support used for the halide guard. Other materials are also available such as calcium promoted halide guards.

After this treatment the cleaned-up biogas/LFG consists principally in a mixture of methane and carbon dioxide, which for CPOx reforming purposes can be assimilated as methane.

2. Biogas generated from anaerobic digesters

Figure V-3 shows the clean-up flux proposed for biogas (produced in anaerobic digesters) usage in SOFC systems. The biogas gererated from anaerobic digesters is less treatment demanding comparing to the biogas formed in landfills (landfill gas) and then the clean-up flux is simplier.

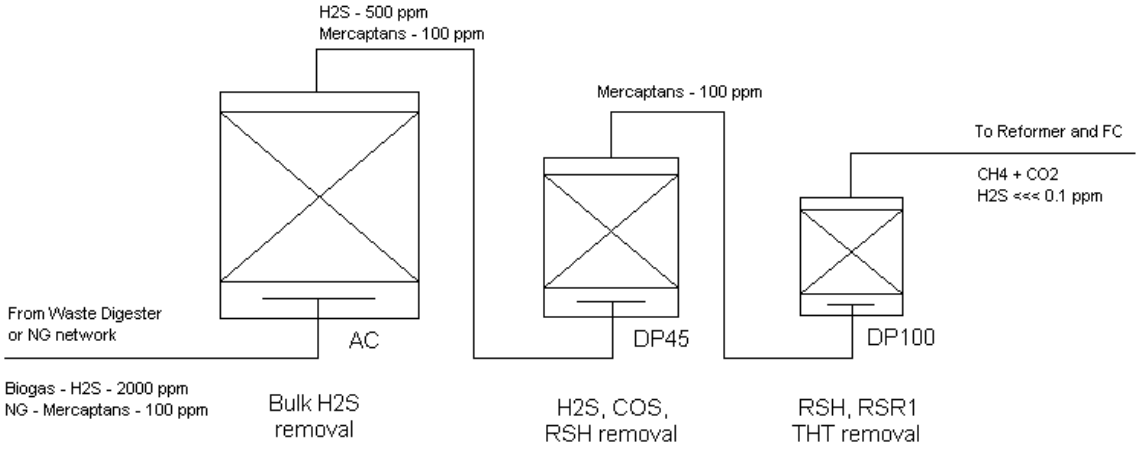

Figure V-3. Proposed flux for clean-up of biogas produced in anaerobic digesters.

References

[1] Steinfeld, G., Sanderson, R. – Landfill gas clean-up for carbonate fuel cell power generation – final report – Energy Research Corporation, 1998, NREL/SR-570-26037